2018

Study of the energy gap structure in iron-based superconductors using London penetration depth and controlled artificial disorder

Serafim Teknowijoyo
Iowa State University

Study of the energy gap structure in iron-based superconductors using London penetration depth and controlled artificial disorder

by

Serafim Teknowijoyo

A dissertation submitted to the graduate faculty

in partial fulfillment of the requirements for the degree of

DOCTOR OF PHILOSOPHY

Major: Condensed Matter Physics

Program of Study Committee:
Ruslan Prozorov, Major Professor
Makariy A. Tanatar
Peter P. Orth
James Cochran
Aaron J. Rossini

The student author, whose presentation of the scholarship herein was approved by the program of study committee, is solely responsible for the content of this dissertation. The Graduate College will ensure this dissertation is globally accessible and will not permit alterations after a degree is conferred.

Iowa State University

Ames, Iowa

2018

TABLE OF CONTENTS

Page

LIST OF TABLES

LIST OF FIGURES

ACKNOWLEDGEMENTS

Since I did not get to this point solely on my own ability, I would like to acknowledge and give the credits due to the people that have pushed and helped me forward and also first and foremost, to God. Pursuing the degree was mentally easier due to the peace coming from my belief that the salvation I received from Christ is much more significant than any degree that I could ever get. I understand that people might wonder why I have such belief. However, in a sense I think it is quite a rational choice given my incomplete comprehension of truth about life and more specifically, the afterlife (Pascal's wager).

I would also like to thank Dr. Ruslan Prozorov for giving me the opportunity to pursue my research career in the Supermaglab group. The group members have been great, especially for Dr. Makariy A. Tanatar and Dr. Kyuil Cho for their help and advices. I also thank Dr. Peter P. Orth, Dr. James Cochran and Dr. Aaron J. Rossini for being members in my committee and challenging my physics understanding with their questions.

I would take the opportunity to thank and appreciate my family members. My Dad, although he passed away 14 years ago, has fostered in me the mindset of curiosity and pursuing the answers. My Mom, who loves me more than her desire to keep me close and supports me even when I am far away from home. My brothers and sisters-in-law, who have supported me in various ways along the process.

Then I would like to thank George and Dorothy Hatfield, Tony and Valentina Loe, Mallory and Judy Parmerlee, John and Marissa Sharbaugh for their mentorship, godly examples and for always being available in times of need during my stay in Ames.

I thank all my friends and other people that have supported me and made the time I've spent in Ames more fun and enjoyable. Special thanks to Octavyan Revyn Pratama, for being a faithful friend and keeping in touch even after all these years I have been away from home in Solo, Indonesia.

Finally, I thank and appreciate Iowa State University Physics and Astronomy Department and Ames Laboratory for the wonderful staffs and the financial support during my Ph.D. program. This work was supported by the U.S. Department of Energy (DOE), Basic Energy Sciences at the Ames Laboratory under contract number DE-AC02-07CH11358. Ames Laboratory is operated for the DOE by Iowa State University. The document number assigned to this dissertation is IS-T 3255.

ABSTRACT

A combination of London penetration depth and artificial disorder was used to probe the energy gap structure and symmetry of a few members of the iron-based superconductor systems. Information regarding the gap structure and symmetry is an important clue which helps uncover the mechanism behind the unconventional, non-BCS-type superconductors. We used the tunnel-diode resonator method to do London penetration depth measurements with high precision down to 50 mK base temperature. The disorder is introduced by electron irradiation, which was performed at the SIRIUS facility in Ecole Polytechnique (Palaiseau France) to produce point-like disorder in the materials of study. Non-magnetic defects induced by the irradiation influence each material differently depending on its underlying susceptibility to impurity scattering. The response to irradiation provides another key clue about the gap structure and symmetry of iron-based superconductors. This dissertation describes the details of the experimental work on 16 samples from the $Ba_{1-x}K_xFe_2As_2$ system across the superconducting dome, with the results can be explained coherently with $s_{\pm}$-pairing symmetry. The same gap symmetry was also found in the $CaKFe_4As_4$ system. We found that this series is remarkably similar to the $Ba_{1-x}K_xFe_2As_2$ system in many ways, consistent with other reports in literature. London penetration depth measurements and electron irradiation were also performed on FeSe, which is a unique system in the iron-based superconductor family. Surprisingly, T_c in FeSe was *enhanced* by irradiation which paints a different picture of superconductivity compared to $Ba_{1-x}K_xFe_2As_2$ and $CaK(Fe_{1-x}Ni_x)_4As_4$. However, the FeSe experimental data could still be explained within the (extended) $s_{\pm}$ paradigm. In conclusion, we found a strong evidence supporting the $s_{\pm}$ pairing symmetry which manifested into different gap structures in several representative systems in the iron-based superconductors family.

CHAPTER 1. GENERAL INTRODUCTION

1.1 Basic Overview of Iron-based Superconductors

In the early 2000s following the breakthrough on the research in copper-based (cuprates) material where the superconducting critical temperature (T_c) reached the temperature range above liquid nitrogen, the stage was set in anticipation for another exciting discovery in the field of superconductivity. In the year of 2006 Hosono *et al.* reported a new superconductor (SC) containing iron layers LaOFeP, which has a rather unimpressive T_c of 4 K [1]. Although the material falls into the range of low-T_c SC's, the finding was still quite significant. At that time, the common wisdom to look for a new superconductor compound was to stay away from any magnetic elements (such as iron) following the so-called Matthias' rules [2]. Two years later, a bigger impact came when the same authors published and reported different substitutions in $La(O_{1-x}F_x)FeAs$ ($x = 0.05 - 0.12$) which raised the T_c up to 26 K [3]. This temperature regime is above the range that conventional BCS weak-coupling theory can predict [4], which suggests that Fe-based superconductors (FeSCs) might also belong to the "unconventional" superconductors, putting them in a category similar to the high-T_c cuprates. Consequently, active research with concentrated efforts exploded in that direction. From that point on FeSCs has grabbed the center of attention from the cuprates. Since then a host of different families of FeSCs have been discovered with T_c ranging up to 100 K in certain conditions [5]. In this dissertation I use the term "unconventional" to mean SCs that are non-phonon mediated, as opposed to conventional BCS-type SCs which are phonon mediated. Note that this is a slightly simpler and more relaxed definition compared to the traditionally stricter definition of an unconventional superconductor having a lower symmetry than the lattice.

1.1.1 Families of iron-based superconductors

Now about a decade after the initial excitement one of the ways we classify the different families of iron-based superconductors is by their composition ratios, such as 11 (e.g. FeSe), 111 (e.g. LiFeAs), 122, (e.g. $BaFe_2As_2$), 1111 (e.g. LaOFeAs), 32522 ($Sr_3Sc_2O_5Fe_2As_2$) and finally the recently (2016) discovered 1144 (e.g. $CaKFe_4As_4$) families, see Fig. 1.1(a). Alternatively, it is also common to identify the materials by their elemental components: pnictides which contain As or P and chalcogenides which contain S, Se or Te. Although there is a the tremendous amount of diversity in terms of T_c, phase diagram and competing orders, all iron-based superconductors possess a similar layered structure. As can be seen in Fig. 1.1(a) layers containing iron pnictides or iron chalcogenides are stacked in between the alkali or alkali-earth ions in the crystallographic c-direction. The similarities in their structural pattern to the cuprates which contain CuO layers were pointed early on. The lower dimensionality (planar/2D as opposed to 3D) is speculated to be one of the necessary ingredients for a high-T_c superconductor.

1.1.2 Tuning parameters and phase diagrams

The iron-based superconductors are metallic at ambient conditions, which is very different from the cuprates which are Mott insulators. When cooled down several stoichiometric parent compounds of iron-based superconductors do not undergo the superconducting transitions, and the normal metallic state (which might order magnetically) persists down to zero Kelvin (see, for example, Fig. 1.2(a)). However, if their electronic band structure is in a close proximity to the superconducting instability, then by tuning the material's key parameters (such as substitutional doping, uniaxial strain, hydrostatic pressure or disorder level) the superconducting state may be promoted as the more favorable ground state in the material. This is far from a universal rule however, since in other materials we may encounter the opposite behavior: that superconductivity in a chemically stoichiometric compound is suppressed by increasing/tuning the parameters. These physical parameters have allowed experimentalists to explore the phase space and reveal the underlying rich physics. Some of the published work in selected materials are presented in Fig. 1.2

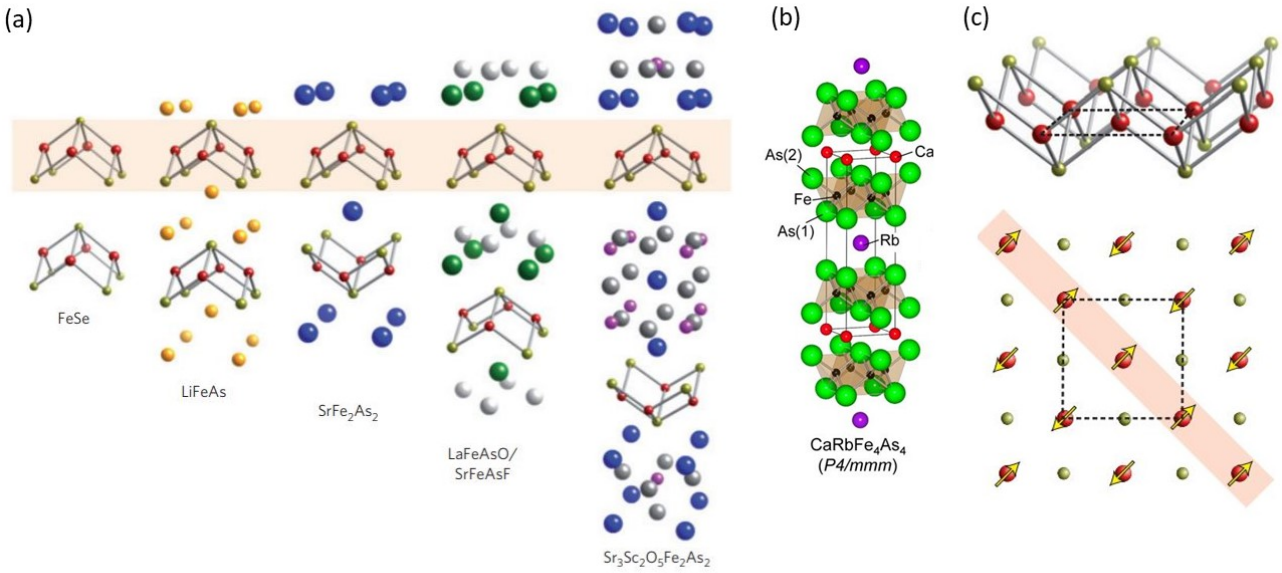

Figure 1.1 The crystallographic and magnetic structure of iron-based superconductors. (a) And (b) examples of tetragonal structure of FeSC, from the left, "11", "111", "122", "1111", "32522" and "1144" families. (c) The planar iron layer common to all superconducting compounds with iron ions shown in red and pnictogen/chalcogen anions shown in gold. The dashed line indicates the size of the 2-Fe unit cell, and the stripe-type spin arrangement is indicated by arrows. (a) And (c) from Ref. [6], (b) from Ref. [7].

(a) - (c), which show examples of T vs doping phase diagrams in different families of FeSCs. Fig. 1.2 (d) - (f) show examples of the effect of pressure and disorder.

Among the examples in Fig. 1.1 the so-called 122 family is one of the most heavily studied materials. This is because the parent compounds of the 122 system are very versatile and responsive to the tuning of physical parameters that we discussed previously. We will revisit this point in further details in Ch. 3, which covers $Ba_{1-x}K_xFe_2As_2$, one of the focus points of this dissertation. Here we will only discuss general features and terminology of the 122 phase diagram, shown in Fig. 1.3.

In a typical FeSC phase diagram, the horizontal and vertical axes represent a tuning parameter and temperature, respectively. In Fig. 1.3 the tuning parameter is chemical substitution but the following discussion is also applicable to the other parameters. At $x = 0$ (non-superconducting parent compound) the system undergoes a magnetic phase transition from paramagnetic to antiferromagnetic (AFM) which is coupled to a structural phase transition from tetragonal to orthorhombic at $T_N \approx T_s \approx 140$ K. As x increases these transition temperatures maintain their coincidence and decrease as one in the K and P doping. However, in $Ba(Fe_{1-x}Co_x)_2As_2$ there is a clear separation between the two temperatures, tracing two distinct lines as x moves away from the origin. The AFM order manifests itself as a stripe-type spin density wave (SDW) arrangement where the magnetic moments of the nearest neighbor Fe atoms in the FeAs layer are aligned in one planar direction, but oppositely oriented in the other planar direction (see Fig. 1.1(b)). Both of the AFM and orthorhombic phase are suppressed as the tuning parameter moves away from $x = 0$. At a certain range of x inside the so-called superconducting dome, the superconducting order parameter emerges. In Fig. 1.3 the x-axis parameter is the doping concentration so the position where the T_c is the highest is called the optimal doping (e.g. $T_c \approx 40$ K for $x \approx 0.4$ in $Ba_{1-x}K_xFe_2As_2$). Compositions below and above this in concentration are called the under- and over-doped regions, respectively.

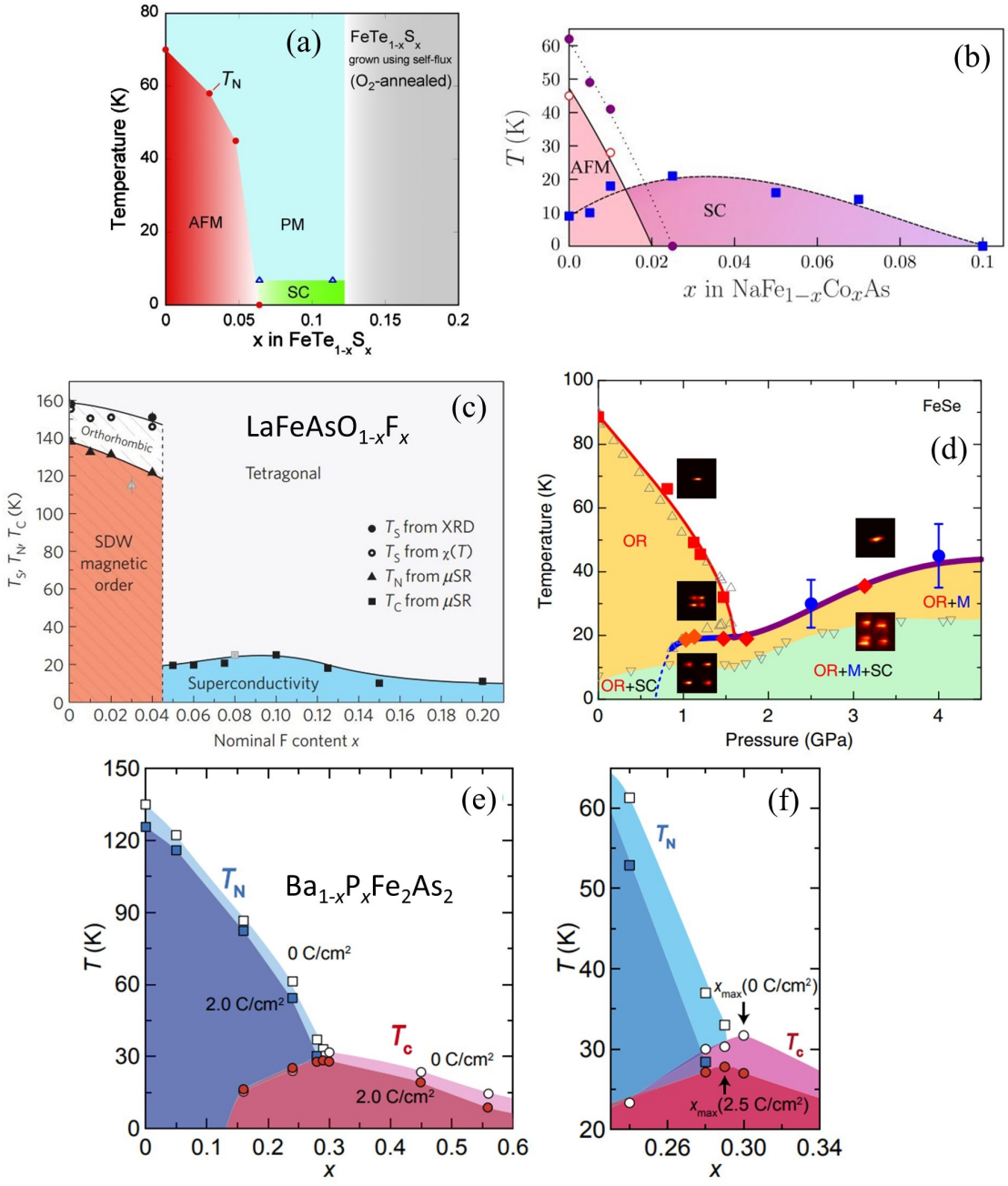

Figure 1.2 Temperature-tuning parameter phase diagrams of iron-based superconductors with tuning parameter: (a) - (c) chemical substitution, (d) pressure and (e) - (f) chemical composition and disorder level. (a) From Ref. [8], (b) from Ref. [9], (c) from Ref. [10], (d) from Ref. [11], (e) - (f) from Ref. [12].

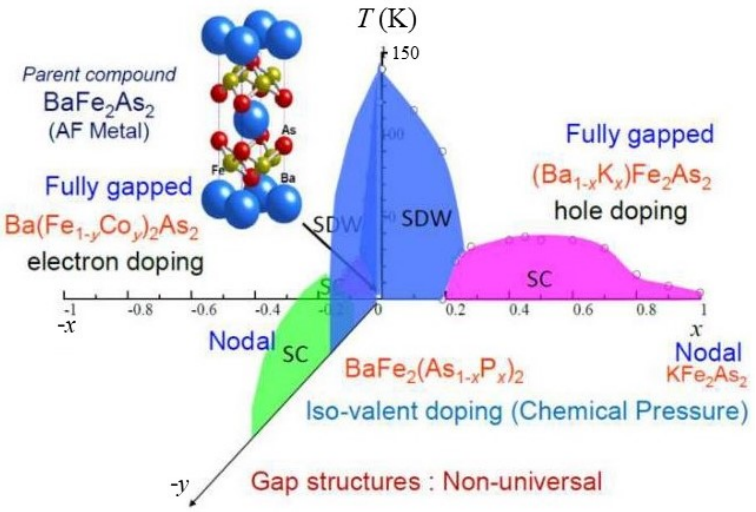

Figure 1.3 Phase diagrams of several systems in the Ba122 family. The negative x-axis shows electron doping by Co substitution, the positive x-axis shows hole doping by K substitution, the negative y-axis shows the isovalent substitution (to increase chemical pressure) by P substitution and the z-axis shows temperature. The AFM phase in the spin density wave (SDW) arrangement is shaded blue and the superconducting domes are shaded green (P doping) and pink (K and Co doping). From Ref. [13].

1.2 Iron-based Superconductors: Energy Gap Structure and Symmetry

Although the families of $BaFe_2As_2$ (Ba122) share the same parent compound, there is a diverse variety of gap structures (Fig. 1.3). In the Co-doped system (Co-Ba122) Co atoms replace some of the Fe atoms adding more electron count. The Fermi surface is fully gapped across the superconducting dome in the *ab*-plane [14], but develops line nodes in the *c*-direction in the underdoped and overdoped edges [15]. In the P-doped compounds (P-Ba122) where P isovalently replaces As, the gap contains nodes in the *ab*-plane that are not due to the symmetry of the order parameter [16] (as opposed to symmetry-imposed nodes in *d*-wave order parameter). Interestingly, the K-doped system (K-Ba122, K adds hole count at Ba sites) exhibits both nodal and nodeless gaps in the *ab*-plane in different regions of the superconducting dome [17, 18, 19] (see Ch. 3 for more details on K-Ba122). Other than the Ba122 family the 122 system has other parent compounds such as $CaFe_2As_2$ (Ca122), $SrFe_2As_2$ (Sr122), with various options of elements to dope them with, such as Na, Ni, Ru, Rh, among others.

The 122 family serves as a good example to show that there are many possibilities of gap structures in unconventional SCs. Therefore an accurate determination of a superconducting gap of a given compound is required. While knowledge of the presence (or absence) of nodes often gives the necessary evidence to narrow down the possibility of potential gap structures, sometimes it may not be sufficient to determine the gap *symmetry*. As illustrated in Fig 1.4, (a) - (d) have different structures but they belong to the same (extended) s-wave symmetry group. Therefore all of them are invariant under 90° rotation. On the other hand, (d) and (e) both have nodes along their gap structure although they belong to different symmetry groups (*s*-wave and *d*-wave order parameter, respectively). Upon 90° rotation the *s*-wave gap symmetry preserves its sign but the *d*-wave reverses sign.

It is essential to investigate the superconducting gap structure along with the gap symmetry as much as possible in order to reveal the pairing mechanism in the unconventional superconductors [20]. Until now there is no universal consensus in the condensed matter physics community regarding the exact pairing mechanism - how and what "glues" the electrons to form into pairs

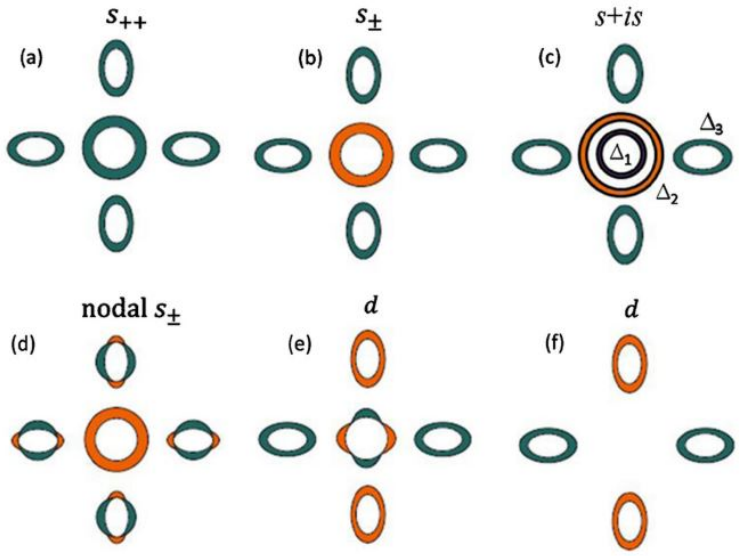

Figure 1.4 Schematic gaps $\Delta(\mathbf{k})$ in FeSC. Color represents phase of $\Delta(\mathbf{k})$. (a) Conventional s-wave (s_{++} state). (b) $s_{\pm}$ state with gap on hole pocket having a different sign than on electron pockets. (c) Antiphase s-wave state possible when two or more hole pockets are present, showing gaps with three different phases. (d) Similar to (b), but with accidental nodes on electron pockets. (e) d-wave state, (f) d-wave state when no central hole pocket is present (nodeless d-wave). From Ref. [20].

in unconventional superconductors, including the cuprate and FeSC families. Although everybody agrees that it is likely that the Fe atoms (with their $5d$ orbitals) play a crucial role in the pairing mechanism for FeSC, there are different schools of thought regarding the exact channel via which the Fe - Fe interaction happens. Unlike in phonon-mediated conventional BCS (Fig. 1.5), promising candidates for the interaction channels in FeSCs include the spin fluctuations (magnons), charge (orbital) fluctuations or a combination/cooperation of both.

1.2.1 Iron-based superconductor - a multiband system

To understand the intricate details of how the different channels play a role in iron-based superconductors we need to review the concepts of multiband superconductivity, starting with the FeSC band structure. For most compounds in the FeSC system (except in a few cases with an extreme doping and topology) measurements by angular resolved photoemission spectroscopy (ARPES) technique and first-principle calculations by density functional theory (DFT) model reveal that there are at least five electronic bands crossing the Fermi surface (FS, see Fig. 1.6(a) - (c)). One or sometimes two located at the center of the Brillouin zone (BZ) have hole-like dispersion relation, and the ones at the corners have electron-like dispersion relation. They are most commonly referred to as hole and electron pockets, respectively. The bands are almost two-dimensional with a cylinder-like shape near the Fermi surface with the cylinder axis points along the c-crystallographic direction. The two dimensionality of the band structure is consistent with the fact that FeSC crystal in real space has a layered structure with a weaker interlayer bond. For experimental purposes, the layered crystals are quite cleavable to expose a fresh and clean surface for the surface-sensitive measurements such as ARPES or STM, which can probe the momentum and real spaces directly. Other experiments such as the inelastic neutron scattering can probe the magnetic structure, with the superconducting state on iron-based superconductors feature a resonance peak at a momentum transfer $\mathbf{Q} = (\pi, \pi)$ [24, 25] which is associated with the wave vector of a long range antiferromagnetic order. This resonance behavior is similar to what is observed in the cuprate system. Although this does not prove that Fe-based superconductivity is mediated by the spin fluctuations, it is sug-

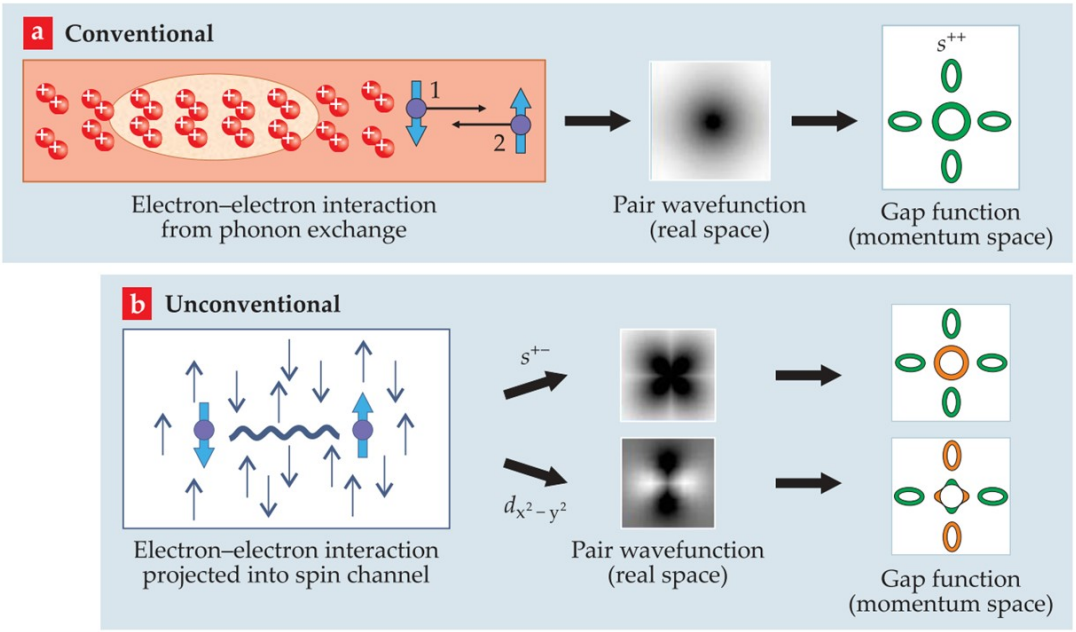

Figure 1.5 Two routes to superconductivity. (a) Two electrons attract each other when the first polarizes a local region (yellow) of the lattice and the second is attracted to that region. The pair wavefunction $\Psi(\mathbf{r})$ (where $\mathbf{r}$ is the relative electron coordinate) has the full symmetry of the crystal and gives rise to a gap function $\Delta(\mathbf{k})$ (where $\mathbf{k}$ is the momentum) with the same sign on the whole FS. (b) Electrons interact with each other via the Coulomb repulsion. In this example the dominant interaction is the magnetic exchange (blue wavy line) arising between opposite-spin electrons due to Coulomb forces. The first electron polarizes the conduction electron gas antiferromagnetically, and a second electron of opposite spin can lower its energy in that locally polarized region. Here $\Psi(\mathbf{r})$ has a node at the origin which minimizes the Coulomb repulsion and can have either $S_{\pm}$ or $d_{x^2-y^2}$ form, as shown. The two possibilities lead to gap functions of varying sign on the FS. From Ref. [21].

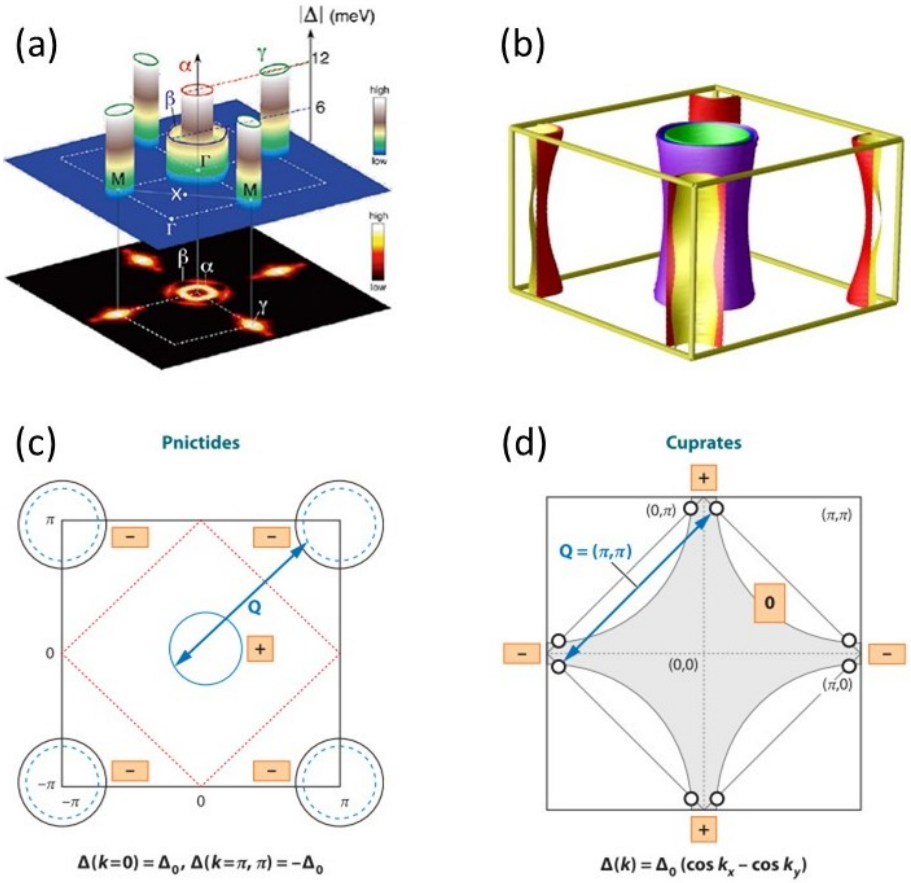

Figure 1.6 Fermi surfaces of FeSCs and the cuprates. (a) A three-dimensional plot of the superconducting gap size (Δ) of $Ba_{0.6}K_{0.4}Fe_2As_2$ measured at 15 K on the three observed FS sheets (shown at the bottom as an intensity plot). (b) The Fermi surface of the nonmagnetic $BaFe_2As_2$ for 10% h-doping (virtual crystal approximation). (c) In FeSCs scattering by antiferromagnetic $\mathbf{Q}$ moves fermions from one FS to the other. Because spin-mediated interaction is positive (repulsive), the gap must change sign between different FSs but to first approximation remains a constant on a given FS. By symmetry such a gap is an s-wave gap, specifically the $s_{\pm}$ because it changes sign between different FSs. (d) In the cuprates the FS is single and large, and $\mathbf{Q}$ connects points on the same FS. In this situation the gap must change sign between FS points separated by $\mathbf{Q}$. Consequently, the gap changes sign twice along the FS. This implies a d-wave gap symmetry. (a) And (b) from Ref. [22], (c) and (d) from Ref. [23].

gestive evidence that spin density waves play a major role in the mechanism of superconductivity in iron-based superconductors.

The general interpretation of the neutron spin resonance itself is that it is a representation of a paramagnon mode of the system [20]. The mode is associated with a magnetic susceptibility which contains an anomalous Green function proportional to the coherence factor

$$\sum_{\mathbf{k}} \left[1 - \frac{\Delta_{\mathbf{k}} \Delta_{\mathbf{k+q}}}{E_{\mathbf{k}} E_{\mathbf{k+q}}} \right] ... \tag{1.1}$$

where ... is the kernel of the BCS susceptibility. A quick glance reveals that this factor vanishes if $\Delta_{\mathbf{k}}$ and $\Delta_{\mathbf{k+q}}$ have the same sign, and is maximized if their signs are opposite. This is why the observation from a neutron spin resonance peak is generally accepted as a "natural" indication of a sign change in the order parameter, i.e. the gap function $\Delta(\mathbf{k})$.

A sign change in the gap function is the crucial element for any electronic mechanism of superconductivity. Since the spin-mediated interaction $U(\mathbf{k}, \mathbf{k}')$ is repulsive (positive), the gap function $\Delta(\mathbf{k})$ has to change sign to extract an overall attractive (negative) component from the BCS gap equation

$$\Delta(\mathbf{k}) \propto \int d\mathbf{k} d\mathbf{k}' U(\mathbf{k}, \mathbf{k}') \Delta(\mathbf{k}') \tag{1.2}$$

with $\mathbf{k}$ and $\mathbf{k}' = \mathbf{k} + \mathbf{Q}$ are two different points in the gapped FS, and $\mathbf{Q} = (\pi, \pi)$ is the momentum transfer wave vector.

Having established that the sign change which is indicated by the neutron spin resonance experiments is actually a necessary ingredient for the mechanism of superconductivity, we can now analyze how it constrains possible candidates for the superconducting gap structure and symmetry in FeSC system. The available symmetries in 2D tetragonal systems (such as the FeSCs) are A_{1g} (s-wave), B_{1g} ($d_{x^2-y^2}$), B_{2g} (d_{xy}), E_g ($d_{xz,yz}$)and A_{2g} ($g_{xy(x^2-y^2)}$ [26]. In the cuprates since the wave vector $\mathbf{Q}$ connects the points in the same FS (see Fig. 1.6(d)), the symmetry is d-wave which changes sign twice along the FS. On the other hand, in iron-based superconductors the FSs are small and $\mathbf{Q}$ connects points from two different bands. Therefore the sign change happens between the hole pocket at the center of the (BZ) and the electron pocket at the corner (Fig. 1.6(c)). This

belongs to the (extended) s-wave symmetry, the $s_{\pm}$ gap structure. For this reason $s_{\pm}$ is the leading candidate for the gap structure in FeSCs, although not everyone is convinced that it is universally applicable to all families in iron-based superconductors.

1.2.2 Derivation of *s*-wave and *d*-wave gaps in a multiband superconductor

From a theoretical viewpoint having multiple bands makes the full-blown, brute force calculations to the system can get very involved, which is not the scope of this dissertation. A reader curious about the different theoretical schemes and microscopic treatments about iron-based superconductors may refer to the collection of review papers written by excellent theorists [20, 23, 27, 28] for further details. In this section we will only consider a theoretical "toy" FS model that simplifies the situation into three distinct bands (one hole pocket and two electron pockets) while still capturing the essential physics to get the fundamental insights about FeSCs. The discussion is derived from [23].

We start with the multiband electronic structure as observed by experiment as input and restricting ourselves only to 1-Fe BZ. The difference between 1-Fe (unfolded) and 2-Fe (folded) BZs are shown schematically in Fig. 1.7(b) and (c). The folded version contains two Fe atoms and takes into account the two inequivalent As sites (1.7(a) blue square [real space], 1.7(b) [momentum space]) so it is physically more meaningful. However, the unfolded version (1.7(a) green square [real space] 1.7(c) [momentum space]) still captures the fundamental interactions and is easier to work with. If (for simplicity) the potential difference from the two inequivalent interactions can be neglected, the difference between the two BZs becomes purely geometrical. In the momentum space the axes of the unfolded BZ are rotated 45° from their folded counterparts.

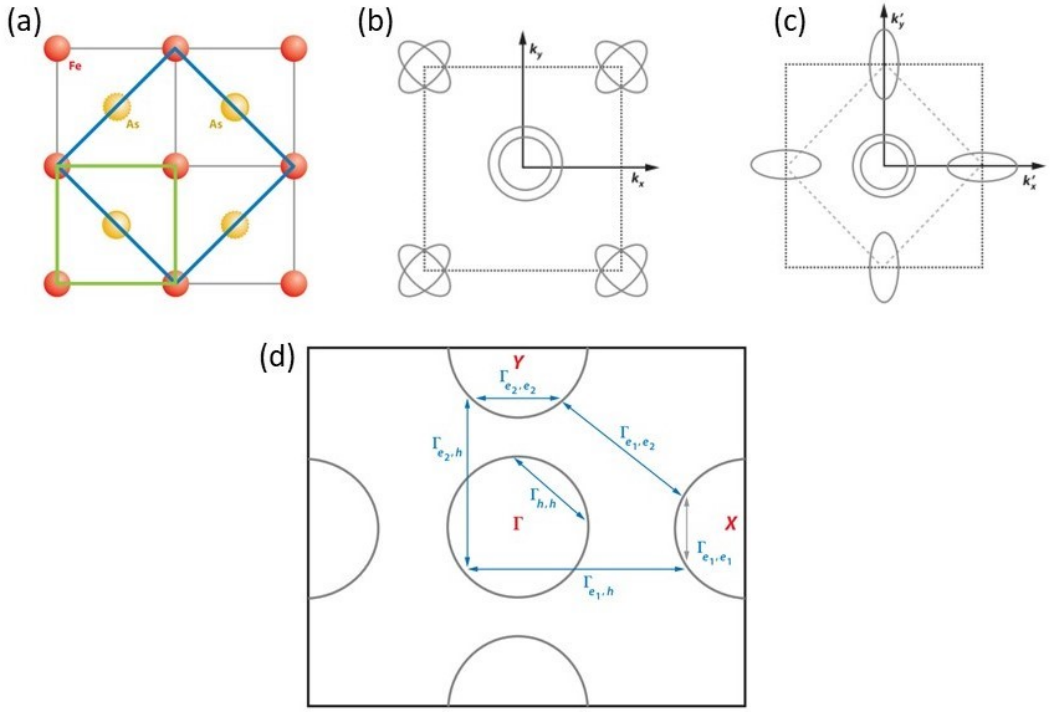

Figure 1.7 Real and momentum space structures of iron-based superconductors. (a) If only Fe states are considered, an elementary cell containing one Fe atom is marked by a green square. The actual unit cell (blue) contains two Fe atoms because two inequivalent positions of a pnictide above and below the Fe plane (solid and dashed As circles). (b) The location of hole and electron FSs in a 2D cross section in the folded Brillouin zone (BZ) with 2-Fe cell, (c) and in the unfolded BZ with 1-Fe cell. (d) Intrapocket and interpocket interactions in a four-band 2D model for FeSCs. For simplicity only one hole FS is shown. Γ, X and Y points are (0,0), (π,0) and (0,π), respectively. $\Gamma_{h,h}$ is the hole intrapocket interaction. $\Gamma_{e_1,h}$ and $\Gamma_{e_2,h}$ are interpocket interactions between a hole and an electron pocket. Γ_{e_1,e_1}, Γ_{e_2,e_2} and Γ_{e_1,e_2} are intrapocket and interpocket interactions involving the two electron pockets. (a) From Ref. [23], (b) and (c) from Ref. [29], (d) from Ref. [30].

A generic low-energy BCS-type model in the band basis is described by

$$H = \sum_{i,\mathbf{k}} \epsilon_i(\mathbf{k}) a^\dagger_{i\mathbf{k}} a_{i\mathbf{k}} + \sum_{i,j,\mathbf{k},\mathbf{p}} \Gamma_{i,j}(\mathbf{k},\mathbf{p}) a^\dagger_{i,\mathbf{k}} a^\dagger_{i-\mathbf{k}} a_{j\mathbf{p}} a_{j-\mathbf{p}} \tag{1.3}$$

The first sum describes low-energy excitations near hole and electron FSs with $a^\dagger_{i\mathbf{k}}$ ($a_{i\mathbf{k}}$) as the creation (annihilation) operator for an electron with momentum $\mathbf{k}$ and band index i. The second sum describes the scattering of a pair $(k\uparrow, -k\downarrow)$ on the FS i to a pair $(p\uparrow, -p\downarrow)$ on the FS j. These interactions are either intrapocket (hole-hole Γ_{hh} or electron-electron $\Gamma_{e_ie_i}$, assuming only one hole pocket for simplicity) or interpocket interactions (hole-electron Γ_{e_ih} or electron-electron $\Gamma_{e_i\neq e_j}$). This is illustrated in Fig. 1.7(d).

If we assume that the Γs are frequency independent, then the gap function $\Delta(\mathbf{k})$ also does not depend on frequency. In this case the gap equation becomes an eigenfunction/eigenvalue problem

$$\lambda_i \Delta_i(k) = -\int \frac{dp||}{4\pi^2 v_{\mathbf{p}_F}} \Gamma(\mathbf{k}_F, \mathbf{p}_F) \Delta_i(p) \tag{1.4}$$

where Δ_i are the eigenfunctions and λ_i the eigenvalues. If one or more λ_i are positive, the system is unstable toward superconducting pairing with the corresponding $T_{c,i} = \Lambda_i e^{-1/\lambda_i}$. Because of the exponential dependence on $1/\lambda_i$, the solution with the largest positive λ_i will emerge first and establish the pairing state, immediately below its T_c.

To solve 1.4 we need to express $\Gamma(k,p)$ in the basis functions of one of the representations of the tetragonal group (A_{1g}, B_{1g}, etc, see the paragraph below Eq. 1.2). For example, the s-wave (A_{1g} representation) component of $\Gamma(k,p)$ can be quite generally expressed as

$$\Gamma^{(1g)}(k,p) = \Gamma_s(k,p) = \sum_{m,n} A^s_{mn} \Psi^s_m(k) \Psi^s_n(p) \tag{1.5}$$

where $\Psi^s_m(k)$ are the basis functions of the A_{1g} symmetry group: 1, cos k_x cos k_y, cos k_x + cos k_y, etc., and A^a_{mn} are the coefficients. By expanding $\Psi^s_m(k)$ near (0,0) and $\Psi^s_n(p)$ near (0,π) in the BZ which are the locations of the hole and electron pockets and keeping only the leading terms, we get

$$\Psi^s_m(k) \approx a_m \quad \text{and} \quad \Psi^s_n(p) \approx b_n \pm b_n \cos 2\phi_p \tag{1.6}$$

with the upper sign for an electron pocket at (0,π) and the lower for the other one at (π,0).

Using 1.6 to express $\Gamma_s(k,p)$ in 1.5 and substituting them to solve the eigenfunction equation 1.4, we get the expression for the gap functions of FeSC in the s-wave symmetry

$$\begin{aligned}\Delta_h^{(s)}(k) &= \Delta_{h0}\ (k-\text{independent})\\ \Delta_e^{(s)}(k) &= \Delta_{e0}\ (1 \pm r\ \cos\ 2\phi_k)\end{aligned} \tag{1.7}$$

The gaps along the hole FS are angle independent, but the gaps along the two electron FSs may acquire accidental nodes depending on the ratio of the two prefactors. Here r is the anisotropy parameter. When $r \geq 1$ then nodes appear at accidental values of ϕ, which are not protected by symmetry and could be different between the two electron FSs.

Doing the same exercise in the B_{1g} representation yields the gap functions in the $d_{x^2-y^2}$ symmetry,

$$\begin{aligned}\Delta_h^{(d)}(k) &= \Delta_{h0}\ \cos\ 2\phi_k\\ \Delta_e^{(d)}(k) &= \Delta_{e0}\ (\pm 1 + r\ \cos\ 2\phi_k)\end{aligned} \tag{1.8}$$

Along the hole FS the gap behaves as a conventional d-wave gap with four nodes along the diagonals. Along the electron FSs the two gaps differ in the sign of the angle-independent terms and have in-phase cos 2ϕ oscillating components. When $r \ll 1$ the two gaps are simply plus and minus gaps, but when $r \geq 1$ then again accidental nodes appear.

Therefore we see that the geometry of the FSs in the FeSCs affects the gap structure in a fundamental way: Because electron FSs are centered at (0,π) and (π,0) points and not along BZ diagonals, s-wave gaps on these FSs have cos 2ϕ oscillations that one normally would associate with a d-wave symmetry, and d-wave gaps have constant (plus-minus) components that one would normally associate with an s-wave symmetry. When these "wrong" components are large, the gaps develop accidental nodes. Thus these nodes may be present or absent for both s-wave and d-wave gaps, regardless of the symmetry constraints [23].

1.2.3 Brief overview of experimental methods to probe the energy gap structure and symmetry

To probe the superconducting gap structure one needs to access the states below T_c which rules out electronic transport (resistivity) measurement immediately. It is still a very useful probe of the normal (metallic) state properties above T_c though it usually needs to be used in conjunction with other methods when studying a superconductor material. At present day, there are various experimental tools in the physicists' arsenal that can probe the surface (such as ARPES and STM) and thermodynamics (such as heat capacity and quantum oscillations) states. This section is an introduction to a few selected experimental probes that are widely used today, but it is not by any means an exhaustive list. The section will close with the discussion of London penetration depth which is the main characterization technique used for the studies in this dissertation.

1.2.3.1 Angle-resolved photo-emission spectroscopy

ARPES is probably the most direct probe of the superconducting gap structure because it is able to observe the low energy quasiparticle excitations. It uses a laser to knock out loosely bound electrons and record their angular and energy distribution. The technique can resolve both the FS structure in the momentum space and the spectra of the electronic states near the Fermi energy. The data from ARPES measurements have been used to verify the band structure calculations that predict the size, shape and position of the FS pockets of FeSC in the momentum space (see Fig. 1.6(a) and (b)). On the limitation side, ARPES laser only penetrates a few lattice parameters deep and therefore the quality of the sample's surface is of paramount importance. This is the reason why an ARPES set up is usually equipped with a mechanism to cleave the sample *in situ*, inside its ultra-high vacuum (UHV) chamber space. A successful cleaving exposes a fresh, contaminant-free surface that is ready to be measured. Due to its nature as a surface probe, the data gleaned from ARPES has to be analyzed in the right framework by taking into account the surface conditions, surface reconstruction energy and other variables before making interpretations about the bulk

properties of the material. Another obvious limitation of the ARPES technique is that it can only map out states below the Fermi energy and all the states above the Fermi energy are "invisible".

1.2.3.2 Scanning tunneling microscopy

The complement of the momentum space mapping using ARPES is of course, the STM that maps out real space. The technique uses a sharp conducting tip biased at potential V and positioned close to the surface. The electrons that tunnel between the tip and the surface are proportional to the local electronic density of states. Depending on the chosen experimental parameters while scanning a desired area, STM can produce a map that shows the local distribution of elemental atoms, impurities, magnetic vortices, etc. In order to gain information about the gap structure in the momentum space the STM image can be further processed using the Fourier transformation, and this is called quasiparticle interference (QPI) technique. Any kind of impurity or defect in the metal gives rise to Friedel oscillations of the charge and spin and density around the imperfection, which are reflected in the QPI image. After the Fourier transformation the QPI image can be used to cross-reference the ARPES data to highlight their similarities and differences. The STM/QPI also suffer from the same limitations as other surface probes, which is usually remedied by having the *in situ* cleaving mechanism to get the best surface possible.

1.2.3.3 Heat capacity and thermal conductivity

The low temperature heat capacity of a material is given by

$$C = \gamma T + \beta T^3 \tag{1.9}$$

where γ, β are the electronic (Sommerfeld) and phonon contribution coefficients, respectively. In a conventional weak-coupling (BCS-type) SC, the gap is single and isotropic. In this case, there is a well-known relation between the heat capacity jump at T_c, γ and T_c itself, given by $\Delta C|_{T_c}/(\gamma T_c) = 1.43$. In the case of a new superconducting material with an unknown gap, the heat capacity data comparison to the BCS curve has been used to infer whether the new material is likely to have a conventional s-wave gap structure or otherwise. More specifically, if C/T saturates

to zero as $T \to 0$ the FS is commonly interpreted as fully gapped. The full gap scenario indicated by a saturation at low temperature extends to other probes that similarly rely on the population abundance of the quasiparticles (the unpaired electrons) such as London penetration depth. Since the temperature dependence follows a thermally activated behavior (Boltzmann distribution function), an exponential behavior which has strong saturation at low temperature is usually accepted as a strong indication of the a fully gapped FS, provided a clean material and the base temperature of the experiment is sufficiently far below T_c.

The thermal conductivity of a material at low temperatures is given by

$$\kappa = aT + bT^{\alpha-1} \tag{1.10}$$

where the first term comes from the conduction electrons and the second term comes from the phonon and magnon contributions. For a superconductor, the residual linear term κ/T ($T \to 0$) is used to distinguish the presence/absence of nodes in the gap structure. If nodes are present (absent), κ/T is approaching a finite value (zero) when extrapolated to $T \to 0$. To achieve a good confidence in determining the value of the residual linear term, a dilution refrigerator is sometimes required to reach a base temperature in the tens of mK range.

An application of magnetic field may also provide insight about the gap topography. For a gap without nodes or deep minima, the rise in κ as a function of applied field H is very slow because it relies on tunneling between quasiparticle states localized on adjacent vortices. By contrast, a superconducting gap that develops deep minima but non-zero anywhere in FS will show saturation behavior at $H = 0$, then rise rapidly at the application of field. The work by Tanatar *et al*. on Co-Ba122 system is an example that shows both behaviors, concluding that the gap anisotropy strongly depends on the doping composition [14].

Another advantageous feature of thermal conductivity experiments is that it is directional. Therefore it is possible to do an angular dependence study of the gap structure and uncover the nodal directions. For a few special scenarios, this capability may provide the crucial evidence for distinguishing between the symmetry-imposed vs accidental nodes since the symmetry-imposed nodes (such as *d*-wave) are tied to specific locations. Not only limited to the *ab*-plane, the heat

current can also be directed along the c-axis to explore the 3D nature of the FeSC gap structure (e.g. in the work of Reid *et al.* in Co-Ba122 system [15]).

1.2.3.4 London penetration depth

The London penetration depth, λ_L, is the characteristic length scale of the exponential decay of externally applied magnetic field inside a superconductor due to Meissner screening [31]. There are several methods to experimentally measure λ_L for instance using magnetic force microscopy (MFM), the cavity perturbation technique, using muon-spin rotation (μSR), etc. Each method has more or less its own strengths and weaknesses. In this work the London penetration depth was measured using the tunnel-diode resonator (TDR) technique, which will be discussed in details in Section 2.2. As a summary, the advantages of using the TDR method are as follows: its relatively small size allows mounting the set up to a dilution refrigerator to reach sub 100 mK temperature, the ability to apply external magnetic field to access both London and Campbell states in both the in-plane (ab) and out-of-plane (c) directions, and the part-per-billion (ppb) precision that may translate to Angstrom scale precision. On the other hand, the disadvantage of the TDR method is its inability to easily measure the absolute value of penetration depth. Instead the data is usually given as the change in penetration depth $\Delta\lambda_L(T) = \lambda_L(T) - \lambda_L(T_{base})$ where T_{base} is the experimental base temperature. To get the absolute penetration depth $\lambda(T)$ we need to fix $\lambda(T_{base})$ to a reference point. When T_{base} is low enough (sub-Kelvin range) we may take the penetration depth at 0 K [$\lambda(0)$] as the reference point. $\lambda(0)$ is an important parameter of the material (see Ch. 2 for more details) which needs to be independently determined from other experimental methods. Prozorov *et al.* [32] developed a method to measure $\lambda(0)$ using a TDR setup where the sample needs to be coated with a thin layer of aluminum [33, 34] with the penetration depth measurements taken before and after the coating.

The relation between London penetration depth to the density of paired electrons responsible for the supercurrent is given by $\lambda_L^{-2}(T) \propto n_s(T)$. Since the total count of electrons are conserved ($n_{total} = n_{qp} + n_s$), the increase of λ_L due to temperature is considered as a measure of the increase

of the excited quasiparticles whose pairs are broken and they behave like normal electrons. The behavior of the excitations depends closely on the gap structure and therefore provides evidence for the presence of shallow gap minima, midgap states or nodal structures, with the same line of reasoning discussed in the heat capacity section. In a conventional (s-wave) SC the gap magnitude Δ is isotropic and approximately temperature-independent below 0.3 T_c (Fig. 1.8(a)). In this case, the temperature dependence of London penetration depth is exponential as derived from the BCS theory [35]

$$\frac{\Delta\lambda_L(T)}{\lambda_L(0)} \approx \sqrt{\frac{\pi\Delta(0)}{2k_{\rm B}T}}\ \exp -\frac{\Delta(0)}{k_{\rm B}T} \tag{1.11}$$

where $\lambda_L(0)$ and $\Delta(0)$ are the penetration depth and gap magnitude at 0 K, respectively. On the other hand, a nodal gap would have linear T-dependence due to the immediately accessible states for the excited quasiparticles. For a clean d-wave measured in the ab-plane, the temperature dependence is given by [36]

$$\frac{\Delta\lambda_L(T)}{\lambda_L(0)} \approx \frac{2\ \ln 2}{\alpha\Delta(0)}T \tag{1.12}$$

where α depends on the functional form of Δ near nodes [37]. For additional details on the theory of London penetration depth, see Section 2.1.

Since s-wave and d-wave gaps have their own T-dependent signature, the low temperature part ($T/T_c \leq 0.3$) of $\Delta\lambda_L(T)$ can provide an insight about the gap structure (Fig. 1.8(b)). A quick and practical way to analyze the T-dependence is to put it in the power-law form $\Delta\lambda_L(T) \propto T^n$ [33, 40, 41]. A high exponent ($n > 3$) is indicative of a fully gapped FS since it is practically indistinguishable from an exponential function [Fig. 1.8(c), red curve (Nb)]. On the other hand, a close to linear ($n < 1.5$) T-dependence has been interpreted as evidence of the presence of nodes somewhere in the gap function [Fig. 1.8(c), blue curve (BSSCO)].

For an exponent that falls around ~ 2 the interpretation is not as straightforward. A gap function with various degrees of angular anisotropy (from a gap with deep minima but nodeless, to a gap with weak anisotropy) may give exponent between 1.5 and 3. For example this was demonstrated in the K- and Co-doped Ba122 systems by Kim *et al.* [19] and Tanatar *et al.* [14], respectively. Furthermore, a quadratic T behavior may also arise from impurity scattering inside the

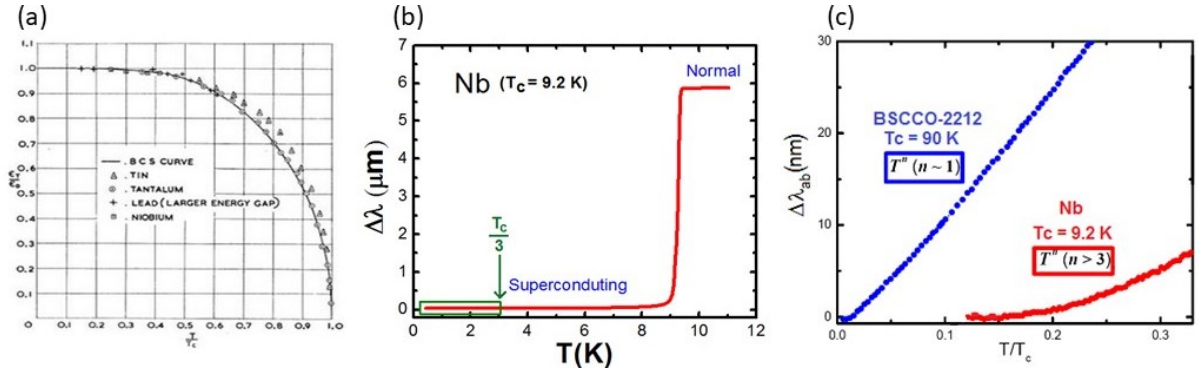

Figure 1.8 Temperature-dependent BCS gap magnitude and London penetration depth. (a) Theoretical BCS prediction as compared to experimentally determined energy gap magnitude in elemental SCs against normalized temperature. (b) The change in London penetration depth $\Delta\lambda_L(T)$ in Nb. (c) Zoom of the low temperature $\Delta\lambda_L(T)$ in the nodal BSSCO and nodeless Nb to contrast their exponents extracted from power-law fitting. (a) From Ref. [38], (b) and (c) from Ref. [39].

sample, which create the midgap density of states [42]. By increasing the impurity scattering, the gap structure can be driven into a gapless or near-gapless regime, which will result in the quadratic T-dependence [43] regardless of the pristine state having $n \approx 1$ (nodal) or $n > 3$ (nodeless) [33]. This argument has been used to explain the T^2-dependence as a "dirty" d-wave in early cuprate crystals [42]. Therefore both the anisotropy and the impurity levels may affect the exponent independently and deserve a careful interpretation.

Because different gaps respond differently to different types of disorder, disorder in itself can be used as a probe of the gap structure. In the following Section 1.3 we will discuss the effects of disorder on superconductivity more thoroughly. For now, we will conclude this section by acknowledging the need to use more than one experimental probe (sometimes via collaboration) to gain a good understanding of the material of interest. The findings based only on one technique may not be sufficient to paint the whole picture. Only by comparing and contrasting data from several experimental probes (surface, transport, thermodynamics, etc.) that we are able to get more or less a reliable picture.

1.3 Effects of Disorder on Superconducting Critical Temperature and Low Temperature London Penetration Depth for Different Gap Structures.

Real crystals are not perfect. Even the best crystal ever grown contains various types of crystallographic defects, such as unintended chemical impurities, deficiencies, inclusions, or internal stress/strain and so on. For this reason it is necessary to research and study the role of disorder in various types of material. By gaining a good understanding on the interplay between disorder and a specific property in the material of interest (e.g. superconductivity), it is then possible to manipulate them to our advantage. But as one can imagine, the possible combinations of disorder and material types are almost limitless. Hence in this section we will eventually limit our scope to a specific type of disorder that is used to study the gap structure of a superconductor.

1.3.1 Basic overview of different types of disorder

The defects listed in the opening paragraph of this section are considered as growth defects since they are present in the freshly grown crystals even with the grower's best efforts to minimize them. Another concept related to the crystal growth process is the chemical substitution disorder. These are the defects that may play a significant role in non-stoichiometric compounds, e.g. $Ba_{1-x}K_xFe_2As_2$. In these chemically substituted compounds it is usually impossible to decouple the effects of the desired chemical composition from the (sometimes undesired) accompanying change in the electronic band structure, chemical potential, chemical pressure on the lattice parameters and compositional homogeneity in the sample, etc. Therefore the disorder due to both growth and chemical substitution are considered to be innate to the sample, and are sometimes too complicated to interpret or quantify in a theoretical model. On top of that, they lack the degree of freedom necessary for a systematic study of disorder.

What is more desirable is a kind of disorder that can be tuned (like turning a knob). One can imagine the case where a specimen is prepared with the innate (growth and substitutional) defects taken as the baseline. The sample properties are measured from this baseline. Then we turn the "knob" to add a controlled amount of artificial disorder, and the sample is measured again

to quantify the changes in its properties. This would open up a whole new phase space for research exploration. Practically, we are accessing another parameter axis in the phase space to play with, on top of the usual physical parameters available in the experiment such as temperature, magnetic field, pressure and so on. So how does one access this parameter? One way to access this parameter is by particle irradiation. Accelerated particles (heavy ions, protons, electrons etc.) with enough kinetic energy can generate defects from the collision with the target sample. The formula for the maximum transferable energy by energetic particles is

$$E_{p,max} = \frac{2E\Big(E + 2mc^2\Big)Mc^2}{\Big((m+M)c^2\Big)^2 + 2EMc^2} \tag{1.13}$$

Eq. 1.13 gives the maximum energy transferred by accelerated incident particles (of rest mass m and energy E) to target atoms of mass M [44]. Different types of defects may form depending on the mass, kinetic energy and charge of the incident particles that bombard a given material. Fig. 1.9(a) shows the predicted defects formed when the target material contains Fe atoms (such as iron-based superconductors). On the heavier side, ion irradiation such as Pb^+ or Au^+ have large rest mass energy that they are known to create columnar defects, which may be useful for vortex-pinning related research (Fig. 1.9(b)). Moderately massive particles like α-particles, neutrons and protons with sufficient kinetic energy create clusters of defects due to cascades of secondary collisions after the initial impact (Fig. 1.9(c)). Electrons, on the other hand, are the only particles that reliably create homogeneous point-like disorder in a material due to their small masses and large charge (Fig. 1.9(d)). A head-on collision with an electron in the MeV range can knock an atom out of its ground state lattice position, creating a vacancy-interstitial (Frenkel pair) defect. The effect of electron irradiation with different energies on different systems including metals and their compounds has been previously studied in great detail [44, 45, 46].

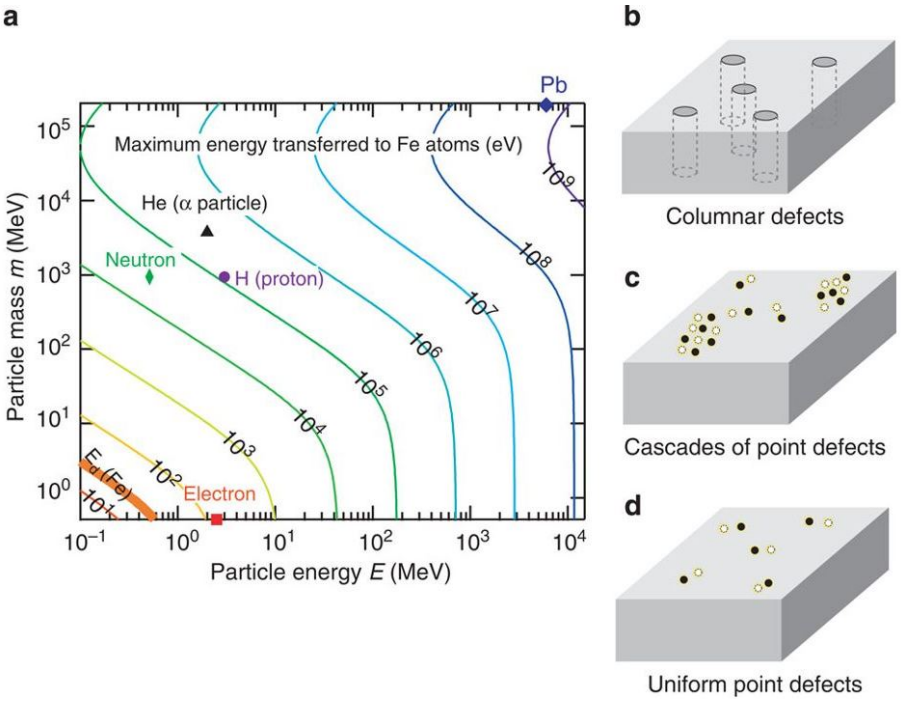

Figure 1.9 The contour plot of maximum energy transferred to Fe atoms (recoil energy) for irradiated particles with rest mass m and incident energy E. The typical threshold energy E_d for the displacement of Fe atoms from the lattice is marked by the thick orange line. The typical energies for electron (red square), neutron (green diamond), proton (purple circle), α-particle (black triangle) and heavy-ion Pb (blue diamond) irradiation are indicated. Owing to its small mass, the recoil energy of the electron irradiation used in this study is orders of magnitude smaller than those other particle cases. (b) Schematic illustrations of columnar defects which can be created by heavy-ion irradiation. (c) Particle irradiation with relatively large recoil energies tends to have cascades of point defects due to successive collision of atoms. (d) Electron irradiation with a small recoil energy is the most reliable way to obtain uniform point defects. From Ref. [16].

1.3.2 Effects of non-magnetic, point-like disorder on superconducting critical temperature

In this section we will discuss how the concentration of defects in a material affect superconductivity. One of the earlier studies on the effects of impurity in a superconductor was done by Philip Anderson in 1959 from which the famous Anderson's theorem originated [47]. The theorem states that the gap amplitude $|\Delta|$ and the superconducting critical temperature T_c of an isotropic BCS-type superconductor are insensitive to non-magnetic impurities. The complementary works by Abrikosov-Gor'kov in 1960 revealed that magnetic impurities on the other hand, are strong pair-breakers in a conventional BCS superconductor [48]. In this case T_c and $|\Delta|$ are quickly suppressed even at low impurity concentration. A hand-waving argument can explain why magnetic impurities are strong pair-breakers; as one of the electrons that make up a Cooper pair with spin singlet ($S = 0$) scatters off a magnetic impurity, it has to change its momentum *and* flip its spin orientation. Since both electrons now have their spins pointing in the same direction, the Cooper pair is broken. Non-magnetic impurities on the other hand, do not force a spin flip on the electron thus preserving the Cooper pair. The situation quickly becomes complicated however, if we consider cases beyond a single isotropic BCS-type gap. For superconductors that have anisotropic gaps, multiple gaps or other gap symmetries even non-magnetic impurities may cause significant changes in the superconducting state.

1.3.2.1 Single band case

To turn the hand-waving argument into a more quantitative model we consider T_c suppression of a single gap SC by non-magnetic impurities, using the Abrikosov-Gor'kov formula [49, 50]

$$\ln\left(\frac{T_{c0}}{T_c}\right) = \Omega\left[\varphi\left(\frac{1}{2}+\frac{\mu}{2}\right) - \varphi\left(\frac{1}{2}\right)\right] \tag{1.14}$$

where $\mu = \hbar\ (2\pi k_{\mathrm{B}} T_c \tau)^{-1}$ and $\varphi(x)$ is the digamma function. In mathematics, the digamma function is defined as the logarithmic derivative of the gamma function $\Gamma(x) = \int_0^\infty z^{x-1} e^{-z} dz$ [51]

$$\varphi(x) = \frac{d}{dx}\ \ln\Gamma(x) = \frac{\Gamma'(x)}{\Gamma(x)} \tag{1.15}$$

It also has an integral representation as

$$\varphi(x) = \int_0^\infty \left(\frac{e^{-t}}{t} - \frac{e^{-xt}}{1-e^{-t}} \right) \mathrm{d}t \tag{1.16}$$

τ in the expression for μ is the relaxation time of non-magnetic impurities scattering which is related to the concentration of the impurities. Ω in Eq. 1.14 is the gap anisotropy defined as

$$\Omega \equiv 1 - \frac{\langle \Delta(\mathrm{k}) \rangle^2}{\langle \Delta(\mathrm{k})^2 \rangle} \tag{1.17}$$

It is evident from a quick glance that an isotropic superconducting gap (e.g. isotropic s-wave) has $\Omega = 0$, while for an anisotropic gap, $0 < \Omega < 1$ (d-wave has $\Omega = 1$). This is why the non-magnetic impurities do not break paired electrons for an isotropic gap but anisotropic gap. To get a more explicit dependence due to the impurity concentration, 1.14 can be simplified to

$$\frac{T_c}{T_{c0}} = 1 - \frac{\pi\hbar}{8k_\mathrm{B}} \frac{1}{\tau} \tag{1.18}$$

the critical scattering rate where superconductivity is completely suppressed ($T_c = 0$) is defined as $1/\tau_c = 8k_\mathrm{B}/\pi\hbar$.

To experimentally measure τ directly is far from trivial. However, it is generally possible to measure the residual resistivity increase due to impurities $\Delta\rho_0$, which is related to $1/\tau$ according to Drude's model

$$\frac{1}{\tau} = -\frac{ne^2\Delta\rho_0}{m^*} \tag{1.19}$$

m^* is the effective mass with a value between $2m_e$ and $4m_e$ in the 122-type iron-based superconductors taken from ARPES measurements [52, 53]. Residual resistivity ρ_0 is the value of resistivity extrapolated $T \to 0$ and it directly corresponds to the amount of scattering centers in the material. To extract ρ_0 from a temperature-dependent resistivity measurement $\rho(T)$ we need to fit a power-law relation at a limited temperature range above T_c (see Fig. 1.10).

$$\rho(T) = \rho_0 + AT^n \tag{1.20}$$

Particle irradiation induces artificial disorder which adds to the pre-existed temperature-independent disorder in the material. This effectively increases ρ_0 which raises the $\rho(T)$ curve. If the upward

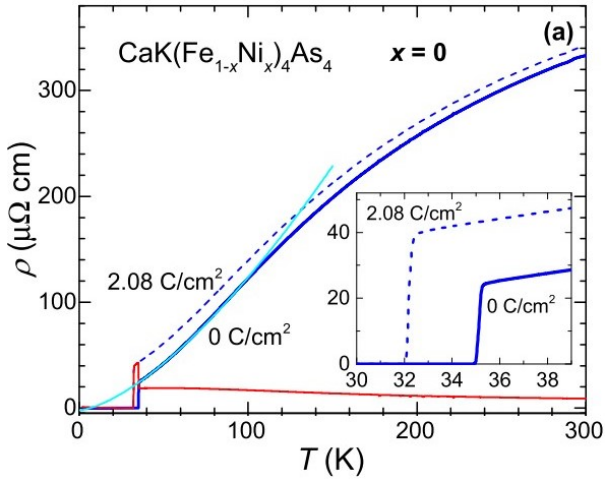

Figure 1.10 In-plane resistivity data of the stoichiometric $CaKFe_4As_4$ sample. Solid and dashed lines show resistivity of the sample before and after irradiation, with the dose of 2.08 C/cm^2. The red line shows the difference of resistivity between irradiated and pristine states. The cyan line is the fit of the curve in the pristine state to $\rho(0) + \rho_T T^{3/2}$. The right inset zooms on the superconducting transition range. From [55].

shift is parallel in the whole temperature range then it follows the so-called Mathiessen's rule [54], which is generally observed in FeSC family.

So now we have the essential tools to develop an experimental procedure to better characterize the T_c suppression against disorder. By using particle irradiation and measuring the specimen's resistivity before and after the irradiation run, we can obtain the suppression rate of T_c/T_{c0} vs $\Delta\rho_0$. To improve the experimental accuracy, the contacts for wires in the standard four-probe configuration should be preserved during irradiation. In this way, the error associated with the contacts' resistance can be minimized since the same soldered contacts are used before and after irradiation. Our group has followed this procedure whenever possible, with several of the results discussed later.

1.3.2.2 Multiband case

Since iron-based superconductors have multiband nature, a different model is needed to predict the behavior T_c suppression due to disorder. In this case the calculations become more complex since

they have to include more parameters and assumptions for the intra- and interband interactions. One of the earlier works on FeSC T_c vs impurity is by Onari and Kontani [56]. The main result of their work is summarized in Fig. 1.11. They proposed that the $s_{\pm}$ gap is very susceptible to any impurities (even the non-magnetic ones) due to the presence of interband scattering term. They modeled impurities in the form of chemical doping and their calculation estimated that $s_{\pm}$ gap vanishes when the doping concentration reaches 1% or roughly $\Delta\rho_0 \approx 20\ \mu\Omega$ cm. On the other hand, the s_{++} gap is very robust against impurity effects, with only weak pair-breaking due to the difference in the gap magnitudes.

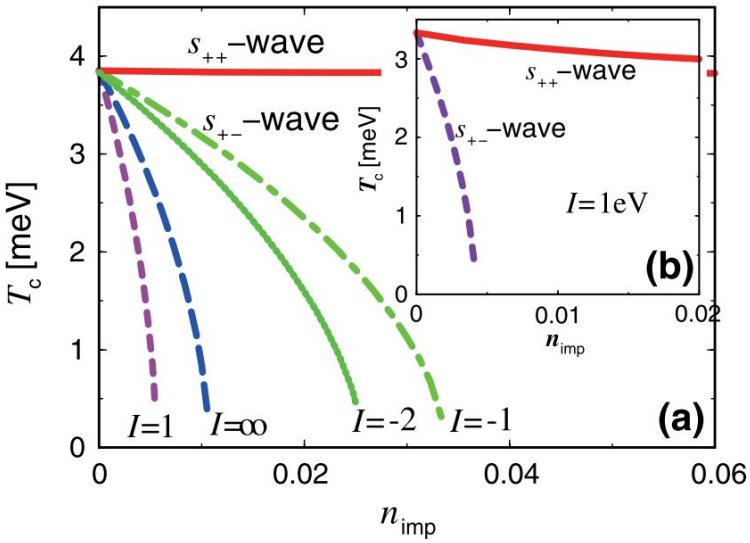

Figure 1.11 Calculated T_c for the $s_{\pm}$-wave and s_{++}-wave states as functions of the impurity concentration n_{imp} with two different sets of $g_{1,2}$ for (a) and (b). Parameters used in (a) $g_{1,2} = 2$ eV ($T_{c0} = 46$ K) and (b) $g_1 = 3g_2 = 3$ eV (the superconducting $T_{c0} = 40$ K). I represents the scattering strength and $g_{1,2}$ are the coupling parameters for interband scattering off the hole $FS_{1,2}$, respectively. In either case, the s_{++} model is much more robust compared to model $s_{\pm}$. More details of the model and calculations can be found from Ref. [56].

Subsequent works on T_c suppression on iron-based superconductors by disorder with different sets of parameters (e.g. Efremov *et al.* [57] and Wang *et al.* [58]) also arrive at conclusions that are qualitatively similar to our prior discussions; First, the $s_{\pm}$ gap is generally more susceptible to disorder compared to s_{++}, unless when intraband scattering completely dominates (the ratio

of interband/intraband $\rightarrow$ 0). This intuitively makes sense since if interband interactions are turned off to zero and scattering happens mainly between particles in the same band then whether there is sign change between bands makes essentially little difference. The second conclusion, in direct analogy to the single band counterpart is that anisotropic gaps in a multiband scenario also experience more significant T_c suppression compared to the isotropic ones (see Fig. 1.12).

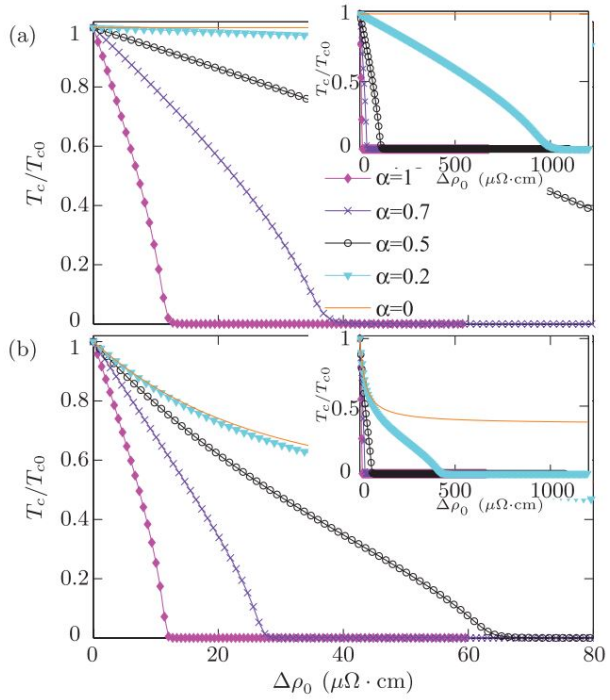

Figure 1.12 (a) Normalized critical temperature T_c/T_{c0} vs disorder-induced resistivity change $\Delta\rho_0$ for isotropic $s_\pm$-wave pairing for various values of the inter- to intraband scattering ratio $\alpha \equiv u/v$. Inset: Same quantity plotted over a larger $\Delta\rho_0$ scale. (b) As (a) but for an anisotropic (nodal) gap. From Ref. [58].

Li *et al.* [49] have summarized various Zn chemical doping and particle irradiation studies in iron-based superconductors with comparison to the aforementioned theoretical models. They found that in most cases the experimental data are not consistent with s_{++} since the T_c's are suppressed rather rapidly with increasing disorder introduced by Zn impurity concentration or irradiation dose. However, the suppression slopes are a factor of $\sim$5 larger (i.e., the T_c suppression is slower) than the $s_\pm$ slope value predicted by Onari, at best. They suggested that the mismatch could

have arisen from the combination of the theoretical side overestimating the role of the interband scattering, along with the experimental side's sample quality that could be improved. Overall, Li *et al*. concluded that the current state of affairs provide more justification toward $s_{\pm}$ side compared to s_{++} but further theoretical and experimental investigations are required.

1.3.3 Effects of non-magnetic disorder on the energy gap structure

Increasing the impurity concentration does not only affect T_c but also the the gap structure $\Delta(\mathbf{k})$ itself. This is because impurity states smear out the energy gap in the density of states (see Fig. 1.13(a)) and also mix different parts of the Fermi surface due to both interband and intraband interactions [27, 56]. With increasing disorder the gap function $\Delta(\mathbf{k})$ on the different FSs tend towards the same value. When this averaging mechanism happens between two isotropic bands but with opposite signs and different magnitudes, it may cause the smaller gap to switch sign leading to a transition from $s_{\pm}$ to s_{++} gap structure [57]. For a multiband case with anisotropy, disorder will average out the angular dependence and in some cases lift accidental nodes that are present in the pristine state [59] (e.g. in P-Ba122 [16], see Fig. 1.13(b)).

Therefore when considering all the possible effects on T_c and $\Delta(\mathbf{k})$ upon increasing disorder, we need to use a combination of experimental measurements that can together probe the gap structure (such as London penetration depth) as well as T_c and increase in residual resistivity ρ_0. When the measurements are done systematically and in tandem with electron irradiation, this combination has the potential to elucidate very valuable insight about the nature of superconductivity in the material. In our group we have the capability to perform these experiments. Whenever possible we also take a further step to synchronize our experiments; by selecting the samples for the resistivity and penetration depth measurements cleaved from one larger original crystal. Even though the growth batches that we usually work with are not particularly inhomogeneous, this extra step ensures that we are performing consistent and systematic study when we analyze the results across different experimental measurements. At other times when the samples in a given batch are too small to be cleaved in two, multiple crystals are measured to verify the consistency within the batch

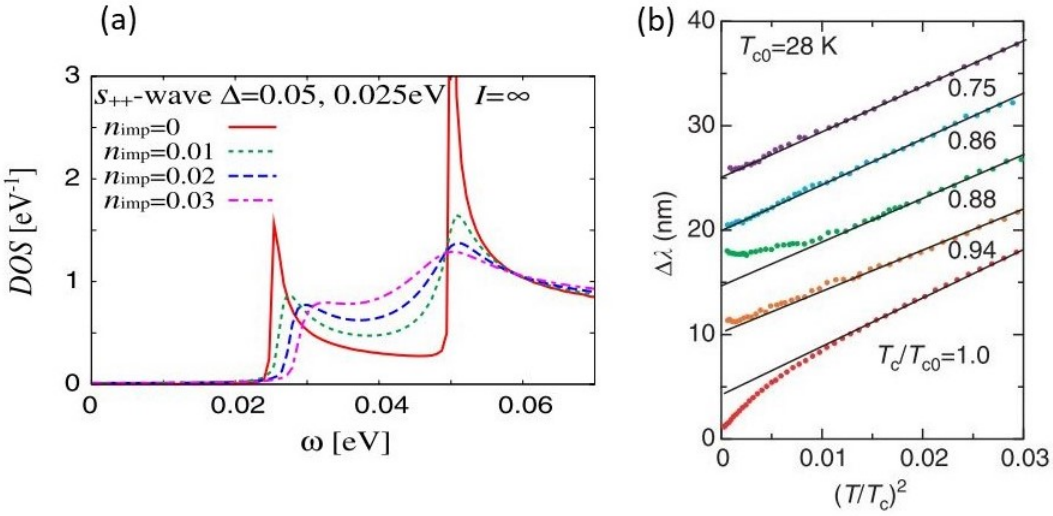

Figure 1.13 (a) Smearing of the density of states of the superconducting gap for an s_{++} state due to impurities. (b) Change in the magnetic penetration depth $\Delta\lambda$ plotted against $(T/T_c)^2$ for a $BaFe_2(As_{1-x}P_x)_2$ with $T_{c0} = 28$ K. Close to linear T-dependence in the pristine state (red) evolves into more exponential dependence (green) until saturating at the dirty limit quadratic dependence (purple). (a) From Ref. [56] and (b) from Ref. [16].

and to improve the statistical confidence. After the samples are measured in the pristine condition they are sent to irradiation (with the resistivity samples having their contacts preserved). After irradiation the samples are measured again in the resistivity and penetration depth setup then the data are compared to the pristine state. Because the contacts are preserved, the usual experimental uncertainty due to the resoldering of the contacts can be neglected and any changes in the data before and after irradiation are due solely to the sample's response. In Ch. 3 and thereafter, I will present and analyze the data from different superconductors measured using this protocol.

1.4 References

[1] Yoichi Kamihara, Hidenori Hiramatsu, Masahiro Hirano, Ryuto Kawamura, Hiroshi Yanagi, Toshio Kamiya, and Hideo Hosono. Iron-based layered superconductor: LaOFeP. *Journal of the American Chemical Society*, 128(31):10012–10013, 2006.

[2] W.E. Pickett. The other high-temperature superconductors. *Physica B: Condensed Matter*, 296(1):112 – 119, 2001. Proceedings of the Symposium on Wave Propagation and Electronic Structure in Disordered Systems.

[3] Yoichi Kamihara, Takumi Watanabe, Masahiro Hirano, and Hideo Hosono. Iron-based layered superconductor La[O1-xFx]FeAs (x= 0.05-0.12) with Tc = 26 K. *Journal of the American Chemical Society*, 130(11):3296–3297, 2008.

[4] L. Boeri, O. V. Dolgov, and A. A. Golubov. Is lafeaso$_{1-x}$f$_x$ an electron-phonon superconductor? *Phys. Rev. Lett.*, 101:026403, Jul 2008.

[5] Jian-Feng Ge, Zhi-Long Liu, Canhua Liu, Chun-Lei Gao, Dong Qian, Qi-Kun Xue, Ying Liu, and Jin-Feng Jia. Superconductivity above 100 K in single-layer FeSe films on doped SrTiO 3. *Nature Materials*, 14(3):285–289, mar 2015.

[6] Johnpierre Paglione and Richard L. Greene. High-temperature superconductivity in iron-based materials. *Nature Physics*, 6:645 EP –, Aug 2010. Review Article.

[7] Akira Iyo, Kenji Kawashima, Tatsuya Kinjo, Taichiro Nishio, Shigeyuki Ishida, Hiroshi Fujihisa, Yoshito Gotoh, Kunihiro Kihou, Hiroshi Eisaki, and Yoshiyuki Yoshida. New-structure-type fe-based superconductors: Caafe4as4 (a = k, rb, cs) and srafe4as4 (a = rb, cs). *Journal of the American Chemical Society*, 138(10):3410–3415, 2016. PMID: 26943024.

[8] Yoshikazu Mizuguchi, Keita Deguchi, Yasuna Kawasaki, Toshinori Ozaki, Masanori Nagao, Shunsuke Tsuda, Takahide Yamaguchi, and Yoshihiko Takano. Superconductivity in oxygen-annealed single crystal. *Citation: Journal of Applied Physics*, 109:13914, 2011.

[9] Dinah R Parker, Matthew J P Smith, Tom Lancaster, Andrew J Steele, Isabel Franke, Peter J Baker, Francis L Pratt, Michael J Pitcher, Stephen J Blundell, and Simon J Clarke. Control of the Competition between a Magnetic Phase and a Superconducting Phase in Cobalt-Doped and Nickel-Doped NaFeAs Using Electron Count. 2009.

[10] H. Luetkens, H.-H. Klauss, M. Kraken, F. J. Litterst, T. Dellmann, R. Klingeler, C. Hess, R. Khasanov, A. Amato, C. Baines, M. Kosmala, O. J. Schumann, M. Braden, J. Hamann-Borrero, N. Leps, A. Kondrat, G. Behr, J. Werner, and B. Büchner. The electronic phase diagram of the LaO1xF x FeAs superconductor. *Nature Materials*, 8(4):305–309, apr 2009.

[11] K. Kothapalli, A. E. Böhmer, W. T. Jayasekara, B. G. Ueland, P. Das, A. Sapkota, V. Taufour, Y. Xiao, E. Alp, S. L. Bud'ko, P. C. Canfield, A. Kreyssig, and A. I. Goldman. Strong cooperative coupling of pressure-induced magnetic order and nematicity in FeSe. *Nature Communications*, 7:12728, sep 2016.

[12] Yuta Mizukami, Marcin Konczykowski, Kohei Matsuura, Tatsuya Watashige, Shigeru Kasahara, Yuji Matsuda, and Takasada Shibauchi. Impact of disorder on the superconducting phase diagram in bafe2(as1xpx)2. *Journal of the Physical Society of Japan*, 86(8):083706, 2017.

[13] Sultan Demirdi, Thierry Klein, Président Cyril, Proust Raporteur, Christoph Meingast, Raporteur Véronique, Brouet Examinateur, Dimitri Roditchev Examinateur, Luca Perfetti, Examinateur Cornelis, Jacominus Van Der, and Beek Directeur. *Effects of Disorder in Iron-Based Superconductors*. PhD thesis, 2012.

[14] M. A. Tanatar, J. Ph Reid, H. Shakeripour, X. G. Luo, N. Doiron-Leyraud, N. Ni, S. L. Bud'Ko, P. C. Canfield, R. Prozorov, and Louis Taillefer. Doping dependence of heat transport in the iron-arsenide superconductor Ba(Fe1-xCox)2As2: From isotropic to a strongly K-dependent gap structure. *Physical Review Letters*, 104(6):067002, feb 2010.

[15] J.-Ph. Reid, M. A. Tanatar, X. G. Luo, H. Shakeripour, N. Doiron-Leyraud, N. Ni, S. L. Bud'ko, P. C. Canfield, R. Prozorov, and Louis Taillefer. Nodes in the gap structure of the iron arsenide superconductor $Ba(Fe_{1-x}Co_x)_2as_2$ from *c*-axis heat transport measurements. *Phys. Rev. B*, 82:064501, Aug 2010.

[16] Y. Mizukami, M. Konczykowski, Y. Kawamoto, S. Kurata, S. Kasahara, K. Hashimoto, V. Mishra, A. Kreisel, Y. Wang, P. J. Hirschfeld, Y. Matsuda, and T. Shibauchi. Disorder-induced topological change of the superconducting gap structure in iron pnictides. *Nature Communications*, 5:5657, nov 2014.

[17] K. Cho, M. Konczykowski, S. Teknowijoyo, M. A. Tanatar, Y. Liu, T. A. Lograsso, W. E. Straszheim, V. Mishra, S. Maiti, P. J. Hirschfeld, and R. Prozorov. Energy gap evolution across the superconductivity dome in single crystals of (Ba1-xKx)Fe2As2. *Science Advances*, 2(9):e1600807–e1600807, 2016.

[18] J.-Ph. Reid, M. A. Tanatar, A. Juneau-Fecteau, R. T. Gordon, S. René de Cotret, N. Doiron-Leyraud, T. Saito, H. Fukazawa, Y. Kohori, K. Kihou, C. H. Lee, A. Iyo, H. Eisaki, R. Prozorov, and Louis Taillefer. Universal heat conduction in the iron arsenide superconductor kfe_2as_2: Evidence of a *d*-wave state. *Phys. Rev. Lett.*, 109:087001, Aug 2012.

[19] H. Kim, M. A. Tanatar, W. E. Straszheim, K. Cho, J. Murphy, N. Spyrison, J.-Ph. Reid, Bing Shen, Hai-Hu Wen, R. M. Fernandes, and R. Prozorov. Competition between superconductivity and magnetic/nematic order as a source of anisotropic superconducting gap in underdoped $ba_{1-x}k_xfe_2as_2$. *Phys. Rev. B*, 90:014517, Jul 2014.

[20] P. J. Hirschfeld. Erratum: Corrigendum to Using gap symmetry and structure to reveal the pairing mechanism in Fe-based superconductors (Comptes Rendus Physique (2016) 17(1-2) (197231)(S1631070515001693)(10.1016/j.crhy.2015.10.002)). *Comptes Rendus Physique*, 17(7):803, 2016.

[21] Andrey Chubukov and Peter J. Hirschfeld. Iron-based superconductors, seven years later. *Physics Today*, 68(6):46–52, jun 2015.

[22] H. Ding, P. Richard, K. Nakayama, K. Sugawara, T. Arakane, Y. Sekiba, A. Takayama, S. Souma, T. Sato, T. Takahashi, Z. Wang, X. Dai, Z. Fang, G. F. Chen, J. L. Luo, and N. L.

Wang. Observation of fermi-surfacedependent nodeless superconducting gaps in ba 0.6 k 0.4 fe 2 as 2. *EPL (Europhysics Letters)*, 83(4):47001, 2008.

[23] Andrey Chubukov. Pairing Mechanism in Fe-Based Superconductors. *Annu. Rev. Condens. Matter Phys*, 3:57–92, 2012.

[24] A. D. Christianson, E. A. Goremychkin, R. Osborn, S. Rosenkranz, M. D. Lumsden, C. D. Malliakas, I. S. Todorov, H. Claus, D. Y. Chung, M. G. Kanatzidis, R. I. Bewley, and T. Guidi. Unconventional superconductivity in Ba0.6K0.4Fe2As2 from inelastic neutron scattering. *Nature*, 456(7224):930–932, dec 2008.

[25] Peter Babkevich, M Bendele, Andrew Boothroyd, Kazimierz Conder, S N Gvasaliya, R Khasanov, Ekaterina Pomjakushina, and B Roessli. Magnetic excitations of fe1 + ysexte1 - x in magnetic and superconductive phases. 22:142202, 04 2010.

[26] P J Hirschfeld, M M Korshunov, and I I Mazin. Gap symmetry and structure of Fe-based superconductors. *Reports on Progress in Physics*, 74(12):124508–44, 2011.

[27] I.I. Mazin and J. Schmalian. Pairing symmetry and pairing state in ferropnictides: Theoretical overview. *Physica C: Superconductivity*, 469(9-12):614–627, may 2009.

[28] Rafael M. Fernandes and Andrey V. Chubukov. Low-energy microscopic models for iron-based superconductors: A review. *Reports on Progress in Physics*, 80(1), 2017.

[29] A. V. Chubukov and I. Eremin. Angle-resolved specific heat in iron-based superconductors: The case for a nodeless extended s-wave gap. *Phys. Rev. B*, 82:060504, Aug 2010.

[30] Saurabh Maiti and Andrey V. Chubukov. Renormalization group flow, competing phases, and the structure of superconducting gap in multiband models of iron-based superconductors. *Phys. Rev. B*, 82:214515, Dec 2010.

[31] F. London and H. London. The electromagnetic equations of the supraconductor. *Proceedings of the Royal Society of London A: Mathematical, Physical and Engineering Sciences*, 149(866):71–88, 1935.

[32] R. Prozorov, R. W. Giannetta, A. Carrington, P. Fournier, R. L. Greene, P. Guptasarma, D. G. Hinks, and A. R. Banks. Measurements of the absolute value of the penetration depth in high-tc superconductors using a low-tc superconductive coating. *Applied Physics Letters*, 77(25):4202–4204, 12 2000.

[33] R Prozorov and V G Kogan. London penetration depth in iron-based superconductors. *Reports on Progress in Physics*, 74(12):124505, 2011.

[34] R. T. Gordon, H. Kim, N. Salovich, R. W. Giannetta, R. M. Fernandes, V. G. Kogan, T. Prozorov, S. L. Bud'ko, P. C. Canfield, M. A. Tanatar, and R. Prozorov. Doping evolution of

the absolute value of the london penetration depth and superfluid density in single crystals of $Ba(Fe_{1-x}Co_x)_2as_2$. *Phys. Rev. B*, 82:054507, Aug 2010.

[35] Bernhard Mühlschlegel. Die thermodynamischen funktionen des supraleiters. *Zeitschrift für Physik*, 155(3):313–327, Jun 1959.

[36] James Annett, Nigel Goldenfeld, and S. R. Renn. Interpretation of the temperature dependence of the electromagnetic penetration depth in $yba_2cu_3o_{7-\delta}$. *Phys. Rev. B*, 43:2778–2782, Feb 1991.

[37] D. Xu, S. K. Yip, and J. A. Sauls. Nonlinear meissner effect in unconventional superconductors. *Phys. Rev. B*, 51:16233–16253, Jun 1995.

[38] P. Townsend and J. Sutton. Investigation by electron tunneling of the superconducting energy gaps in nb, ta, sn, and pb. *Phys. Rev.*, 128:591–595, Oct 1962.

[39] R. T. Gordon. Ph. D. thesis, Iowa State University, 2011.

[40] Ruslan Prozorov and Russell W. Giannetta. Magnetic penetration depth in unconventional superconductors. *Superconductor Science and Technology*, 19(8), 2006.

[41] F. Gross, B. S. Chandrasekhar, D. Einzel, K. Andres, P. J. Hirschfeld, H. R. Ott, J. Beuers, Z. Fisk, and J. L. Smith. Anomalous temperature dependence of the magnetic field penetration depth in superconducting ube13. *Zeitschrift für Physik B Condensed Matter*, 64(2):175–188, Jun 1986.

[42] Peter J. Hirschfeld and Nigel Goldenfeld. Effect of strong scattering on the low-temperature penetration depth of a d-wave superconductor. *Phys. Rev. B*, 48:4219–4222, Aug 1993.

[43] D. Parker, O. V. Dolgov, M. M. Korshunov, A. A. Golubov, and I. I. Mazin. Extended $s_\pm$ scenario for the nuclear spin-lattice relaxation rate in superconducting pnictides. *Phys. Rev. B*, 78:134524, Oct 2008.

[44] A.C. Damask and G.J. Dienes. *Point Defects in Metals*. Gordon and Breach Science, 1963.

[45] The scattering of fast electrons by atomic nuclei. *Proceedings of the Royal Society of London A: Mathematical, Physical and Engineering Sciences*, 124(794):425–442, 1929.

[46] M. W. Thompson. *Defects and Radiation Damage in Metals*. September 1974.

[47] P.W. Anderson. Theory of dirty superconductors. *Journal of Physics and Chemistry of Solids*, 11(1):26 – 30, 1959.

[48] AA Abrikosov and LP Gorkov. Zh. é ksp. teor. fiz. 39, 1781 1960 sov. phys. *JETP*, 12:1243, 1961.

[49] Jun Li, Yan-Feng Guo, Zhao-Rong Yang, Kazunari Yamaura, Eiji Takayama-Muromachi, Hua-Bing Wang, and Pei-Heng Wu. Progress in nonmagnetic impurity doping studies on Fe-based superconductors. *Superconductor Science and Technology*, 29(5):053001, may 2016.

[50] A. V. Balatsky, I. Vekhter, and Jian-Xin Zhu. Impurity-induced states in conventional and unconventional superconductors. *Rev. Mod. Phys.*, 78:373–433, May 2006.

[51] K. V. Samokhin. *Effects of Impurities in Non-centrosymmetric Superconductors*, pages 269–295. Springer Berlin Heidelberg, Berlin, Heidelberg, 2012.

[52] Zhao Lin, Liu Hai-Yun, Zhang Wen-Tao, Meng Jian-Qiao, Jia Xiao-Wen, Liu Guo-Dong, Dong Xiao-Li, Chen Gen-Fu, Luo Jian-Lin, Wang Nan-Lin, Lu Wei, Wang Gui-Ling, Zhou Yong, Zhu Yong, Wang Xiao-Yang, Xu Zu-Yan, Chen Chuang-Tian, and Zhou Xing-Jiang. Multiple nodeless superconducting gaps in (ba 0.6 k 0.4)fe 2 as 2 superconductor from angle-resolved photoemission spectroscopy. *Chinese Physics Letters*, 25(12):4402, 2008.

[53] K. Nakayama, T. Sato, P. Richard, Y.-M. Xu, Y. Sekiba, S. Souma, G. F. Chen, J. L. Luo, N. L. Wang, H. Ding, and T. Takahashi. Superconducting gap symmetry of ba 0.6 k 0.4 fe 2 as 2 studied by angle-resolved photoemission spectroscopy. *EPL (Europhysics Letters)*, 85(6):67002, 2009.

[54] J. S. Dugdale and Z. S. Basinski. Mathiessen's rule and anisotropic relaxation times. *Phys. Rev.*, 157:552–560, May 1967.

[55] S. Teknowijoyo, K. Cho, M. Kończykowski, E. I. Timmons, M. A. Tanatar, W. R. Meier, M. Xu, S. L. Bud'ko, P. C. Canfield, and R. Prozorov. Robust $s_{\pm}$ pairing in $\mathrm{CaK(Fe_{1-x}Ni_x)_4as_4}$ ($x = 0$ and 0.05) from the response to electron irradiation. *Phys. Rev. B*, 97:140508, Apr 2018.

[56] Seiichiro Onari and Hiroshi Kontani. Violation of Anderson's Theorem for the Sign-Reversing s-Wave State of Iron-Pnictide Superconductors.

[57] D. V. Efremov, M. M. Korshunov, O. V. Dolgov, A. A. Golubov, and P. J. Hirschfeld. Disorder-induced transition between $s_{\pm}$ and s_{++} states in two-band superconductors. *Phys. Rev. B*, 84:180512, Nov 2011.

[58] Y Wang, A Kreisel, P J Hirschfeld, and V Mishra. Using controlled disorder to distinguish s and s ++ gap structure in Fe-based superconductors. *PHYSICAL REVIEW B*, 87:94504, 2013.

[59] V. Mishra, G. R. Boyd, S. Graser, T. Maier, P. J. Hirschfeld, and D. J. Scalapino. Lifting of nodes by disorder in extended-s-state superconductors: Application to ferropnictides. *Phys. Rev. B*, 79:094512, Mar 2009.

CHAPTER 2. EXPERIMENTAL DETERMINATION OF THE SUPERCONDUCTING GAP STRUCTURE: LONDON PENETRATION DEPTH AND DISORDER

In Chapter 1, we learned that a superconductor's energy gap structure can give crucial clues toward understanding the microscopic theory behind the pairing mechanism. Here we will discuss in more detail the theory behind London penetration depth, what it tells us about the gap structure and how to measure it experimentally in the laboratory.

2.1 London Penetration Depth

When subjected into a weak magnetic field, a material in the superconducting state ($T < T_c$) will form a supercurrent close to the surface to expel the magnetic induction from its interior ($B_{inside} = 0$), the phenomenon of which is called the Meissner - Ochsenfeld effect [1] (see Fig. 2.1). The characteristic length scale where the magnetic induction dies out exponentially inside the superconductor is called the London penetration depth, λ_L, due to the work of the London brothers in 1935 [2].

$$\nabla^2 B = \frac{B}{\lambda_L^2} \tag{2.1}$$

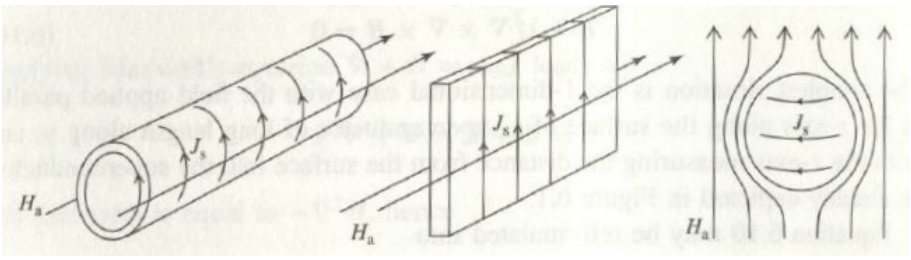

Figure 2.1 Some examples of sample shapes and screening currents in an external magnetic field. From Ref. [3].

Together with the coherence length ξ, which characterizes the spatial variation of the order parameter, these two characteristic lengths are very important parameters which factor into many properties of a superconducting material, such as the upper critical fields, the physics of vortices, etc. In particular, the ratio of London penetration depth (from now on I just denote it by λ for simplicity) to the coherence length defines the Ginzburg-Landau parameter $\kappa = \lambda/\xi$, which is the most common criterion used to distinguish between type-I ($\kappa < 0.7$) and type-II ($\kappa > 0.7$) superconductors. Here, we will focus on the temperature dependence of the change in London penetration depth, $\Delta\lambda(T)$, which can be measured very accurately using the tunnel-diode resonator method (more in Section 2.2), and provide useful insights of the energy gap structure of a superconductor.

For an isotropic material (electron gas model) with no demagnetization effect (infinite slab approximation), the London penetration depth is related to the paired electrons responsible for the supercurrent by

$$\lambda^2(T) = \frac{mc^2}{4\pi e^2 n_s(T)} \tag{2.2}$$

with m is the mass of a Cooper pair and n_s is the density of the superconducting electron which also gives the T-dependence. In a typical metal, the supercurrent involves about 1% of the total electron density (the total includes the core electrons) at temperatures well below T_c, when all the usable electrons near the Fermi surface form pairs. These are the electrons (denoted as n) that lie close to the FS, which are also responsible for the normal conduction and thermodynamics processes above T_c. When temperature is lowered to $0 < T < T_c$, a fraction of n condenses into forming Cooper pairs, n_s, until this fraction reaches unity at $T = 0$. We denote the remaining electrons that stay normal below T_c as n_n ($n = n_n + n_s$) which will disappear completely at $T = 0$. This phenomenological two-fluid coexistence model was introduced by Gorter and Casimir in 1934 [4] with the proposed empirical T-dependence $n_s = n(1 - (\frac{T}{T_c})^4)$.

To account for the anisotropy in real materials we have to consider a more sophisticated model. For the anisotropic treatment, I will follow the semiclassical approach provided by Prozorov *et al.* [5] and Chandrasekhar *et al.* [6], which gives a general method to calculate three spatial components of the London penetration depth of a given Fermi surface and a gap function (the superconducting

order parameter). This treatment is very useful for properly interpreting and understanding the experimental results, since oftentimes measurements are only taken in specific orientations. For example, when the sample is in thin rectangular shape along the ab plane and placed perpendicular to the magnetic field, we would only get information about λ_{ab} but not λ_c. So for a superconductor with an arbitrary electronic structure,

$$\lambda_{ii}^2 = \frac{c}{4\pi\mathbb{R}_{ij}}, i, j = x, y, z \tag{2.3}$$

$\mathbb{R}_{ij} = \mathbb{R}_D + \mathbb{R}_P$ is the (symmetric) response tensor proportional to the superfluid density n_s which contains diamagnetic and paramagnetic contributions. $\mathbb{R}_{ij}$ also contains the information about the anisotropy of the Fermi surface and the gap function $\Delta(\mathbf{k})$. The full expression is given by

$$\mathbb{R}_{ij} = \frac{e^2}{4\pi^3\hbar c}\oint_{FS} dS_k \left[\frac{v_F^i v_F^j}{|\mathbf{v}_F|}\left(1 + 2\int_{\Delta(k)}^{\infty}\frac{\partial f(E)}{\partial E}\frac{E}{\sqrt{E^2 - \Delta(\mathbf{k})^2}}dE\right)\right] \tag{2.4}$$

$f(E)$ is the Fermi function, $\mathrm{E} = \sqrt{\varepsilon^2 + \Delta(\mathbf{k})}$ is the quasiparticle energy, with the normal metal band energy ε is measured from E_F. v_F^i are the components of the Fermi velocity, $\mathbf{v}_F$. The second term is the paramagnetic contribution which contains an integral that averages the gap function $\Delta(\mathbf{k}, T)$ over the Fermi surface. So, from Eq. 2.4, we are able to relate experimentally measured penetration depth to the gap structure of the sample of interest. The determination of the structure and symmetry of a superconducting gap puts restriction on the pairing mechanism candidates available for the theory. Ultimately, this will let us come to the proper model of superconductivity in iron-based superconductor, and possibly in other families of unconventional superconductors.

Another useful quantity for understanding the gap structure a superconductor is the superfluid density, which is the fraction of conduction electrons that condense into pairs as function of temperature, given by

$$n_{ii}(T) = \frac{cm_{ii}}{e^2}\mathbb{R}_{ii}(T) \tag{2.5}$$

$$m_{ii} = \frac{e^2 n}{c\mathbb{R}_{ii}(0)} \tag{2.6}$$

with m_{ii} is the effective mass. As mentioned above, Gorter and Casimir proposed $(T/T_c)^4$ dependence that describes conventional (BCS) superconductors, which were the only ones known at that

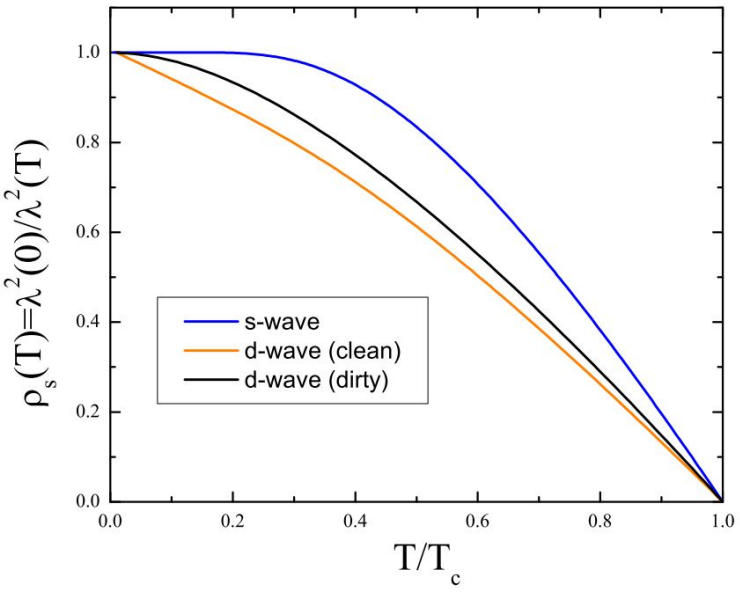

Figure 2.2 Theoretical curves for normalized superfluid density vs. normalized temperature for clean s-wave, clean d-wave and dirty d-wave cases. From ref. [7].

time. As of now, many different kinds of superconductors have been discovered with each having a distinct temperature dependence of the normalized superfluid density profile

$$\rho_{ii}(T) = \frac{n_{ii}(T)}{n} = \frac{\mathbb{R}_{ii}(0)}{\mathbb{R}_{ii}(T)} = \left(\frac{\lambda_{ii}(0)}{\lambda_{ii}(T)}\right)^2 \tag{2.7}$$

Comparing the experimentally obtained profiles to the standard s-wave BCS or d-wave cuprates profiles shown in Fig. 2.2 sometimes gives enough evidence to ascertain the gap structure of the material of interest. Next we will discuss how to experimentally use the tunnel-diode resonator method to measure London penetration depth, which then can be transformed into the superfluid density of a superconductor.

2.2 Measurement of London Penetration Depth: Tunnel-diode Resonator Method

Here we discuss the technique that was used in this work to measure London penetration depth in a material. The method was developed in the University of Illinois Urbana-Champaign, by Carrington and Prozorov *et al.* [8, 9, 10, 11], using a device called tunnel-diode, whose low temperature properties and stability were extensively explored by Van Degrift [12]. First, we will discuss the basic properties of a tunnel-diode circuit, the backbone of our tunnel-diode resonator (TDR) method, and then how to use it to measure London penetration depth in the laboratory.

2.2.1 Basic properties of a tunnel-diode circuit

A tunnel-diode or Esaki diode is a heavily doped P-N junction semiconductors, which causes an overlap between the p-type filled valence band and the n-type empty conduction band. With very thin depletion layer of ~ 100 Å, electrons can tunnel through the junction even in zero bias condition. This causes tunnel-diodes to have a distinct I-V diagram compared to the normal diode (see Fig. 2.3).

As can be seen in Fig. 2.3, there exists a negative slope for some range of forward bias values. In this range, the (differential) resistance is *negative*. This feature is unique to the tunnel-diode, which allows it to act as a power supply when connected to a tank circuit. The LC circuit is driven to resonance at its own natural frequency, $f_0 = \frac{1}{2\pi\sqrt{LC}}$ and the losses are compensated by the TD. This method does away with an external AC generator which normally is used to drive the tank circuit, and thus minimizes the noise and the uncertainties coming from outside the tank system. The resonant state which is locked by the tunnel-diode is highly stable, even when f_0 is slowly changing due to changes of the inductance and/or capacitance. This provides a way to measure the magnetic penetration depth of a superconductor specimen of interest, which can be placed inside the inductor (coil) or the capacitor (parallel plates). For the inductor (capacitor) configuration, as the specimen transitions from superconducting to normal phase or vise versa, the inductance

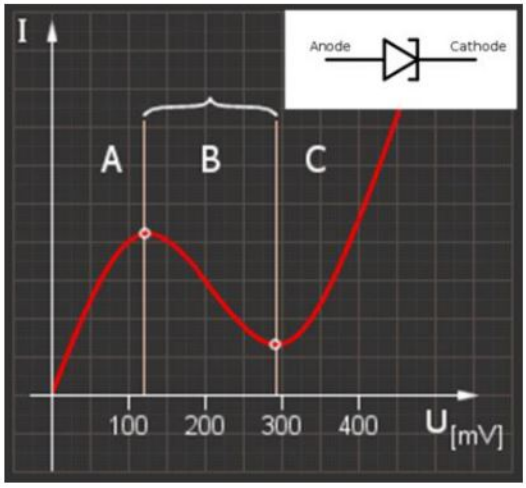

Figure 2.3 The I-V characteristic curve of a tunnel-diode. **B** denotes the region of negative differential resistance which is reachable by properly biasing the tunnel-diode. While the tunnel-diode is operating within **B**, it can be used as a driving source for the tank circuit. From Ref. [13].

(capacitance) will change, which can be tracked from the change of the natural frequency. This is the basic principle behind the TDR method for London penetration depth measurement.

In our laboratory, we use the sample-in-coil configuration. The sample is mounted on a ∼1 mm diameter sapphire rod which is part of the sample holder contraption (see diagram in Fig. 2.4), which is inserted into a ∼2.0 mm inner diameter coil. The coil's length is ∼1 cm, has ∼60 spaced turns, and generates ∼20 mOe field.

The sample holder (Fig. 2.4) is designed so that the sample stage can be heated independently without significantly warming up the rest of the cryostat, using a ceramic (macor) material as the main thermal break. This isolation is critical in order to efficiently use the available volume of condensed ^{3}He liquid in the the ^{3}He pot, which is the main source of cooling power below 4 K. A good thermal break therefore saves time, liquid ^{4}He and other lab operation resources. The outside shell of the sample holder is removable, which allows any necessary inspections and repairs of the soldered joints to the thermometer and heater to be done easily when needed. For more details about the sample holder dimensions and drawings, see Appendix.

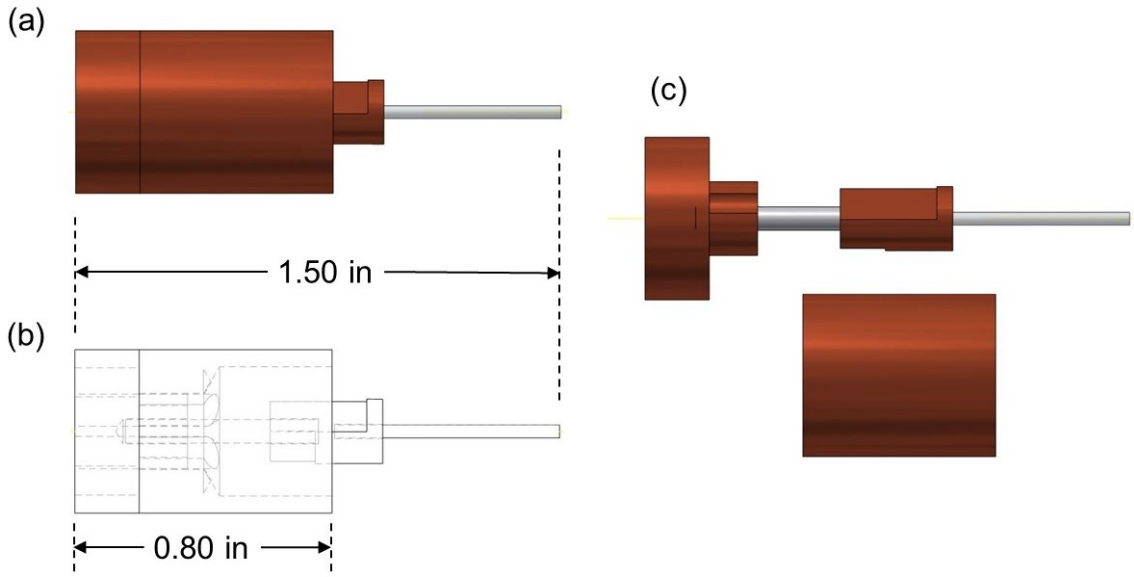

Figure 2.4 Autodesk inventor schematics of the ^{3}He perpendicular sample holder. (a) Side view and (b) side view with visible edges. (c) Side view with the outer shell removed. From left to right: the base, the macor rod, the thermometer/heater stage and the sapphire rod where the sample is mounted. The outer diameter of the shell is 0.506 in, the length of the base and the shell is 0.80 in and the total length from the base to the sapphire tip is ∼1.50 in.

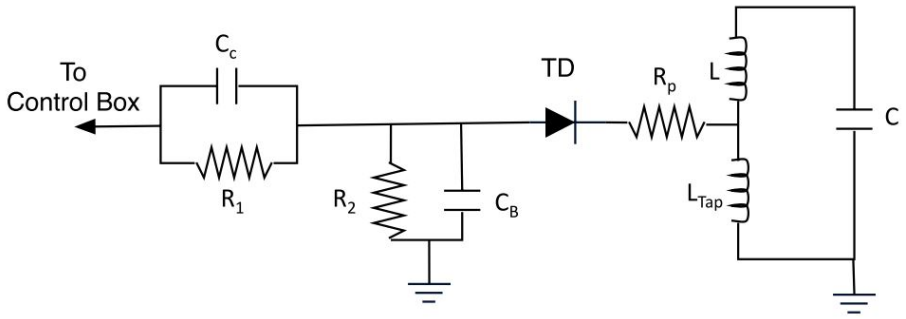

Figure 2.5 A typical TDR circuit diagram. See text for descriptions of the components. From Ref. [14].

Table 2.1 Different examples for the values of the TDR circuit component set.

System	$\mathbf{R}_1$	$\mathbf{R}_2$	$\mathbf{R}_P$	$\mathbf{C}_C$	$\mathbf{C}_B$	$\mathbf{C}_{Tank}$	**TD**
Dipper (2014/07/02)	1 kΩ	200 Ω	100 Ω	39 pF	15 nF	100 pF	$I_p = 223$ μA
^{3}He (2015/06/09)	1.5 kΩ	300 Ω	300 Ω	47 pF	12 nF	120 pF	$I_p = 120$ μA
^{3}He (2007/11/08)	1.2 kΩ	270 Ω	300 Ω	5.6 pF	10 nF	120 pF	(Ruslan's record)

For an optimal and stable low temperature measurement, the tunnel-diode + LC combination has to be protected from external noise and heat sources, such as the room temperature electronics and ground. We use a combination of resistors and capacitors for the electrical signal protection, and high resistance wires for the thermal insulation. The typical full TDR circuit and their component values are shown in Fig. 2.5 and Table 2.1.

In Fig. 2.5, starting from the left side, the line feeds into the bias box at room temperature via an SubMiniature version A (SMA) cable. This cable carries signals both ways: the DC signal to forward bias the tunnel-diode and the AC signal from the tank circuit which is the measurement data. The SMA is connected at the top of the cryostat, then the signal is further carried down by high resistance wire (Beryllium Copper or Phosphorus Bronze materials) to the circuit stage. Since the wire is also highly thermally resistant, the temperature gradient from the room temperature at the top to the low temperature (∼5 K) at the circuit stage can be maintained with high stability. R_1 and C_C filter some unwanted frequencies but still let the DC bias and AC data (typically ∼10

MHz) signals to pass through. Also, R_1 and R_2 together become a voltage divider so that the proper DC bias is achieved across the tunnel-diode. The bypass capacitor, C_{B}, is chosen to be large to act as a short for frequencies in the TDR range. The parasitic resistor, R_{P}, serves to kill stray oscillations that may occur between the small capacitance of the tunnel-diode itself and the tap coil. The tap coil is used to dampen away higher harmonics of the resonance frequency. It usually has $\sim$1/3 of the inductance of the primary coil. It is chosen such that the tap inductance is just beyond the critical value that will allow the tank circuit to resonate. When properly optimized, the TDR circuit will only resonate at low temperature (< 100 K) but not at room temperature. Finally, the total impedance of R_3, C, primary and tap L's should be low enough so that it can just be barely compensated by the negative differential resistance of the tunnel-diode. More detailed description of the TDR circuit can be found in these references [7, 12, 14, 15].

2.2.2 Calibration of penetration depth from TDR frequency measurement

In this section, we will cover the conversion of $\Delta f(T)$ from the TDR signal to $\Delta\lambda(T)$, which contains the information about the gap structure of the material. In the analysis, numerical solutions are taken because of the complication coming from the sample geometry, which is commonly shaped as a thin rectangular block. For λ_{ab} (when the sample is placed perpendicular to field, see Fig. 2.6b), the demagnetization and London equations cannot be solved analytically. Exact analytical solutions are only available for special geometries: an infinite bar or cylinder in longitudinal field, a cylinder in perpendicular field, a sphere or a thin film. We will present the numerical method described by Prozorov *et al.* in [5, 11] for two dimensional long slabs in a perpendicular field, with the results are then extended analytically to three dimensions.

We start by considering the natural resonance frequency of the tank circuit with an empty coil, $f_0 = \frac{1}{2\pi\sqrt{LC}}$. When a superconducting specimen is inserted into the coil, due to the field screening from its interior (diamagnetic/Meissner response) there will be a shift of inductance, ΔL, which in turn shifts the resonance frequency by Δf. Then we have

$$f_0 + \Delta f = \frac{1}{2\pi\sqrt{(L+\Delta L)C}} \tag{2.8}$$

Since L of the coil is in the order of $\sim$1 μH (coil dimensions d = 1.5 mm, l = 10 mm, 60 turns) and ΔL $\sim$10 nH (sample dimensions 1 x 1 x 0.1 mm^3), $\Delta L << L$. Then we can use a binomial expansion and factoring to get

$$\frac{\Delta f}{f_0} \approx -\frac{1}{2}\frac{\Delta L}{L} \tag{2.9}$$

Now let's work out another equation to replace the right hand side of Eq. 2.9 so we can relate Δf to the magnetic susceptibility, χ_{AC}, of the sample. We start from the relation

$$L = \frac{d\Phi}{dI} \tag{2.10}$$

when the coil is empty. Also, $\Phi = H_{AC}V_c$ is the integrated magnetic flux inside the coil, with H_{AC} being the AC field inside and V_c is the volume of the coil. Now we consider the case when a sample is inside the coil. Then we can write,

$$\Phi^* = H_{AC}(V_c - V_s) + BV_s = H_{AC}V_c + 4\pi V_s M \tag{2.11}$$

where we have used the linear relation $B = H + 4\pi M$ to get to the right hand side. The first term is just Φ of the empty state and the second term coming from the sample response. Notice that we can take derivative to get $L^* = L + \Delta L$, with $L = V_c\frac{dH}{dI}$ and $\Delta L = 4\pi V_s \frac{dM}{dH}\frac{dH}{dI}$. Setting $\frac{dM}{dH} = \chi_{AC}$, we can write

$$\frac{\Delta L}{L} = \frac{4\pi V_s}{V_c}\chi_{AC} \tag{2.12}$$

Substituting back to the Eq. 2.9, we can relate the shift in resonance frequency to the AC magnetic susceptibility of the sample

$$\frac{\Delta f}{f_0} = -\frac{V_s}{2V_c}4\pi\chi_{AC} \tag{2.13}$$

Yet this is still not the stage we want. The final step to relate the frequency shift to penetration depth is described in [11] for thin square prism geometry of width $2w$ and thickness $2d$. The configuration and result are given below

$$-4\pi\chi = \frac{1}{1-N}\left[1 - \frac{\lambda_{ab}}{R}\tanh\left(\frac{R}{\lambda_{ab}}\right)\right] \tag{2.14}$$

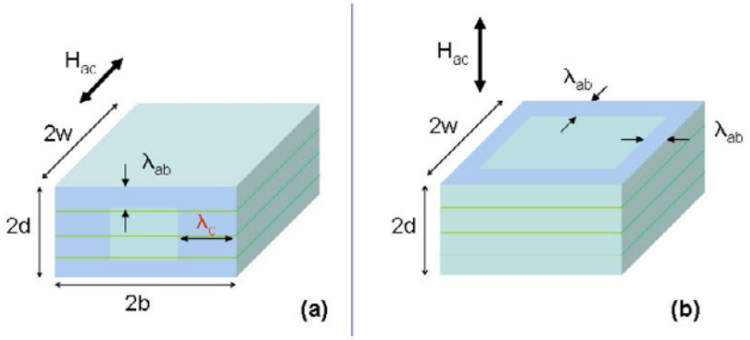

Figure 2.6 Different experimental configurations. In configuration (a), the field is along the plane and the measured signal is a combination of the contributions from both λ_{ab} and λ_c. In configuration (b), the field is perpendicular to the plane, and only λ_{ab} is measured. From Ref. [5].

Here χ is the magnetic susceptibility, N is the effective (numerical approximation of) demagnetization factor, R is the effective sample size for thin square prism geometry and λ_{ab} is the in-plane penetration depth (see Fig. 2.6(b)). Now, the numerical approximation for R from the sample dimensions is given by the expression

$$R \approx \frac{w}{2\left[1+\left[1+\left(\frac{2d}{w}\right)^2\right]\arctan\left(\frac{w}{2d}\right)-\frac{2d}{w}\right]} \tag{2.15}$$

Again, here we assume a square cross section with sides of length $2w$. In real life, most samples are not perfect squares. If instead, the sample is rectangular with a cross section $2a$ x $2b$, then we can still use 2.15 by approximating w by

$$w = \frac{2ab}{a+b} \tag{2.16}$$

Let's consider the typical sample dimensions, which are 0.5 x 0.5 x 0.05 mm^3. Using 2.15 we get $R \approx 112$ μm, which is much larger than a typical value of penetration depth in a superconductor (~ 1 μm). So using the limit $\lambda \ll R$ to expand the hyperbolic tangent function, and combining 2.13, 2.14 and 2.15, finally we are able to relate measured TDR frequency $\Delta f(T)$ into penetration

depth $\lambda(T)$, both of which have an explicit dependence on temperature

$$\frac{\Delta f(T)}{f_0} = \frac{V_s}{2V_c(1-N)}\left(1 - \frac{\lambda(T)}{R}\right) \tag{2.17}$$

If we move f_0 into the right hand side, we can define the apparatus and sample-dependent proportionality factor $\Delta f_0 = f_0 V_s/[2V_0(1-N)]$. During the experiment, this factor as a change in frequency is measured directly by pulling the sample out of the coil at the experimental base temperature.

While we already connected the TDR frequency shift Δf to the penetration depth $\lambda(T)$, let us take one step further and define $\Delta\lambda(T) = \lambda(T) - \lambda(0)$. This is reasonable because it is the *change* of penetration depth over temperature that contains the information about the gap structure. In subsequent chapters the penetration depth data are presented in this quantity. There is however, a small caveat: since the determination of $\lambda(0)$ often requires non-trivial measurements and not easily available with the TDR method, we define $\Delta(T)$ from our experimental base temperature ($\sim$ 400 mK). This allows us to set the penetration depth in a relative scale, which does not change the physics and is still perfectly usable. We can rearrange Eq. 2.17 and define $\delta f(T) \equiv \Delta f(T) - \Delta f(T_{min})$ to get

$$\Delta\lambda(T) = \lambda(T) - \lambda(T_{min}) = -\delta f(T)\frac{R}{\Delta f_0}. \tag{2.18}$$

How about λ_c? To measure λ_c, the sample needs to be inserted with the field parallel to the ab-plane (see Fig. 2.6(a)). In this case, Δf^{mix} contains contributions from both $\Delta\lambda_{ab}$ and $\Delta\lambda_c$, from the relation [16]

$$\frac{\Delta f^{mix}}{\Delta f_0^{mix}} \approx \frac{\Delta\lambda_{mix}}{R_b} = \frac{\Delta\lambda_{ab}}{t} + \frac{\Delta\lambda_c}{w} \tag{2.19}$$

with R_b (not to be confused by R) is the effective dimension in the $H||ab$ configuration for a rectangular sample of length l, width $2w$ and thickness $2t$. Due to the geometry, the contribution of $\Delta\lambda_{ab}$ is much larger than $\Delta\lambda_c$ so the extraction of $\Delta\lambda_c$ from Eq. 2.19 is prone to large errors. A more reliable method involves cutting the sample and measuring it again the second time. It goes as follows: first, the sample is measured with the field is oriented along the longest side ($H||l$). Then, the sample is cut along this l direction in two halves, so that the width (originally $2w$) is

reduced to w, and one of the halves is measured again (with the same orientation $H||l$). Since the thickness $2t$ remains the same, we can now use Eq. 2.19 from the two measurements to eliminate $\Delta\lambda_{ab}$ (two equations two unknonws). This protocol yields a more accurate temperature dependence of $\Delta\lambda_c(T)$ [16].

2.2.3 Screening of samples using the TDR dipper probe

In this section the method employed in our group to select high quality samples for the London penetration depth measurement is described. Our Janis ^{3}He cryostat which is our main TDR instrument requires three days and ∼40 liters of liquid helium (∼ $300, 2018 price) to measure a sample in a typical operation. Since money and time are limited resources, we need to be wise in selecting the candidates from a given batch of samples. To make sure that our resources are only spent on the best single crystals, we screen many samples taken from a same batch in our TDR dipper setup, which was developed in-house by the previous students, Nick Spyrison and Hyunsoo Kim [15, 17]. This probe is basically a simplified version of the TDR cryostat which is very useful for a "quick and dirty" London penetration depth measurement. It is meant to be inserted or "dipped" in a He transfer dewar (hence called the dipper) to quickly access the liquid helium temperature for the measurement. It is equipped with a complete TDR circuit with the sample inserted inside the coil, so the frequency change corresponds to the magnetic penetration depth inside the sample. The sample holder construction is based on the original ^{3}He setup which includes a main copper stage with a sapphire rod, a thermometer and heater attached. The practical base temperature is ∼4.5 K and one measurement can be done in an hour. There is no temperature control on the circuit stage, so the signal is often too noisy to extract a meaningful conclusion in the low temperature range. However, the probe provides good enough resolution to compare the superconducting transition between samples side by side to easily spot unwanted features, such as a second phase, an excessive broadness or a non-superconducting specimen (see Fig. 2.7(a)). The best sample is the one that (at the end of the screening process) has the sharpest transition (smallest $\Delta T_c \equiv T_c^{onset} - T_c^{offset}$) along with a large frequency shift (which is proportional to the crystal size). For example in Fig. 2.7,

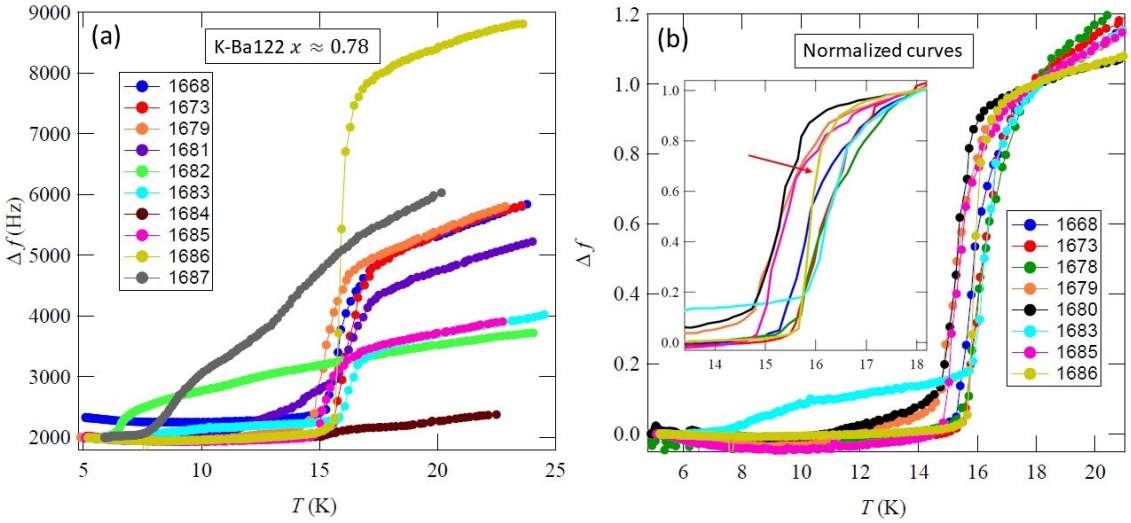

Figure 2.7 A summary of the screening process of K-Ba122 with $x \approx 0.78$ using the dipper probe. (a) Shows the raw data in frequency shift of 10 different samples. 1682, 1684 and 1687 are not superconducting, while 1681 shows a secondary transition, indicating its compositional inhomogeneity. The rest of the samples shows decent transition, however, 1686 stands out due to its transition's size and sharpness. (b) Several select samples normalized by the size of the transition. Inset: magnified view of the transition. Red arrow points to 1686 which clearly has a smooth and sharp transition worth measuring in the ^{3}He setup.

the sample with dipper number 1686 (yellow) has both the sharpest and largest transition. In this case, 1686 is the ideal candidate to be measured in the full ^{3}He TDR setup.

2.3 Electron Irradiation to Introduce Point-like Disorder

In Section 1.3, electron irradiation in the MeV range is singled out as the sole mechanism to reliably create artificial point-like disorder in a material. One of such facility is the SIRIUS facility of the Laboratoire des Solides Irradiés (LSI) at Ecole Polytechnique, Palaiseau, France. It is a user facility where research groups can apply for beam time several times a year. Our group is a frequent user of the facility and we have published various papers from our collaboration with the operators.

Figure 2.8 From https://portail.polytechnique.edu/lsi/en/facilities/sirius-installation.

Their Pelletron machine (Fig. 2.8) can deliver a beam of electrons with 2.5 MeV energy to a cryostat which is cooled with liquid hydrogen ($T \approx 20$ K). The irradiation on the sample is performed at low temperature to minimize *in situ* defect migration, recombination and clustering [18]. The cryostat is also equipped with *in situ* resistivity setup to track the increase in the sample's resistance as it is being irradiated at ∼20 K. But to get the temperature dependence of resistivity, the sample has to be taken out of the cryostat to be measured in a different system because the *in situ* setup does not have a built in temperature control. Upon raising the sample back to the room temperature after irradiation, up to 40% of defects are annealed as estimated from the drop of the residual resistivity ρ_0 value [19, 20]. After that initial annealing, to first approximation, the defects are metastable as long as the sample is not subjected to higher temperatures during the passive storage in the desiccator [19]. The remaining $\sim 60 - 70\%$ of the defects contribute as pair-breaker impurities which increase ρ_0 and suppress T_c in most SCs. Although the artificial defects are relatively stable, in our experience, some of our samples do recover a small fraction of the T_c suppression when they are remeasured several months after irradiation. However, since most of our samples are measured within 1 - 3 weeks of irradiation (we irradiate tens of samples in one period of irradiation), we can be quite certain that our irradiation data are reliable.

In Fig. 3.2, the sharpness of the superconducting transitions is preserved after irradiation, which suggests that the sample remains homogeneous and the defects are randomly distributed throughout the full volume. The lateral homogeneity of the electron distribution is guaranteed by the beam rastering over an inch-wide large area, so that, statistically, the entire surface of a

sub-mm sample is well covered. Our TDR sample holder has a diameter of 1 mm, so it is limited to square/rectangular samples with diagonal $\leq$ 1 mm, well below the size limit of the irradiation lateral uniformity. However, the longitudinal distribution of the created defects is a different issue, because there are examples of a significant depth dependence of measured properties in electron-irradiated superconductors [21]. A more quantitative analysis using available softwares, such as the National Institute of Standards and Technology's (NIST) ESTAR [22], can be employed. As an example, in Ch. 5 we calculated the stopping power for electrons in an FeSe sample. We found that the average energy loss by 2.5 MeV electrons throughout a 0.03 mm FeSe sample is only 26 keV, or $\sim$ 1 % of the initial energy. In general, since 2.5 MeV electrons have $\sim$mm penetration range [23, 24], we limit our samples' thickness to a maximum of $\sim$ 150 μm to ensure full and homogeneous defect creation.

The defects created by 2.5 MeV electron irradiation are assumed to be dominated by interstitial-vacancy (Frenkel) pairs. After irradiation, the interstitials are known to migrate to various "sinks" as the sample is warmed up to the room temperature, which causes the resistivity to drop by $\sim$30% [19, 20]. The remaining 70% of the defects can be largely attributed to the left vacancies, which are generally not as mobile compared to the interstitials. The concentration of the produced Frenkel pairs can be estimated using the SECTE simulation package [25] by calculating the cross-section of a specific ion as a function of the energy of the electron (see Ch. 5 for an example of such simulation). After irradiation, within the excellent sensitivity of our TDR technique we find that the defects are non-magnetic. Moreover, the measurements of Hall coefficient before and after the electron irradiation found no change in the electronic carrier density, which implies that the defects do not effectively dope the system, but only increase the scattering rate [19, 20, 26].

The dose of the irradiation is usually given in units of C/cm^2 for convenience, which can be converted to the number of electrons by a factor of electron charge $1/e$. This gives 1 C/cm^2 = 6.24 x 10^{18} electrons/cm^2. The actual dose experienced by the sample is calibrated in real time by measuring the current from the beam captured by the Faraday cage behind the sample stage.

Typically, samples are continuously irradiated for a day or more, which with the rate of 3 x $10^{-}5$ C/s cm^2 [19], will accumulate a dose of $\sim$ 2.5 C/cm^2 in a 24 hour period.

2.4 References

[1] W. Meissner and R. Ochsenfeld. Ein neuer effekt bei eintritt der supraleitfähigkeit. *Naturwissenschaften*, 21(44):787–788, Nov 1933.

[2] F. London and H. London. The electromagnetic equations of the supraconductor. *Proceedings of the Royal Society of London A: Mathematical, Physical and Engineering Sciences*, 149(866):71–88, 1935.

[3] Kristian Fossheim and Asle Sudboe. *Superconductivity: Physics and Applications*. Wiley, 2004.

[4] C. J. Gorter and H. B. Casimir. *Zur thermodynamik des supraleitenden zustandes Phys. Z.*, 35:963, 1934.

[5] Ruslan Prozorov and Russell W. Giannetta. Magnetic penetration depth in unconventional superconductors. *Superconductor Science and Technology*, 19(8), 2006.

[6] Chandrasekhar B. S. and Einzel D. The superconducting penetration depth from the semiclassical model. *Annalen der Physik*, 505(6):535–546.

[7] R. T. Gordon. Ph. D. thesis, Iowa State University, 2011.

[8] R. Prozorov, R. W. Giannetta, A. Carrington, P. Fournier, R. L. Greene, P. Guptasarma, D. G. Hinks, and A. R. Banks. Measurements of the absolute value of the penetration depth in high-tc superconductors using a low-tc superconductive coating. *Applied Physics Letters*, 77(25):4202–4204, 12 2000.

[9] A. Carrington, R. W. Giannetta, J. T. Kim, and J. Giapintzakis. Absence of nonlinear meissner effect in $yba_2cu_3o_{6.95}$. *Phys. Rev. B*, 59:R14173–R14176, Jun 1999.

[10] A. Carrington, F. Manzano, R. Prozorov, R. W. Giannetta, N. Kameda, and T. Tamegai. Evidence for surface andreev bound states in cuprate superconductors from penetration depth measurements. *Phys. Rev. Lett.*, 86:1074–1077, Feb 2001.

[11] R. Prozorov, R. W. Giannetta, A. Carrington, and F. M. Araujo-Moreira. Meissner-london state in superconductors of rectangular cross section in a perpendicular magnetic field. *Phys. Rev. B*, 62:115–118, Jul 2000.

[12] Craig T. Van Degrift. Tunnel diode oscillator for 0.001 ppm measurements at low temperatures. *Review of Scientific Instruments*, 46(5):599–607, 1975.

[13] Andrei Diaconu. Ultra-low Temperature Measurements of London Penetration Depth in Iron Selenide Telluride Superconductors. 2013.

[14] M. D. Vannette. Ph. D. thesis, Iowa State University, 2009.

[15] H. Kim. Ph. D. thesis, Iowa State University, 2013.

[16] R Prozorov and V G Kogan. London penetration depth in iron-based superconductors. *Reports on Progress in Physics*, 74(12):124505, 2011.

[17] N. Spyrison, M. A. Tanatar, Kyuil Cho, Y. Song, Pengcheng Dai, Chenglin Zhang, and R. Prozorov. Environmental stability and anisotropic resistivity of co-doped $na_{1-\delta}fe_{1-x}co_{x}as$. *Phys. Rev. B*, 86:144528, Oct 2012.

[18] Sultan Demirdi, Thierry Klein, Président Cyril, Proust Raporteur, Christoph Meingast, Raporteur Véronique, Brouet Examinateur, Dimitri Roditchev Examinateur, Luca Perfetti, Examinateur Cornelis, Jacominus Van Der, and Beek Directeur. *Effects of Disorder in Iron-Based Superconductors*. PhD thesis, 2012.

[19] R Prozorov, M Kończykowski, M A Tanatar, A Thaler, S L Bud'ko, P C Canfield, V Mishra, and P J Hirschfeld. Effect of Electron Irradiation on Superconductivity in Single Crystals of BaFe 1x Ru x 2 As 2 (x 0.24).

[20] Kyuil Cho, M. Kończykowski, S. Teknowijoyo, M. A. Tanatar, J. Guss, P. B. Gartin, J. M. Wilde, A. Kreyssig, R. J. McQueeney, A. I. Goldman, V. Mishra, P. J. Hirschfeld, and R. Prozorov. Using controlled disorder to probe the interplay between charge order and superconductivity in NbSe2. *Nature Communications*, 9(1):2796, dec 2018.

[21] P. Rodière, J. P. Brison, A. D. Huxley, F. Rullier Albenque, and J. Flouquet. Characterization of high energy electron irradiation damage in upt3 samples. *Journal of Low Temperature Physics*, 132(1):119–134, Jul 2003.

[22] M.J. Berger, J.S. Coursey, M.A. Zucker, and J. Chang. Stopping-power and range tables for electrons, protons, and helium ions. https://www.nist.gov/pml/stopping-power-range-tables-electrons-protons-and-helium-ions.

[23] A.C. Damask and G.J. Dienes. *Point Defects in Metals*. Gordon and Breach Science, 1963.

[24] The scattering of fast electrons by atomic nuclei. *Proceedings of the Royal Society of London A: Mathematical, Physical and Engineering Sciences*, 124(794):425–442, 1929.

[25] Calculations of cross - sections by electron irradiation. According to O. S. Oen (1965, 1973), C code by Daniel Lesueur, restored by Francois Beuneu. Ecole Polytechnique, Palaiseau, France, 1973.

[26] Yuta Mizukami, Marcin Konczykowski, Kohei Matsuura, Tatsuya Watashige, Shigeru Kasahara, Yuji Matsuda, and Takasada Shibauchi. Impact of disorder on the superconducting phase diagram in bafe2(as1xpx)2. *Journal of the Physical Society of Japan*, 86(8):083706, 2017.

CHAPTER 3. LONDON PENETRATION DEPTH AND ELECTRON IRRADIATION IN $Ba_{1-x}K_xFe_2As_2$

Modified from a manuscript published in

Science Advances 2, 9 e1600807 (2016)

Kyuil Cho,[1,2] Marcin Kończykowski,[3] Serafim Teknowijoyo,[1,2] Makariy A. Tanatar,[1,2] Yong Liu,[1] Thomas A. Lograsso,[1,4] Warren E. Straszheim,[1] Vivek Mishra,[5,6] Peter J. Hirschfeld,[7] Ruslan Prozorov[1,2]

[1] Ames Laboratory, Ames, IA 50011 USA

[2] Department of Physics and Astronomy, Iowa State University, Ames, IA 50011 USA

[3] Laboratoire des Solides Irradiés, École Polytechnique, CNRS, CEA, Université Paris-Saclay, 91128 Palaiseau Cedex, France.

[4] Department of Materials Science and Engineering, Iowa State University, Ames, IA 50011 USA

[5] Joint Institute for Computational Sciences, University of Tennessee, Knoxville, TN 37996, USA

[6] Center for Nanophase Materials Sciences, Oak Ridge National Laboratory, Oak Ridge, TN 37831, USA

[7] Department of Physics, University of Florida, Gainesville, FL 32611, USA

3.1 Abstract

The mechanism of unconventional superconductivity in iron-based superconductors is one of the most intriguing questions in current materials research. Among non-oxide iron-based superconductors, $(Ba_{1x}K_x)Fe_2As_2$ has been intensively studied because of its high superconducting transition temperature and fascinating evolution of the superconducting gap structure from being fully

isotropic at optimal doping ($x \approx 0.4$) to becoming nodal at $x > 0.8$. Although this marked evolution was identified in several independent experiments, there are no details of the gap evolution to date because of the lack of high-quality single crystals covering the entire K-doping range of the superconducting dome. We conducted a systematic study of the London penetration depth, $\lambda(T)$, across the full phase diagram for different concentrations of point-like defects introduced by 2.5-MeV electron irradiation. Fitting the low-temperature variation with the power law, $\Delta\lambda \sim T^n$, we find that the exponent n is the highest and the T_c suppression rate with disorder is the smallest at optimal doping, and they evolve with doping being away from optimal, which is consistent with increasing gap anisotropy, including an abrupt change around $x \simeq 0.8$, indicating the onset of nodal behavior. Our analysis using a self-consistent t-matrix approach suggests the ubiquitous and robust nature of $s_{\pm}$ pairing in iron-based superconductors and argues against a previously suggested transition to a d-wave state near $x = 1$ in this system.

3.2 Introduction

Among iron-based superconductors (FeSCs), the 122 family is one of the most versatile and adaptable systems in terms of doping substitution crystal growth. A typical compound is $BaFe_2As_2$ (Ba122) with the possibility of electron, hole or isovalent doping/substitution. For example, elements Ca, Sr, Na, K and Rb can all occupy the Ba site (Fig. 3.1(a)). Similarly the Fe site can be doped with Co, Ni or Ru and the As site with P. Although all of the combinations are interesting from the materials science perspective, only certain compounds are superconducting. In this case, the Ba122 parent compound is non-superconducting but superconductivity can be induced by doping or pressure. Co-, K- and P- doped 122 systems (Fig. 3.1(b)-(d)) in particular have been widely investigated because of their individual uniqueness and the availability of the high quality single crystals in recent years. The growth procedures for these compounds have been optimized over time and the current generation of samples exhibit relatively homogeneous concentration (from XRD and WDS measurements) and sharp superconducting transition (from thermodynamic and transport measurements). $Ba_{1-x}K_xFe_2As_2$ (K-Ba122) in particular stands out among its siblings

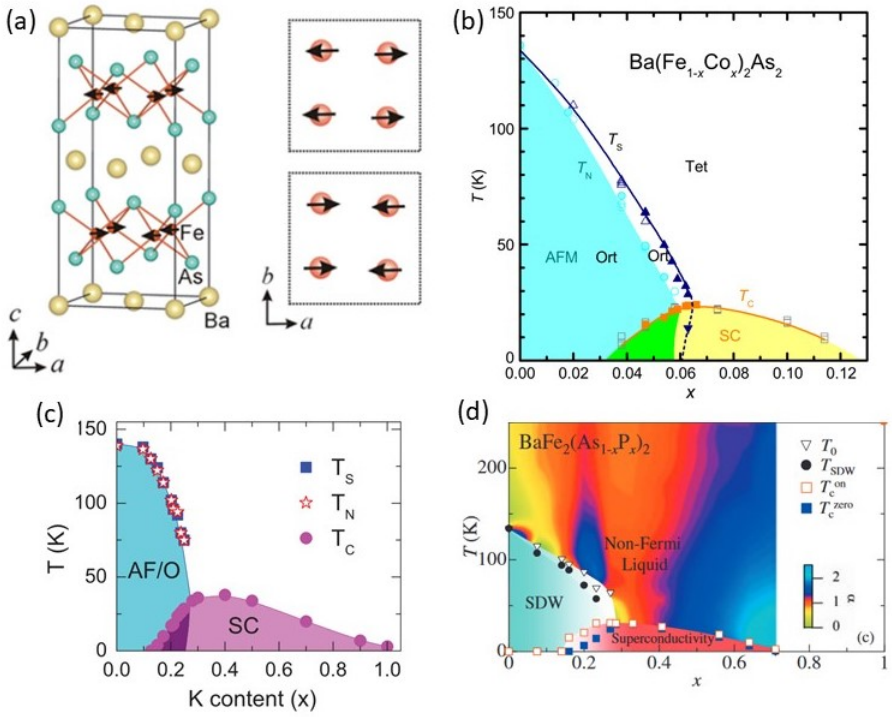

Figure 3.1 (a) The crystallographic structure of $BaFe_2As_2$. Arrows indicate the direction of the stripe antiferromagnetism of the Fe moments. (b) The phase diagram of Co-Ba122 system where there is separation of the magnetic and structural phase lines. (c) The phase diagram of K-Ba122 system with the superconducting dome reaching $x = 1.00$. (d) The phase diagram of P-Ba122 system where quantum critical point is observed. (a) From Ref. [1], (b) from Ref. [2], (c) from Ref. [3], (d) from Ref. [4].

because the optimum T_c is relatively high (39 K, for $x \sim 0.35$ - 0.4) and the superconducting dome covers a broad range of K composition from $x \approx 0.18$ to the pure KFe_2As_2 (K122) (see Fig. 3.1(c)). The underdoped region overlaps (coexists) with the AFM spin density wave phase, a trait shared with several other 122 systems. Other than the magnetic transition, the 122 family also undergoes a structural phase transition from tetragonal to orthorhombic which can be coincident (e.g. in K-Ba122 and P-Ba122) or separate (e.g. in Co-Ba122) from the magnetic phase transition line in the phase diagram (Fig. 3.1(b)-(d)).

Studies of the gap structure spanning the superconducting dome reveal an intriguing evolution from anisotropic but nodeless gaps in the underdoped region [5, 6, 7] to nodeless and effectively

isotropic gaps in the optimal region [8, 9, 10, 11], and further to a clearly nodal behavior at $x = 1$ [12, 13, 14, 15, 16]. The transition from nodeless to nodal is sometimes associated to the Lifshitz transition observed in the intermediate overdoped region ($x \sim 0.7$ - 0.8) [17, 18]. A Lifshitz transition is a reconstruction of the Fermi surface due to changes in the electronic band structure. In this case, the reconstruction happens when the electron pockets disappear as the Fermi level drops due to increasing hope doping (increasing K content). Near $x = 1$, only the center (hole) pockets remain and pairs are formed between electrons in the hole pockets. Prior to our work there have been many attempts to investigate the system in various limited doping ranges and therefore the results are rather fragmented. To fully investigate and track the gap structure evolution in this material, a systematic study with samples spanning the whole superconducting dome is very much desired. In this chapter a systematic study by our group using 16 different compositions of K-doped Ba122 across the T vs doping phase diagram [19] is described. We used London penetration depth and electron irradiation as the main means to probe the superconducting gap structure. These techniques capabilities and strong points have been described in the Ch. 1 and 2.

3.3 Sample Preparations

We received $Ba_{1-x}K_xFe_2As_2$ crystals from Yong Liu (Thomas Lograsso's group, Ames Laboratory). The samples used were grown using the inverted temperature gradient method. The starting materials, i.e. high purity Ba and K lumps, Fe and As powders, were weighed according to the desired composition and loaded into an alumina crucible inside a glove box with inert atmosphere. The alumina crucible was sealed in a tantalum tube by arc welding, then the tantalum tube was further sealed in a quartz ampoule to prevent oxidation of the tantalum. The crystallization processes from the top of the liquid melt help to expel impurity phases during the crystal growth, compared to nucleation centers inside the flux. Further details of the growth and characterization procedures for the entire dome can be found in Ref. [20, 21].

To pick the best crystals from the growth batches the samples were screened in the dipper probe (see Section 2.7). After crystals with the sharpest superconducting transition were selected,

the chemical compositions of each individual sample was determined using wavelength dispersive spectroscopy (WDS) in a JEOL JXA-8200 electron microprobe. WDS is one of the most accurate methods of elemental analysis which can find trace concentrations below 0.1% and resolve overlapping peaks in the energy dispersive spectroscopy (EDS) spectra [22]. In each sample, the composition was measured for 12 points per surface area and averaged [21]. At the end 16 different compositions ranging from $x = 0.20$ to 1.00 were identified, with more than one sample measured for each composition. The crystals had typical dimensions of 0.5 mm x 0.5 mm x 0.03 mm.

3.4 Results and Discussion

The raw data from our measurements are shown in in Fig. 3.2. A representative sample is selected for each of the 16 different compositions, which cover the underdoped ($x = 0.20$, 0.22, 0.25) and the optimal doping ($x = 0.32$, 0.35, 0.4, 0.47) regions in the top panel, along with the overdoped ($x = 0.54$, 0.6, 0.68, 0.78, 0.81, 0.83, 0.91, 0.92 and 1.00) region in the bottom panel. Throughout the experiment, each physical sample was measured in the pristine state and between irradiation runs (up to two cycles of irradiations). The information about T_c and dose of irradiation are listed in Fig. 3.3. Although not all of the samples were taken for irradiation, there is at least one representative from under, optimal or overdoped regions that was irradiated. In Fig. 3.2 the temperature dependence above T_c falls into two categories: whether $\lambda(T)$ becomes of the order of the sample size (size limited) or the normal state skin-depth (skin-depth limited). In the former (size limited) case, the skin-depth response of the material is larger than its physical size hence the curve is flat (temperature independent) above T_c. This is the case for $x = 0.20 - 0.35$. However, the opposite is true in the latter (skin-depth limited) case. When the skin-depth of the material is less than its physical size it is possible to capture the temperature dependence above T_c, as is the case for pristine $x = 0.40 - 1.00$. The skin-depth is proportional to the temperature dependent resistivity $\rho(T)$ from the expression $\delta(T) = (\rho(T)c^2/2\pi\omega)^2$, where $\omega = 2\pi f$ is the resonator frequency. Furthermore, since irradiation increases the residual resistivity it is possible

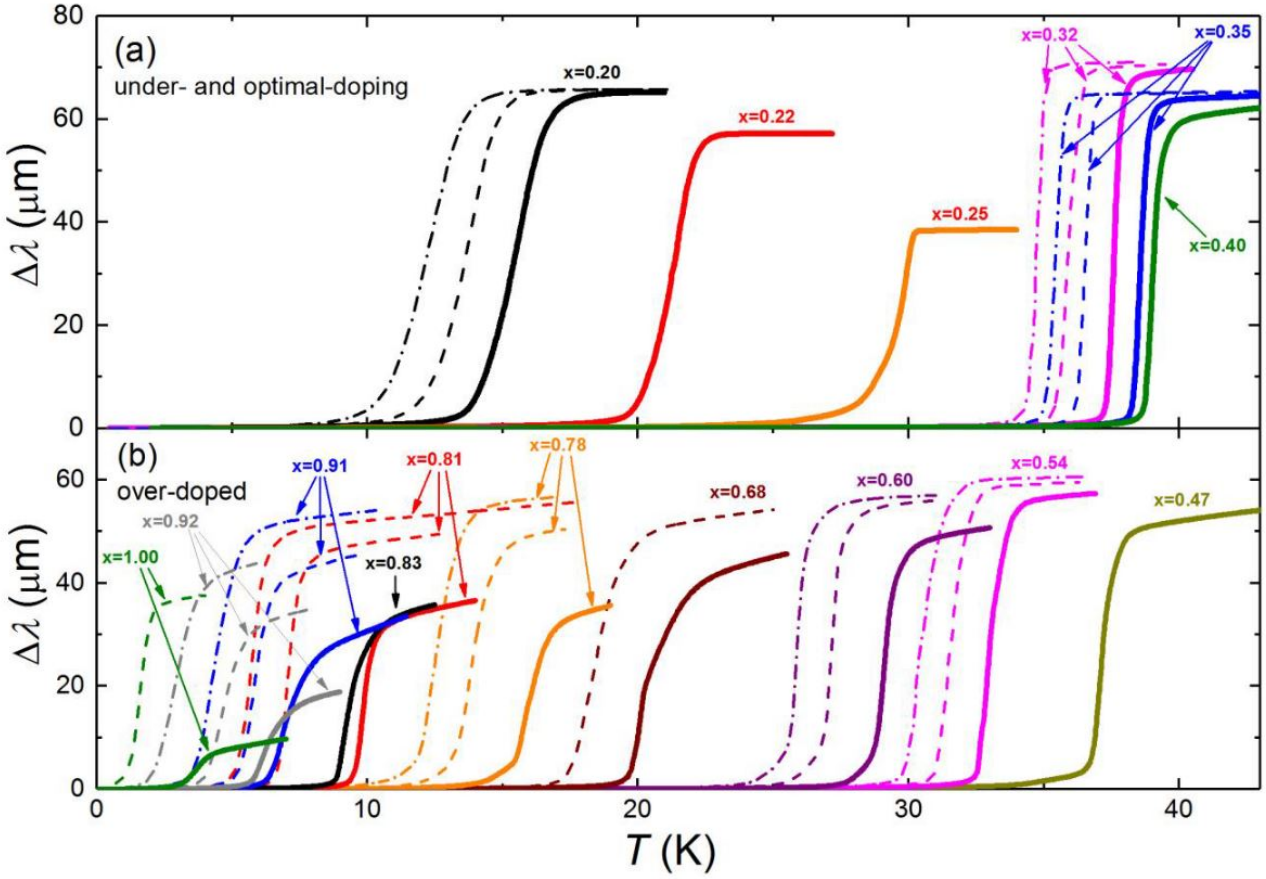

Figure 3.2 London penetration depth $\Delta\lambda(T)$ in the full temperature range for all compositions before (solid lines) and after (dashed lines) electron irradiation. Top panel (a) shows under and optimal doping, while bottom panel (b) shows the overdoped region. Irradiation doses are the same as Fig. 3.3. From Ref. [19] Supplemental Materials.

for a sample to switch over from skin-depth limited regime to size limited regime, as is the case for $x = 0.54$ and 0.60.

The low temperature behavior of the London penetration depth in terms of the power law $\Delta\lambda(T) \propto (T/T_c)^n$ is shown in Fig. 3.3. The upper panels show $\Delta\lambda(T)$ on a fixed scale of 0 to 140 nm and at a temperature range of 0 to 0.3 (T/T_c), which in absolute scale reaches 50 mK using dilution refrigerator. Plotted in this way, it is clear that $\Delta\lambda(T)$ significantly increases as we move away from optimal doping (see also the Summary Figure 3.5(c)). At small x this trend is naturally explained in terms of the competition between superconducting and SDW order [5, 6, 23]. The increase toward the underdoped region is quite monotonic, whereas the increase toward $x = 1$ is distinctly non-monotonic. At $x = 0.81$ there is a small decrease compared to $x = 0.78$, which is coincident with the anomaly at T_c (Fig. 3.5(a)) and where the Lifshitz transition is suspected to occur [17]. Similar non-monotonicity in the same region was reported before [14] so it seems that this is not an experimental aberration. In fact, this feature may signal the onset of accidental nodes near the Lifshitz transition [24] where a fully gapped $\Delta(\phi)$ near the expected nodal region transits to a linear-in-ϕ dependence through an intermediate quadratic, $\Delta(\phi) \sim \phi^2$, dependence. Although the non-monotonicity provides only a circumstantial evidence of the onset of accidental nodes since it is not a unique cause, accidental nodes can naturally lead to the observed non-monotonic behavior.

The lower panels in Fig. 3.3 show the exponent n obtained in the power-law fitting (see also Fig. 3.5(d)). To examine the robustness of the power-law representation, fitting of $\Delta\lambda(T/T_c)$ was performed from the base temperature up to three different upper limits $T_{up}/T_c = 0.20$, 0.25 and 0.30. The results are shown by the three points in each frame of the lower panel. Horizontal lines show three principal limits of the exponent n expected for different scenarios. A clean, nodal gap corresponds to $n \approx 1$ whereas exponential behavior is experimentally not distinguishable from a large exponent ($n \gtrsim 3$). In all cases, $n = 2$ is the terminal dirty limit for any scenario with pair-breaking ($s_\pm$ or d-wave). On the other hand, for s_{++} pairing n will still stay exponential because non-magnetic scattering is not pair-breaking.

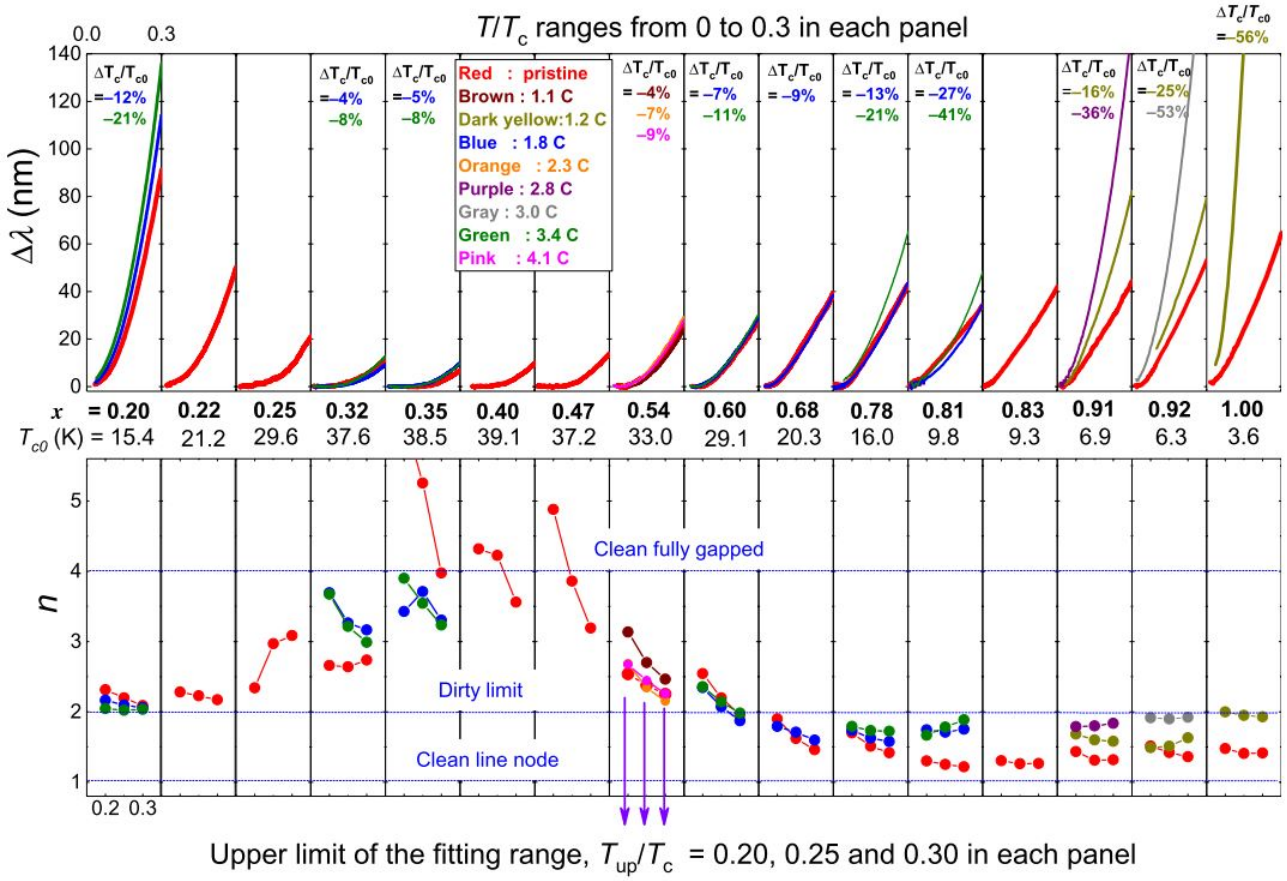

Figure 3.3 The evolution of the temperature dependent part of London penetration depth, $(\Delta\lambda(T))$, with electron irradiation. Upper panels: $\Delta\lambda(T/T_c)$ for 16 different compositions before and after electron irradiation. Each individual panel shows a low-temperature region of $T/T_c < 0.3$ (full-range curves are shown in Fig. 3.2). In the absolute scale, the measurements were taken down to 50 mK using a TDR set up housed in a dilution refrigerator [25]. Lower panels: Exponent n obtained from the power-law fitting, $\Delta\lambda \propto (T/T_c)^n$. For each curve, three different upper-limit temperatures were used, $T_{up}/T_c = 0.20$, 0.25 and 0.30, whereas the lower limit was fixed by the lowest experimental temperature. From Ref. [19].

The measurements after irradiation are shown in different colors for each dose as listed in the legend. At small x (e.g. $x = 0.20$) in the coexistence regime, the gap anisotropy increases however we find no evidence of nodes since n stays ≥ 2 even upon irradiation which is consistent with previous reports [5, 6, 7]. This result argues against an s_{++} scenario in which the reconstruction of Fermi surfaces due to SDW order must lead to robust nodes [23]. Upon irradiation T_c slowly decreases suggesting moderate gap anisotropy and the presence of small, but significant interband impurity scattering [26]. Close to the optimal composition at $x = 0.35$ the penetration depth exponent n decreases significantly with irradiation yet remains ≥ 3, providing strong evidence for $s_{\pm}$ pairing with robust full gaps. This is also consistent with the sizable T_c suppression (8%) which is contrary to the expectation for s_{++} scenario. In the latter (s_{++}) case disorder averages the gap over the Fermi surface, leading inevitably to the increase of the minimum gap and therefore an increase in the exponent n and a very robust T_c. Moving to higher x away from optimal composition, the gap anisotropy is smeared out and the exponent increases and the exponent n for the pristine samples decreases. Upon irradiation the gap anisotropy is smeared out and the exponent increases even in the $s_{\pm}$ case, provided that all bands are still fully gapped and the intraband impurity scattering is dominant. This is apparently the case for $x = 0.54$. For still higher doping levels the anisotropy becomes so strong that the system develops accidental nodes ($n \to 1$). Although a case can be made to argue for a symmetry protected (e.g. d-wave) origin of the observed nodal behavior, a careful look at the low temperature region of $x > 0.9$ samples can help distinguish between real nodes (symmetry protected) or nodes developing from deep minima scenarios (see Fig. 3.4). For pristine $x = 1.00$ both s- and d-wave models give reasonable fits by the t-matrix procedure (explained in more details in the Analysis section). However, pristine data of $x = 0.91$ and $x = 0.92$ still contain saturation curvatures at low temperatures which is incompatible with d-wave (taking into account only cos 2ϕ angular contribution, which is commonly done). On the other hand, the extended $s_{\pm}$ scenario can fit the data well. Therefore it is more natural to explain the observed nodal behavior in terms of $s_{\pm}$ pairing symmetry which gradually develops deep anisotropy, leading to accidental nodes somewhere before $x = 1$. Upon irradiation, we observe that the nodes are apparently not

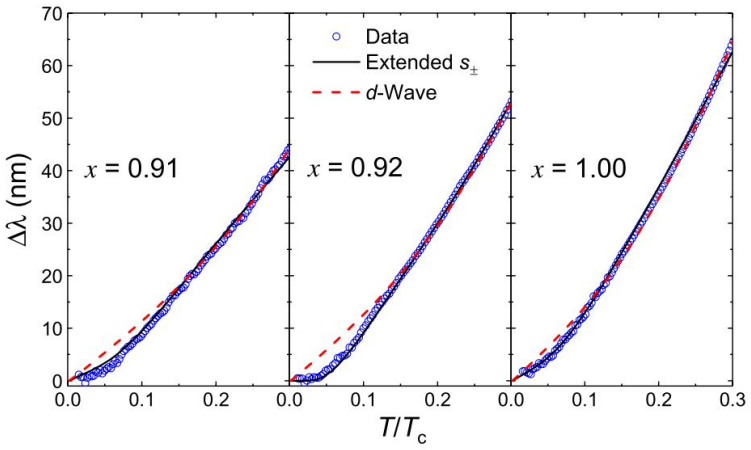

Figure 3.4 The change in penetration depth for the $x > 0.9$ samples fitted with symmetry imposed d-wave and $s_{\pm}$ states. For d-wave fit, both the hole bands are assumed to have gaps of the $\Delta_{h_1/h_2} \cos 2\phi$ form. The gap magnitudes $(\Delta_{01}, \Delta_{02})$ for dopings $x = 0.91$, 0.92 and 1.00 are (1.5,1.8), (1.6,1.2) and (1.0,1.2), respectively, in units of T_c. From Ref. [19].

lifted by disorder [27]. This is possibly due to the substantial change in the electronic band structure approaching the Lifshitz transition and/or the significant interband impurity scattering. Note that this evolution is very different from the isovalently substituted P-Ba122 [28] in which the line nodes are found at all x values and the band structure is unchanged throughout the dome. In our case, at a large x the exponential temperature dependence in pristine samples changes to $\sim T^2$ at around $x = 0.60$ and tends toward $\sim T$ at $x \geq 0.80$, consistent with the assumption of gradually developing nodes. Compared to the optimally doped region, the electron irradiation is much more effective in decreasing T_c; 41% upon 3.4 C/Cm^2 ($x = 0.81$) and 56% upon 1.2 C/cm^2 ($x = 1.00$). Nevertheless, the exponent n never exceeds 2 (e.g. no lifting of the accidental nodes).

3.5 Analysis and Summary

The summary of the effect of irradiation on T_c, $\Delta\lambda(0.3T_c)$ and $n(0.3T_c)$ throughout the dome are given in Fig. 3.5(a), (c) and (d), respectively. The superconducting transition temperature $T_c(x)$ was determined as the midpoint of the transition in penetration depth measurement (see Fig. 3.2).

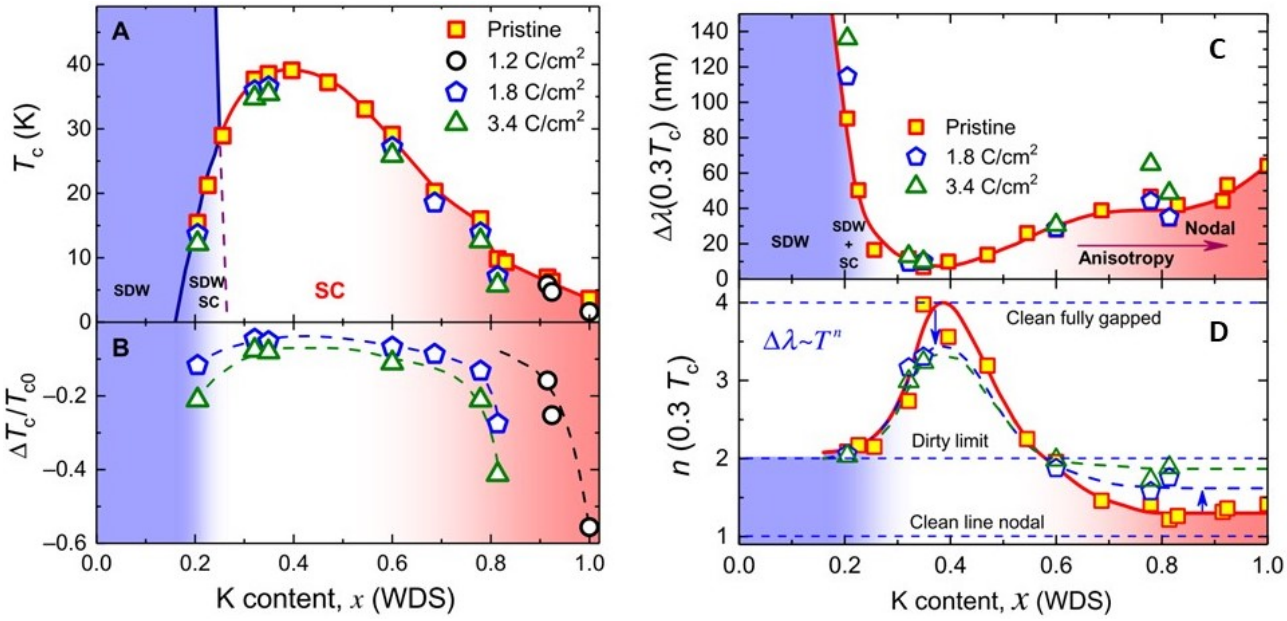

Figure 3.5 Summary figures of the key experimental parameters in 16 samples of $Ba_{1-x}K_xFe_2As_2$ as function of composition. (a) Temperature-composition phase diagram with $T_c(x)$ in pristine (squares) and electron-irradiated (other symbols, see legend) samples. The same set of symbols are used for (b)-(d). The approximate region of spin-density wave (SDW), superconducting (SC) phases and nodal behavior are color shaded blue, white and red, respectively. (b) Normalized $\Delta T_c/T_{c0}$, with the largest T_c suppression is found for $x \gtrsim 0.8$. (c) Absolute change of $\Delta\lambda$ from 0 to $0.3T_c$ for all compositions, with an anomaly at $x \approx 0.8$. (d) Composition dependence of the power-law exponent n for pristine and irradiated samples. As the irradiation dose increases, the exponent approaches but never exceeds the value of $n = 2$. From Ref. [19].

Although the evolution of $T_c(x)$ across the dome is generally smooth, there is an apparent steep drop near $x = 0.80$. This anomaly correlates with the appearance of accidental nodes induced in this material as a consequence of the Lifshitz transition [24]. The anomaly is also present in Fig. 3.5(b), where the relative change $(T_c - T_{c0})/T_{c0}$ is shown for the same samples as in (a). At $x > 0.80$ the T_c suppression rate shows a sudden jump, consistent with the increasing anisotropy in the gap structure. In terms of the rate per irradiation dose, the normalized suppression rate of optimally doped samples (Fig. 3.6) is about 0.025 per 1 C/cm^2 and increases to 0.07 per C/Cm^2 in the underdoped samples ($x = 0.22$) which is consistent with our previous report [5]. In a sharp contrast, the suppression rate increases significantly in the far overdoped region reaching 0.47 per C/cm^2, which is 20 times larger than that of the optimally doped regime. Note however, that because of magnetic ordering the rates of samples in the under and overdoped regimes are not to be compared directly and a separate analysis is required to take into account the competition between superconductivity and magnetism [6]. Nevertheless, all these numbers for the rate of T_c suppression are much greater than those expected from conventional s_{++} pairing and they can be explained within a generalized $s_{\pm}$ pairing model if one is allowed to tune gap anisotropy and ratio of interband/intraband scattering [29].

For the theory modeling we collaborated with Vivek Mishra (Oak Ridge National Laboratory), Saurabh Maiti and Peter Hirschfeld (both from University of Florida). They used the self-consistent t-matrix formalism and sign-changing $s_{\pm}$ state to describe both the London penetration depth and the T_c suppression rate for different levels of disorder [30, 31, 32, 33]. To keep the analysis tractable and to fit the experimental data they minimized the parameter set by working in the 2Fe-BZ and modeling the gap structure as shown schematically in Fig. 3.7(a). Here a minimal two-band model was used which corresponds to hole (at Γ point) and electron (at M point) bands before the Lifshitz transition. After the transition the electron pockets disappear and the two bands switch to the two hole pockets. The gap magnitudes and an overall scaling factor that comes into play from the contribution from the Fermi velocities and the density of states for various doping concentrations are used as the fitting parameters. Although the actual band structure is more complex and involves

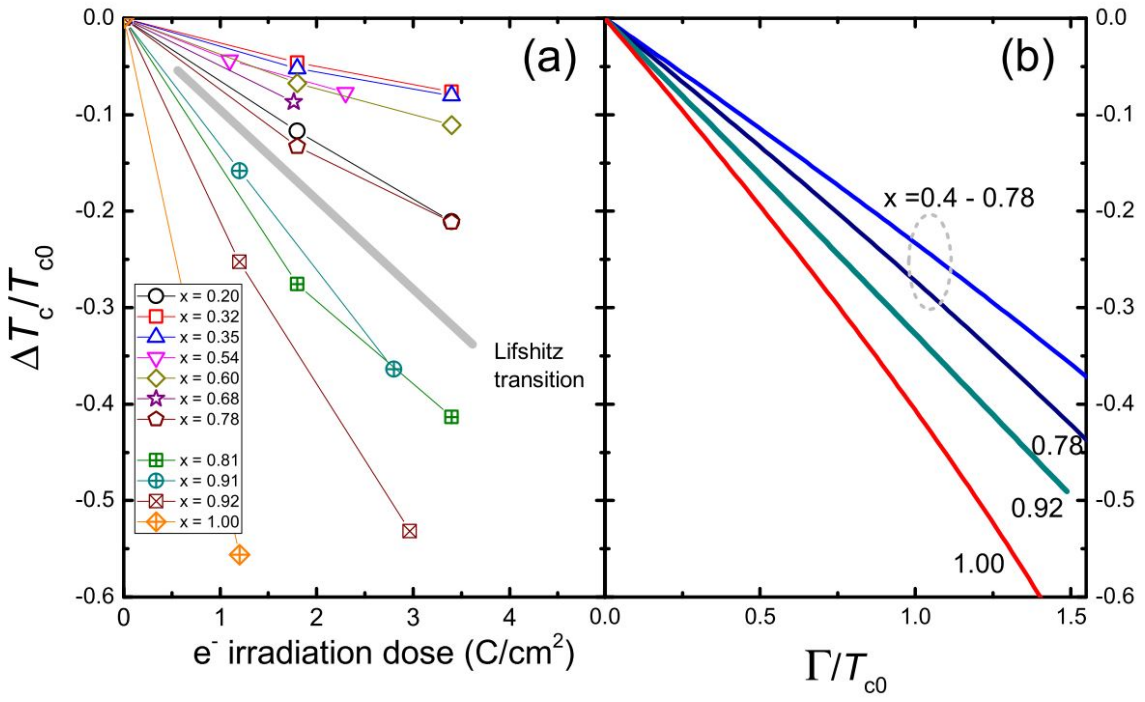

Figure 3.6 The variation of superconducting critical temperature upon irradiation for different compositions. (a) The normalization rate of experimentally observed T_c suppression vs. irradiation dose. The rate increases drastically above the Lifshitz transition. (b) t-matrix calculations of the T_c change using parameters extracted from the London penetration depth fits, Fig. 3.8. While we cannot expect quantitative agreement for our simplified model, the trend is clearly in line with experimental observation. From Ref. [19] Supplemental Materials.

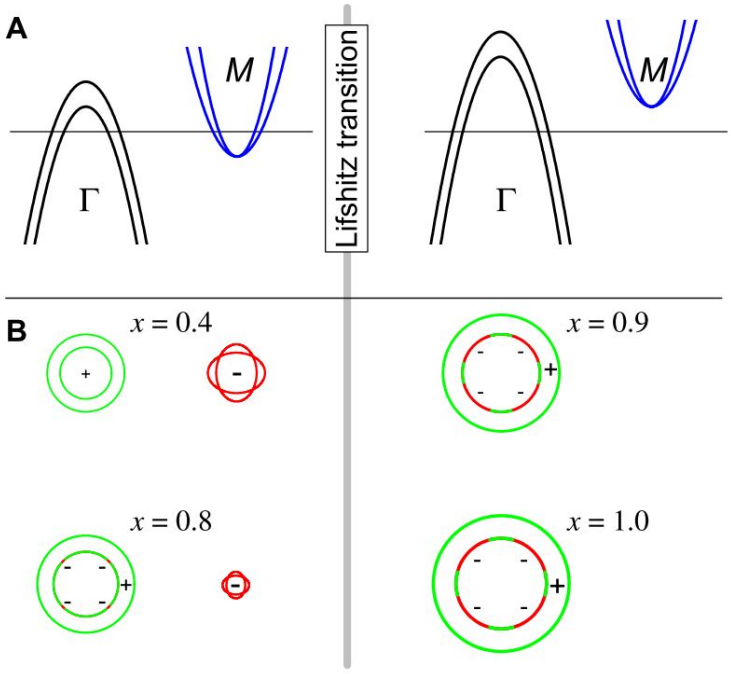

Figure 3.7 A schematic illustration of the effective band structure and order parameter evolution with doping. (a) The change in the electronic band structure across the Lifshitz transition. The electron pocket at M is lifted but remains in the vicinity of E_{F}. The extended $s_{\pm}$ pairing survives, but is shifted to the hole bands at the Γ point. (b) Hole and electron pockets relevant for calculations with the sign-changing order parameter. Signs are encoded by green (+) and red(-) colors. From Ref. [19].

several bands transforming across the Lifshitz transition, we find that a model with two effective gaps with each having isotropic and anisotropic parts is sufficient to explain the observed results. The model gap functions are

$$\begin{aligned} \Delta_1 &= \Delta_{01}\ (1.0 + r_1\ \cos\ 4\phi) \\ \Delta_2 &= \Delta_{02}\ (1.0 + r_2\ \cos\ 4\phi) \end{aligned} \tag{3.1}$$

where the angle ϕ is measured from the zone diagonal. First the fit was done on the low temperature penetration depth for the pristine samples to find the gap amplitudes in the units of the pristine sample's transition temperature T_{c0}. They are shown in Fig. 3.8 which clearly trace the experimental data well. Once the gaps were determined, the interactions which generate these gaps within the weak-coupling BCS approximation can be calculated. The authors parametrized the in-

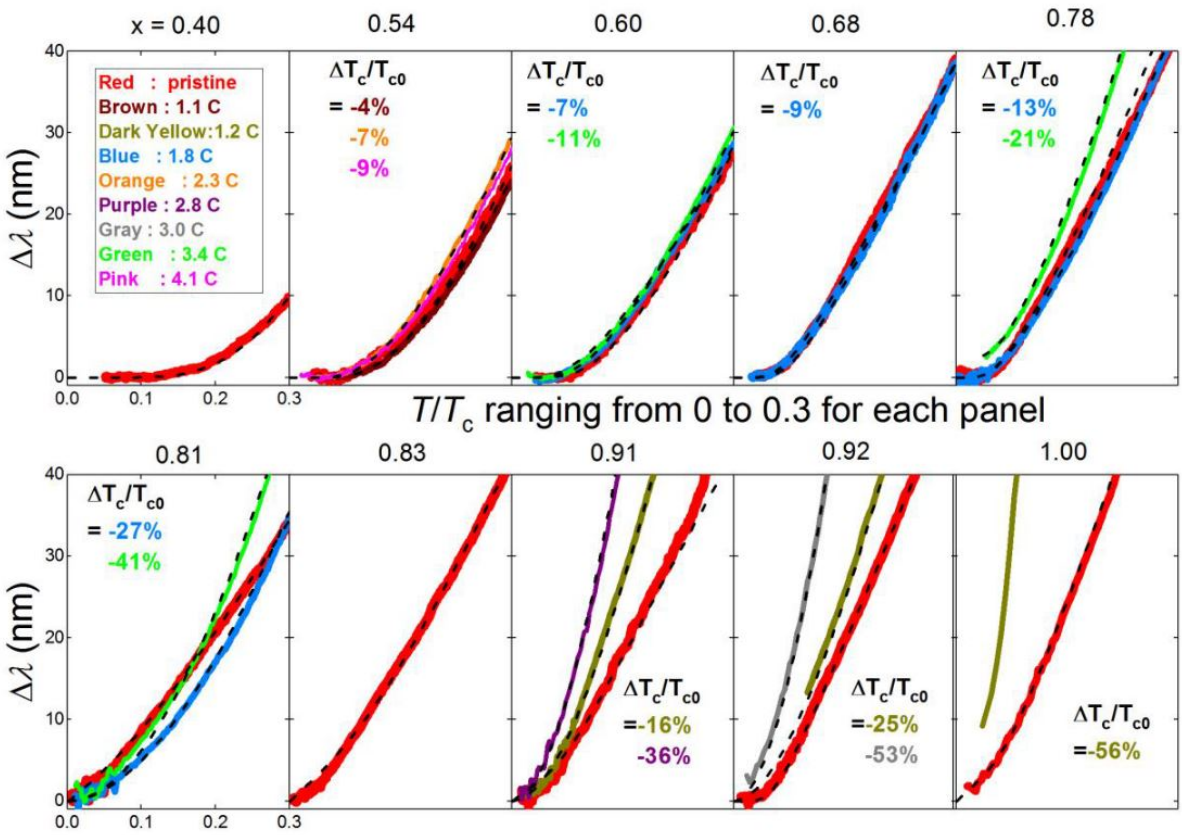

Figure 3.8 t-matrix fitting of the London penetration depth for compositions $x = 0.4$ to $x = 1.00$. The extracted gap magnitudes are plotted in Fig. 3.9. From Ref. [19] Supplemental Materials.

teraction potential in a simple form to reduce the number of parameters where they have assumed the angular form factors in the interactions to be the same as in the one in the gap structure.

$$\begin{aligned} V_{11} &= V_1\ (1.0 + r_1\ \cos\ 4\phi)\ (1.0 + r_1\ \cos\ 4\phi') \\ V_{22} &= V_2\ (1.0 + r_2\ \cos\ 4\phi)\ (1.0 + r_2\ \cos\ 4\phi') \end{aligned} \tag{3.2}$$

$$V_{12} = V'\ [(1.0 + r_1\ \cos\ 4\phi)\ (1.0 + r_2\ \cos\ 4\phi') + (1.0 + r_2\ \cos\ 4\phi)\ (1.0 + r_1\ \cos\ 4\phi')] \tag{3.3}$$

Here V_{ij} denotes the interaction between i^{th} and j^{th} band. After finding the interaction parameters V_{ij}, impurity scattering was treated within self-consistent t-matrix approximation. The defects induced by electron irradiation were modeled as point scatterers which scatter between the bands with a fixed interband amplitude and within the same band with another intraband amplitude.

The presence of interband impurity scattering and the relative sign change between these two bands are necessary to explain the T_c suppression and the increase of penetration depth in the irradiated samples. Before the Lifshitz transition, the best fit is acquired when the ratio between the interband and the intraband impurity potentials is 0.6. After the Lifshitz transition the interband scattering involves two concentric hole pockets, which has a small momentum transfer. Because the two pockets are almost overlapping after the Lifshitz transition the strengths of interband and intraband impurity scattering are taken as equal with the ratio of 1. The fitting procedure yields T_c suppression rate shown in Fig. 3.6(b), which is sufficient to qualitatively explain the experimental observation (Fig. 3.6(a)). However, to get better quantitative agreement between the experimental data and calculation a full multiband approach beyond the minimal two-band model with realistic Fermi surfaces is necessary. As an additional note, we point out that the previously accepted paradigm about nesting between hole and electron pockets as a precondition for $s_\pm$ pairing [34] has started to shift. Several authors have proposed the possibility of $s_\pm$ pairing arising from solely hole-hole interactions [14, 35] which is the case here.

3.6 Conclusions

In conclusion we find that the effective two-band model with generalized sign-changing $s_\pm$ pairing can naturally and consistently describe the evolution of the gap structure in $Ba_{1-x}K_xFe_2As_2$ throughout the superconducting dome, including the crossover at the Lifshitz transition. The data from low temperature London penetration depth measurements combined with T_c suppression due to electron irradiation provide stringent constraints on the possible gap structures. We are able to rule out global s_{++} symmetry because it is incompatible with the rate of T_c suppression that we observe from non-magnetic impurities in the optimal doping region. At the highly overdoped region ($x = 0.91$, 0.92) the low temperature penetration depth fitting favors $s_\pm$ over d-wave pairing. d-wave is predicted by other studies to be competitive [34, 35] but remaining a subleading interaction [36, 37, 38]. In principle, our observation alone is not sufficient to rule out a crossover to d-wave

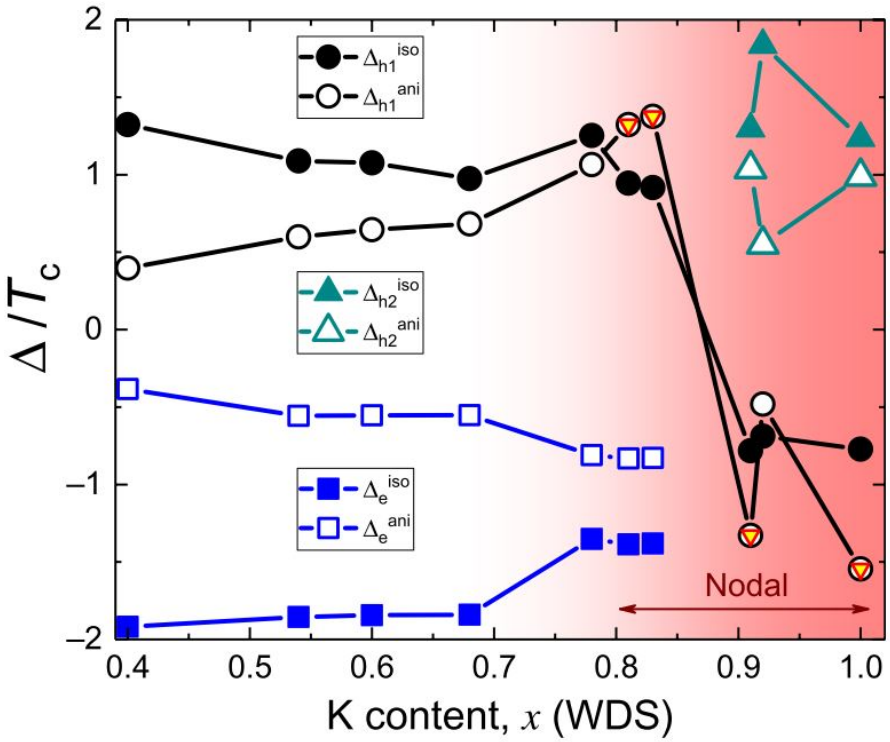

Figure 3.9 The evolution of the superconducting gaps in K-Ba122 with composition, x, obtained from the self-consistent t-matrix fitting (see Fig. 3.8 as described in the text). Assumed angular variations of the gaps is shown schematically in Fig. 3.7. As long as the isotropic part is greater than the anisotropic one, the state is nodeless (that is, for $x < 0.8$). In the opposite limit, the nodes appear. This is shown by inscribed triangles in the figure for h_1 contribution. Consequently, the $s_{\pm}$ pairing switches from hole-electron pockets below the Lifshitz transition to hole-hole above. From Ref. [19].

between $x = 0.92$ and 1.00 but ARPES measurements provide a strong argument against this scenario because of the presence of accidental nodes at $x = 1.00$ [39, 40].

Lastly, by using a generalized $s_{\pm}$ model and t-matrix calculations we calculated the gap magnitudes (in units of T_c) and their evolution from $x = 0.4$ to $x = 1.00$ which is shown in Fig. 3.9. We find that the biggest gap magnitudes Δ^{max}/T_c, fall between 1 - 2 which are consistent with other reports [41]. Before the Lifshitz transition (depicted at $x \approx 0.8$ in Fig. 3.9), sign change happens between the electron (blue squares) and hole (black circles) pockets. The isotropic parts in both pockets are larger (in magnitude), consistent with the absence of nodes observed. As dop-

ing increases the anisotropic contribution in the hole pocket also gradually gets larger and finally overtakes the isotropic term near the Lifshitz transition, leading to accidental nodes. After the transition the electron band disappears and the hole pocket switches its sign, allowing $s_{\pm}$ pairing with a second hole pockets (green triangles). Most of our data points agree with ARPES data [40] that the nodes are preserved all the way until $x = 1.00$. Our result is also highly compatible with other works that probe the gap structure in the underdoped region where superconductivity coexist with magnetism [5, 6]. Together, this provides a strong evidence for global $s_{\pm}$ pairing symmetry in the $Ba_{1-x}K_xFe_2As_2$ series.

3.7 References

[1] Q. Huang, Y. Qiu, Wei Bao, M. A. Green, J. W. Lynn, Y. C. Gasparovic, T. Wu, G. Wu, and X. H. Chen. Neutron-diffraction measurements of magnetic order and a structural transition in the parent $bafe_2as_2$ compound of feas-based high-temperature superconductors. *Phys. Rev. Lett.*, 101:257003, Dec 2008.

[2] S. Nandi, M. G. Kim, A. Kreyssig, R. M. Fernandes, D. K. Pratt, A. Thaler, N. Ni, S. L. Bud'ko, P. C. Canfield, J. Schmalian, R. J. McQueeney, and A. I. Goldman. Anomalous suppression of the orthorhombic lattice distortion in superconducting $Ba(fe_{1-x}co_x)_2as_2$ single crystals. *Phys. Rev. Lett.*, 104:057006, Feb 2010.

[3] S. Avci, O. Chmaissem, D. Y. Chung, S. Rosenkranz, E. A. Goremychkin, J. P. Castellan, I. S. Todorov, J. A. Schlueter, H. Claus, A. Daoud-Aladine, D. D. Khalyavin, M. G. Kanatzidis, and R. Osborn. Phase diagram of $ba_{1-x}k_xfe_2as_2$. *Phys. Rev. B*, 85:184507, May 2012.

[4] S. Kasahara, T. Shibauchi, K. Hashimoto, K. Ikada, S. Tonegawa, R. Okazaki, H. Shishido, H. Ikeda, H. Takeya, K. Hirata, T. Terashima, and Y. Matsuda. Evolution from non-fermi- to fermi-liquid transport via isovalent doping in $bafe_2(As_{1-x}P_x)_2$ superconductors. *Phys. Rev. B*, 81:184519, May 2010.

[5] K. Cho, M. Kończykowski, J. Murphy, H. Kim, M. A. Tanatar, W. E. Straszheim, B. Shen, H. H. Wen, and R. Prozorov. Effects of electron irradiation on resistivity and london penetration depth of $ba_{1-x}k_xfe_2as_2 (x \leq 0.34)$ iron-pnictide superconductor. *Phys. Rev. B*, 90:104514, Sep 2014.

[6] H. Kim, M. A. Tanatar, W. E. Straszheim, K. Cho, J. Murphy, N. Spyrison, J.-Ph. Reid, Bing Shen, Hai-Hu Wen, R. M. Fernandes, and R. Prozorov. Competition between superconductivity and magnetic/nematic order as a source of anisotropic superconducting gap in underdoped $ba_{1-x}k_xfe_2as_2$. *Phys. Rev. B*, 90:014517, Jul 2014.

[7] J.-Ph. Reid, M. A. Tanatar, X. G. Luo, H. Shakeripour, S. René de Cotret, A. Juneau-Fecteau, J. Chang, B. Shen, H.-H. Wen, H. Kim, R. Prozorov, N. Doiron-Leyraud, and Louis Taillefer. Doping evolution of the superconducting gap structure in the underdoped iron arsenide ba$_{1-x}$k$_x$fe$_2$as$_2$ revealed by thermal conductivity. *Phys. Rev. B*, 93:214519, Jun 2016.

[8] H. Ding, P. Richard, K. Nakayama, K. Sugawara, T. Arakane, Y. Sekiba, A. Takayama, S. Souma, T. Sato, T. Takahashi, Z. Wang, X. Dai, Z. Fang, G. F. Chen, J. L. Luo, and N. L. Wang. Observation of fermi-surfacedependent nodeless superconducting gaps in ba 0.6 k 0.4 fe 2 as 2. *EPL (Europhysics Letters)*, 83(4):47001, 2008.

[9] K. Nakayama, T. Sato, P. Richard, Y.-M. Xu, Y. Sekiba, S. Souma, G. F. Chen, J. L. Luo, N. L. Wang, H. Ding, and T. Takahashi. Superconducting gap symmetry of ba 0.6 k 0.4 fe 2 as 2 studied by angle-resolved photoemission spectroscopy. *EPL (Europhysics Letters)*, 85(6):67002, 2009.

[10] X. G. Luo, M. A. Tanatar, J.-Ph. Reid, H. Shakeripour, N. Doiron-Leyraud, N. Ni, S. L. Bud'ko, P. C. Canfield, Huiqian Luo, Zhaosheng Wang, Hai-Hu Wen, R. Prozorov, and Louis Taillefer. Quasiparticle heat transport in single-crystalline ba$_{1-x}$k$_x$fe$_2$as$_2$: Evidence for a k-dependent superconducting gap without nodes. *Phys. Rev. B*, 80:140503, Oct 2009.

[11] D V Evtushinsky, D S Inosov, V B Zabolotnyy, M S Viazovska, R Khasanov, A Amato, H-H Klauss, H Luetkens, Ch Niedermayer, G L Sun, V Hinkov, C T Lin, A Varykhalov, A Koitzsch, M Knupfer, B Büchner, A A Kordyuk, and S V Borisenko. Momentum-resolved superconducting gap in the bulk of Ba _{1 x} K _x Fe ₂ As ₂ from combined ARPES and μSR measurements. *New Journal of Physics*, 11(5):055069, may 2009.

[12] K. Hashimoto, A. Serafin, S. Tonegawa, R. Katsumata, R. Okazaki, T. Saito, H. Fukazawa, Y. Kohori, K. Kihou, C. H. Lee, A. Iyo, H. Eisaki, H. Ikeda, Y. Matsuda, A. Carrington, and T. Shibauchi. Evidence for superconducting gap nodes in the zone-centered hole bands of kfe$_2$as$_2$ from magnetic penetration-depth measurements. *Phys. Rev. B*, 82:014526, Jul 2010.

[13] J.-Ph. Reid, M. A. Tanatar, A. Juneau-Fecteau, R. T. Gordon, S. René de Cotret, N. Doiron-Leyraud, T. Saito, H. Fukazawa, Y. Kohori, K. Kihou, C. H. Lee, A. Iyo, H. Eisaki, R. Prozorov, and Louis Taillefer. Universal heat conduction in the iron arsenide superconductor kfe$_2$as$_2$: Evidence of a d-wave state. *Phys. Rev. Lett.*, 109:087001, Aug 2012.

[14] D. Watanabe, T. Yamashita, Y. Kawamoto, S. Kurata, Y. Mizukami, T. Ohta, S. Kasahara, M. Yamashita, T. Saito, H. Fukazawa, Y. Kohori, S. Ishida, K. Kihou, C. H. Lee, A. Iyo, H. Eisaki, A. B. Vorontsov, T. Shibauchi, and Y. Matsuda. Doping evolution of the quasiparticle excitations in heavily hole-doped ba$_{1-x}$k$_x$fe$_2$as$_2$: A possible superconducting gap with sign-reversal between hole pockets. *Phys. Rev. B*, 89:115112, Mar 2014.

[15] Takahiro Shimojima, Kozo Okazaki, and Shik Shin. Low-Temperature and High-Energy-Resolution Laser Photoemission Spectroscopy. *Journal of the Physical Society of Japan*, 84(7):072001, jul 2015.

[16] Xiao-Chen Hong, Ai-Feng Wang, Zhen Zhang, Jian Pan, Lan-Po He, Xi-Gang Luo, Xian-Hui Chen, and Shi-Yan Li. Doping Evolution of the Superconducting Gap Structure in Heavily Hole-Doped Ba _{1 x} K _x Fe ₂ As ₂ : a Heat Transport Study. *Chinese Physics Letters*, 32(12):127403, dec 2015.

[17] N. Xu, P. Richard, X. Shi, A. van Roekeghem, T. Qian, E. Razzoli, E. Rienks, G.-F. Chen, E. Ieki, K. Nakayama, T. Sato, T. Takahashi, M. Shi, and H. Ding. Possible nodal superconducting gap and lifshitz transition in heavily hole-doped $ba_{0.1}k_{0.9}fe_2as_2$. *Phys. Rev. B*, 88:220508, Dec 2013.

[18] P Richard, T Qian, and H Ding. ARPES measurements of the superconducting gap of Fe-based superconductors and their implications to the pairing mechanism. *Journal of Physics: Condensed Matter*, 27(29):293203, jul 2015.

[19] K. Cho, M. Konczykowski, S. Teknowijoyo, M. A. Tanatar, Y. Liu, T. A. Lograsso, W. E. Straszheim, V. Mishra, S. Maiti, P. J. Hirschfeld, and R. Prozorov. Energy gap evolution across the superconductivity dome in single crystals of (Ba1-xKx)Fe2As2. *Science Advances*, 2(9):e1600807–e1600807, 2016.

[20] Yong Liu, M. A. Tanatar, V. G. Kogan, Hyunsoo Kim, T. A. Lograsso, and R. Prozorov. Upper critical field of high-quality single crystals of kfe_2as_2. *Phys. Rev. B*, 87:134513, Apr 2013.

[21] Y. Liu, M. A. Tanatar, W. E. Straszheim, B. Jensen, K. W. Dennis, R. W. McCallum, V. G. Kogan, R. Prozorov, and T. A. Lograsso. Comprehensive scenario for single-crystal growth and doping dependence of resistivity and anisotropic upper critical fields in $(ba_{1-x}k_x)fe_2as_2$ $(0.22 \leq x \leq 1)$. *Phys. Rev. B*, 89:134504, Apr 2014.

[22] Fisher Scientific. How wds and parallel beam spectroscopy work. https://fscimage.fishersci.com/images/D10994~.pdf.

[23] D. Parker, M. G. Vavilov, A. V. Chubukov, and I. I. Mazin. Coexistence of superconductivity and a spin-density wave in pnictide superconductors: Gap symmetry and nodal lines. *Phys. Rev. B*, 80:100508, Sep 2009.

[24] S. Maiti, M. M. Korshunov, and A. V. Chubukov. Gap symmetry in kfe_2as_2 and the cos 4θ gap component in lifeas. *Phys. Rev. B*, 85:014511, Jan 2012.

[25] Hyunsoo Kim, M. A. Tanatar, and R. Prozorov. Tunnel diode resonator for precision magnetic susceptibility measurements in a mk temperature range and large dc magnetic fields. *Review of Scientific Instruments*, 89(9):094704, 2018.

[26] Vivek Mishra. Effect of disorder on superconductivity in the presence of spin-density wave order. *Phys. Rev. B*, 91:104501, Mar 2015.

[27] V. Mishra, G. R. Boyd, S. Graser, T. Maier, P. J. Hirschfeld, and D. J. Scalapino. Lifting of nodes by disorder in extended-s-state superconductors: Application to ferropnictides. *Phys. Rev. B*, 79:094512, Mar 2009.

[28] Y. Mizukami, M. Konczykowski, Y. Kawamoto, S. Kurata, S. Kasahara, K. Hashimoto, V. Mishra, A. Kreisel, Y. Wang, P. J. Hirschfeld, Y. Matsuda, and T. Shibauchi. Disorder-induced topological change of the superconducting gap structure in iron pnictides. *Nature Communications*, 5:5657, nov 2014.

[29] R Prozorov, M Kończykowski, M A Tanatar, A Thaler, S L Bud'ko, P C Canfield, V Mishra, and P J Hirschfeld. Effect of Electron Irradiation on Superconductivity in Single Crystals of BaFe 1x Ru x 2 As 2 (x 0.24).

[30] Peter J. Hirschfeld and Nigel Goldenfeld. Effect of strong scattering on the low-temperature penetration depth of a d-wave superconductor. *Phys. Rev. B*, 48:4219–4222, Aug 1993.

[31] P. J. Hirschfeld, P. Wölfle, and D. Einzel. Consequences of resonant impurity scattering in anisotropic superconductors: Thermal and spin relaxation properties. *Phys. Rev. B*, 37:83–97, Jan 1988.

[32] V. Mishra, A. Vorontsov, P. J. Hirschfeld, and I. Vekhter. Theory of thermal conductivity in extended-s state superconductors: Application to ferropnictides. *Phys. Rev. B*, 80:224525, Dec 2009.

[33] V. Mishra, S. Graser, and P. J. Hirschfeld. Transport properties of three-dimensional extended s-wave states in fe-based superconductors. *Phys. Rev. B*, 84:014524, Jul 2011.

[34] Ronny Thomale, Christian Platt, Werner Hanke, Jiangping Hu, and B. Andrei Bernevig. Exotic d-wave superconducting state of strongly hole-doped $\mathbf{k}_x\mathrm{ba}_{1-x}\mathrm{fe}_2\mathrm{as}_2$. *Phys. Rev. Lett.*, 107:117001, Sep 2011.

[35] S. Maiti, M. M. Korshunov, T. A. Maier, P. J. Hirschfeld, and A. V. Chubukov. Evolution of symmetry and structure of the gap in iron-based superconductors with doping and interactions. *Phys. Rev. B*, 84:224505, Dec 2011.

[36] F. Kretzschmar, B. Muschler, T. Böhm, A. Baum, R. Hackl, Hai-Hu Wen, V. Tsurkan, J. Deisenhofer, and A. Loidl. Raman-scattering detection of nearly degenerate s-wave and

d-wave pairing channels in iron-based $ba_{0.6}k_{0.4}fe_2as_2$ and $rb_{0.8}fe_{1.6}se_2$ superconductors. *Phys. Rev. Lett.*, 110:187002, May 2013.

[37] T. Böhm, A. F. Kemper, B. Moritz, F. Kretzschmar, B. Muschler, H.-M. Eiter, R. Hackl, T. P. Devereaux, D. J. Scalapino, and Hai-Hu Wen. Balancing act: Evidence for a strong subdominant *d*-wave pairing channel in $ba_{0.6}k_{0.4}fe_2as_2$. *Phys. Rev. X*, 4:041046, Dec 2014.

[38] Thomas Böhm, Florian Kretzschmar, Andreas Baum, Michael Rehm, Daniel Jost, Ramez Hosseinian Ahangharnejhad, Ronny Thomale, Christian Platt, Thomas A Maier, Werner Hanke, Brian Moritz, Thomas P Devereaux, Douglas J Scalapino, Saurabh Maiti, Peter J Hirschfeld, Peter Adelmann, Thomas Wolf, Hai-Hu Wen, and Rudi Hackl. Microscopic origin of Cooper pairing in the iron-based superconductor Ba1xKxFe2As2. *npj Quantum Materials*, 3(1):48, 2018.

[39] K. Okazaki, Y. Ota, Y. Kotani, W. Malaeb, Y. Ishida, T. Shimojima, T. Kiss, S. Watanabe, C.-T. Chen, K. Kihou, C. H. Lee, A. Iyo, H. Eisaki, T. Saito, H. Fukazawa, Y. Kohori, K. Hashimoto, T. Shibauchi, Y. Matsuda, H. Ikeda, H. Miyahara, R. Arita, A. Chainani, and S. Shin. Octet-line node structure of superconducting order parameter in kfe2as2. *Science*, 337(6100):1314–1317, 2012.

[40] Y. Ota, K. Okazaki, Y. Kotani, T. Shimojima, W. Malaeb, S. Watanabe, C.-T. Chen, K. Kihou, C. H. Lee, A. Iyo, H. Eisaki, T. Saito, H. Fukazawa, Y. Kohori, and S. Shin. Evidence for excluding the possibility of *d*-wave superconducting-gap symmetry in ba-doped kfe_2as_2. *Phys. Rev. B*, 89:081103, Feb 2014.

[41] Lei Shan, Yong Lei Wang, Bing Shen, Bin Zeng, Yan Huang, Ang Li, Da Wang, Huan Yang, Cong Ren, Qiang Hua Wang, Shuheng H. Pan, and Hai Hu Wen. Observation of ordered vortices with Andreev bound states in Ba0.6K0.4Fe2As2. *Nature Physics*, 7(4):325–331, apr 2011.

CHAPTER 4. LONDON PENETRATION DEPTH AND ELECTRON IRRADIATION IN $CaK(Fe_{1-x}Ni_x)_4As_4$

Modified from manuscripts published in

Physical Review B 95, 100502(R) (2017)

Kyuil Cho,[1] A. Fente,[2] S. Teknowijoyo,[1] M. A. Tanatar,[1] K. R. Joshi,[1] N. M. Nusran,[1] T. Kong,[1] W. R. Meier,[1] U. Kaluarachchi,[1] I. Guillamón,[2] H. Suderow,[2] S. L. Bud'ko,[1] P. C. Canfield,[1] R. Prozorov[1]

and **Physical Review B 97, 140508(R) (2018)**

S. Teknowijoyo,[1] K.Cho,[1] M. Kończykowski,[3] E. I. Timmons,[1] M. A. Tanatar,[1] W. R. Meier,[1] M. Xu,[1] S. L. Bud'ko,[1] P. C. Canfield,[1] R. Prozorov[1]

[1] Ames Laboratory and Department of Physics and Astronomy, Iowa State University, Ames, IA 50011 USA

[2] Laboratorio de Bajas Temperaturas, Unidad Asociada UAM CSIC, Departamento de Física de la Materia Condensada, Instituto Nicolás Cabrera and Condensed Matter Physics Center (IFIMAC), Universidad Autónoma de Madrid, E-28049 Madrid, Spain

[3] Laboratoire des Solides Irradiés, École Polytechnique, CNRS, CEA, Université Paris-Saclay, 91128 Palaiseau Cedex, France

4.1 Combined Abstract

Measurements of the London penetration depth $\Delta\lambda(T)$ and tunneling conductance in single crystals of the recently discovered stoichiometric iron-based superconductor $CaKFe_4As_4$ (CaK1144)

show nodeless, two-effective-gap superconductivity with a larger gap of about 6-10 meV and a smaller gap of about 1-4 meV. Having a critical temperature $T_{c,onset} \approx 35.8$ K, this material behaves similar to slightly overdoped $(Ba_{1-x}K_x)Fe_2As_2$ (e.g., $x = 0.54$, $T_c \approx 34$ K), a known multi-gap $s_\pm$ superconductor. We conclude that the superconducting behavior of stoichiometric CaK1144 demonstrates that two-gap $s_\pm$ superconductivity is an essential property of high-temperature superconductivity in iron-based superconductors, independent of the degree of substitutional disorder.

Controlled pointlike disorder introduced by 2.5-MeV electron irradiationwas used to probe the superconducting state of single crystals of $CaK(Fe_{1-x}Ni_x)_4As_4$ superconductor at $x = 0$ and 0.05 doping levels. Both compositions show an increase of the residual resistivity and a decrease of the superconducting transition temperature, T_c, at the rate of $dT_c/d\rho(T_c) \approx 0.19$ K/($\mu\Omega$cm) for $x = 0$ and 0.38 K/($\mu\Omega$cm) for $x = 0.05$, respectively. In the Ni-doped compound ($x = 0.05$), the coexisting spin-vortex crystal (SVC) magnetic phase is suppressed at the rate of $dT_N/d\rho(T_N) \approx 0.16$ K/($\mu\Omega$cm). The low-temperature variation of London penetration depth is well approximated by the power-law function, $\Delta\lambda(T) = AT^n$, with $n \approx 2.5$ for $x = 0$ and $n \approx 1.9$ for $x = 0.05$ in the pristine state. Detailed analysis of $\lambda(T)$ and T_c evolution with disorder is consistent with two effective nodeless energy gaps in the density of states due to robust $s_\pm$ pairing. Overall the behavior of $CaK(Fe_{1-x}Ni_x)_4As_4$ at $x = 0$ is similar to a slightly overdoped $Ba_{1y}K_yFe_2As_2$ at $y \approx 0.5$, and at $x = 0.05$ to an underdoped composition at $y \approx 0.2$.

4.2 Introduction

$CaKFe_4As_4$ (CaK1144) along with the rest of the 1144 family were discovered in 2016 by Iyo *et al.* which garnered significant attention in the community as a new series in the realm of iron-based superconductors [1]. The interest in the material was boosted by its relatively high superconducting transition temperatures ($T_c = 31 - 36$ K) which are not very far from the highest T_c among the known iron-based superconductors ($T_c = 39$ K in optimally-doped K-Ba122). As a new material, it is important to compare the new 1144 compound to a more established member of the iron-based superconductor to get a proper perspective. In this case the 122 family became the first

choice. Although it is stoichiometrically distinct from the 122 family, the 1144 system shares many properties with the 122 since the point of its discovery. To grow the 1144 polycrystalline compounds Iyo *et al.* substituted alkali metal (A = Na, K, Rb, Cs) into a regular 122 system AeFe$_2$As$_2$ (Ae = Ca, Sr, Ba). However, they find that depending on the difference in their ionic radii, the alkali atoms may either randomly occupy the alkali-earth sites (preserving the 122 structure) or form a separate layer by occupying inequivalent crystallographic sites thus creating an alternate stacking of Ae and A layers (the new 1144 structure, see Fig. 4.1(a)). The former case yields doped $I4/mmm$ space group of the 122 structure while the latter has $P4/mmm$ space group of the 1144 structure (Fig. 4.1(c)). To create the 1144 structure, there are restrictions on the difference in the ionic radii and a-axis lattice parameters of Ae122 and A122 which were found empirically. Fig. 4.1(b) shows the relationship between Δr ($= r^{A} - r^{Ae}$) and Δa ($= a^{A122} - a^{Ae122}$) for the Ae and A pairs in the figure. The solid squares and circles are the pairs that form the 1144 and the 122 phases, respectively. Therefore, a small Δa along with a large Δr are necessary for the formation of the 1144 phases. The exception seems to be BaCs pair (denoted as triangle in the graph) which is located at the boundary between the 1144 and 122 phases. Since it is sitting at the boundary, there is competition between the two phases to be the ground state of the material which is reflected in the inconclusive x-ray diffraction result of its crystal structure.

4.2.1 CaKFe$_4$As$_4$ single crystals

Iyo *et al.* discovered and studied the 1144 compound in polycrystalline form. However, single crystalline samples are needed if one wants to measure transport and thermodynamic anisotropies, study single crystal diffractions and so on. In the latter part of 2016 Meier and Kong *et al.* have successfully grown single crystals of CaKFe$_4$As$_4$, one of the members in the 1144 family [2]. The details of the necessary conditions and growth parameters for the quarternary flux melt method are described elsewhere [2, 3]. At first glance CaKFe$_4$As$_4$ has the same electron count as Ca$_{0.5}$K$_{0.5}$Fe$_2$As$_2$ and Ba$_{0.5}$K$_{0.5}$Fe$_2$As$_2$. Indeed, electrical transport [1, 2, 3, 4], magneto-optical imaging [2], heat capacity [1, 2], ARPES [5], STM [6], NMR [7], Mossbauer spectra [8], pressure

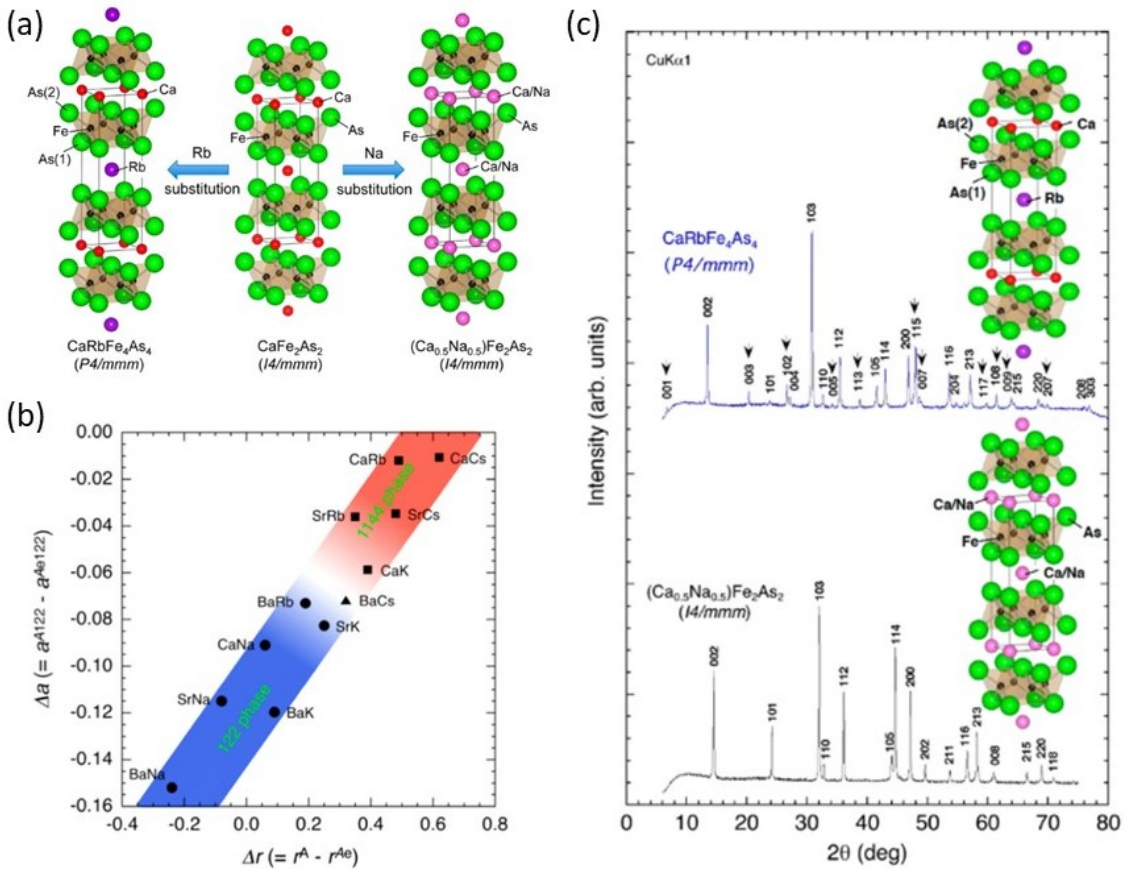

Figure 4.1 (a) Crystal structures of $AeA\mathrm{Fe_4As_4}$ (left), undoped $Ae\mathrm{Fe_2As_2}$ (center) and $(Ae_{1-x}A_x)\mathrm{Fe_2As_2}$ (right). When the conditions are fulfilled, Ae and A metals occupy distinct crystallographic sites, resulting in a different stacked structure ($P4/mmm$, left) compared to the parent compound ($I4/mmm$, center). (b) The parameters Δa and Δr which determine whether the Ae and$A$ pairs will form the stoichiometric 1144 (squares, red region) or doped 122 (circles, blue region) structures. Triangle denotes BaCs, which sits between the two phases, whose structural type is unknown. (c) Powder x-ray diffraction pattern of $\mathrm{CaRbFe_4As_4}$, together with that of $(\mathrm{Ca_{0.5}Na_{0.5}})\mathrm{Fe_2As_2}$ for comparison. $I4/mmm$ structure only allows even values of $h+k+l$ whereas the $P4/mmm$ structure allows both even and odd peaks. From Ref. [1].

studies [9, 10], band structure [11] and DFT calculations [5, 10, 12] have all pointed the overall resemblance to the 122 family. Gap structure studies are consistent with a multiband character with $s_{\pm}$ pairing aided by spin fluctuations [4, 13, 14, 15]. Moreover, CaK1144 and slightly overdoped K-Ba122 have similar T_c's ($\approx$ 35 K). They also feature the absence of structural and magnetic ordered phase above T_c. Despite all the similarities, it is important to point out that $CaKFe_4As_4$ is stoichiometric which means that the material is less disordered compared to the doped 122's. This provides a unique opportunity to study a relatively high transition temperature of an iron-based superconductivity in a highly ordered compound [2, 11]. Indeed, the residual resistivity ratio (RRR $\equiv R(300\text{ K})/R(40\text{ K})$) yields values of ≈ 15 for CaK1144 (Fig. 4.2(d)) as compared to ≈ 7 for the optimally doped K-Ba122 single crystals [4]. Several examples of basic characterizations of CaK1144 single crystals are shown in Fig. 4.2 [2]. All temperature-dependent probes show a clean, bulk superconductivity with $T_c = 35$ K. Resistivity measurements above T_c reveal small anisotropy below 150 K with smooth curves up to 300 K, consistent with the absence of other competing states in this compound (Fig. 4.2(d)). The obtained key parameters of $CaKFe_4As_4$ include the anisotropy parameter $\gamma(T) = H_{c2}^{\perp}/H_{c2}^{\parallel} \simeq 2.5$ (at T_c) and $\simeq 1.5$ (at 25 K), Ginzburg-Landau coherence lengths $\xi_{GL}^{\parallel} \simeq 58$ nm and $\xi_{GL}^{\perp} \simeq 143$ nm [2], upper critical fields $H_{c2}^{\parallel}(0) \simeq 71$ kOe and $H_{c2}^{\perp}(0) \simeq 92$ kOe (by extrapolation) [1, 2], London penetration depth $\lambda(0)^{\perp} \approx 133$ nm [4], 141 nm [16], 187 nm [7], 208 nm [15] and critical current density $j_C \sim 10^8$ A/cm^2 [17]. The parallel and perpendicular directions are defined with respect to the crystallographic c-axis. j_C was measured with $H \parallel ab$.

4.2.2 $CaK(Fe_{1-x}Ni_x)_4As_4$ ($x = 0.05$) single crystals

Since the stoichiometric $CaKFe_4As_4$ is found to be very similar to slightly overdoped K-Ba122, it was assumed that long-range magnetism could be induced by increasing the electron count (which is equivalent to reducing the hole doping in K-Ba122). This idea was realized in 2018 by Meier *et al.* by substituting a fraction of Ni or Co at the Fe site [18]. The resulting compounds, $CaK(Fe_{1-x}Ni_x)_4As_4$ ($x = 0.017$ - 0.063) and $CaK(Fe_{1-y}Co_y)_4As_4$ ($y = 0.039$ - 0.124) show magnetic ordering from NMR and Mossbauer spectra analysis, which is also detected in resistivity measurements. The phase

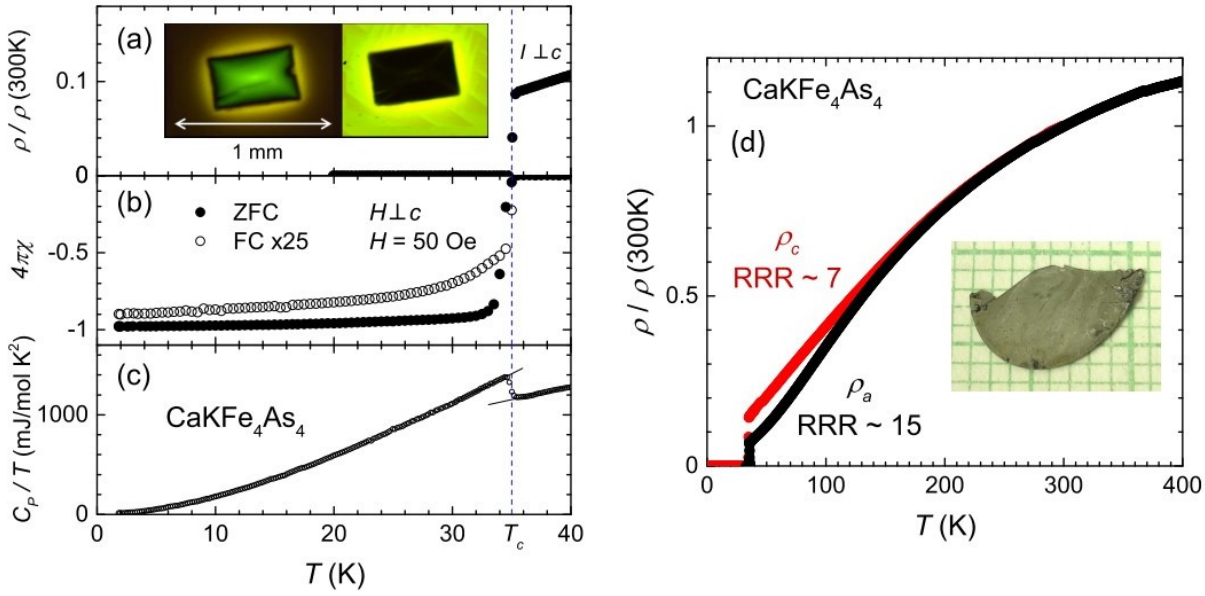

Figure 4.2 Thermodynamic and transport data of $CaKFe_4As_4$ near T_c. (a) The normalized electrical resistivity, inset shows the magneto-optic image on a $CaKFe_4As_4$ single crystal. (b) FC and ZFC magnetization for $H = 50$ Oe for H applied perpendicular to the crystallographic c-axis. ZFC curve shows full volume screening from the interior. (c) The zero-field specific heat $C_p(T)/T$. (d) Full temperature range of in-plane, ($\rho_a(T)$, and interplane, ($\rho_c(T)$), resistivity of $CaKFe_4As_4$, plotted using normalized resistivity scales, $\rho(T)/\rho(300\text{ K})$. At 300 K, $\rho_a \sim 300\ \mu\Omega$ cm, and $\rho_c \sim 1000 - 2000\ \mu\Omega$ cm. Inset shows picture of a $CaKFe_4As_4$ single crystal over a millimeter grid. From Ref. [2].

diagram is shown in Fig. 4.3(g). Since Ni contributes twice as many electrons per atom as Co, the authors were able to plot the data for both Ni- and Co-doped compounds to fall on top of each other by scaling the composition axis of the phase diagram by two. The solid lines mark the expected superconducting and magnetic phase boundaries. The magnetism in doped CaK1144 is identified as the "hedgehog" spin vortex crystal (SVC) structure, in contrast to the stripe spin density wave in the 122 system [18]. Fig. 4.3(a)-(d) show the different spin motifs associated with the magnetic propagation vectors $\mathbf{Q_i}$ in iron-based superconductors. Thus far, only doped CaK1144 has been confirmed experimentally to feature the SVC magnetic order. However it may also be the favorable magnetic ground state in other 1144 series, as predicted by a theoretical study by Borisov *et al.* [10].

A hand-waving argument may explain why the SVC magnetic structure is more favorable in the 1144 compound. SSDW-type AFM breaks the the tetragonal symmetry of the magnetic lattice, similar to orthorhombic structure that breaks the tetragonal symmetry of the crystal lattice. Therefore, a crystallographic structure may favor SSDW (SVC) if its symmetry is orthorhombic (tetragonal). In Ni-CaK1144, X-ray diffraction peaks above and below the AFM transition show no indication of lattice distortion or superlattice geometry [18]. In other words, there is no structural phase transition from tetragonal to orthorhombic symmetry breaking, unlike the 122 system. Therefore, the tetragonal symmetry is preserved which makes the SVC structure more favorable.

4.3 Measurements on Pristine $CaKFe_4As_4$

Since $CaKFe_4As_4$ is similar to slightly overdoped K-Ba122 in many respects, it was predicted in the beginning that the gap structure is also multiband with a relative sign change ($s_\pm$ pairing). Indeed, studies on heat capacity [2], ARPES [5], NMR [7], inelastic neutron scattering [14] and muon spin rotation [15], observed several bands with full, nodeless gaps consistent with the prediction. In the beginning of 2017, our group reported a study on the gap structure of $CaKFe_4As_4$ [4], by measuring the London penetration depth using the TDR method (see Ch. 1, 2). Since London penetration depth is a direct probe of the gap structure, our result highly complements other

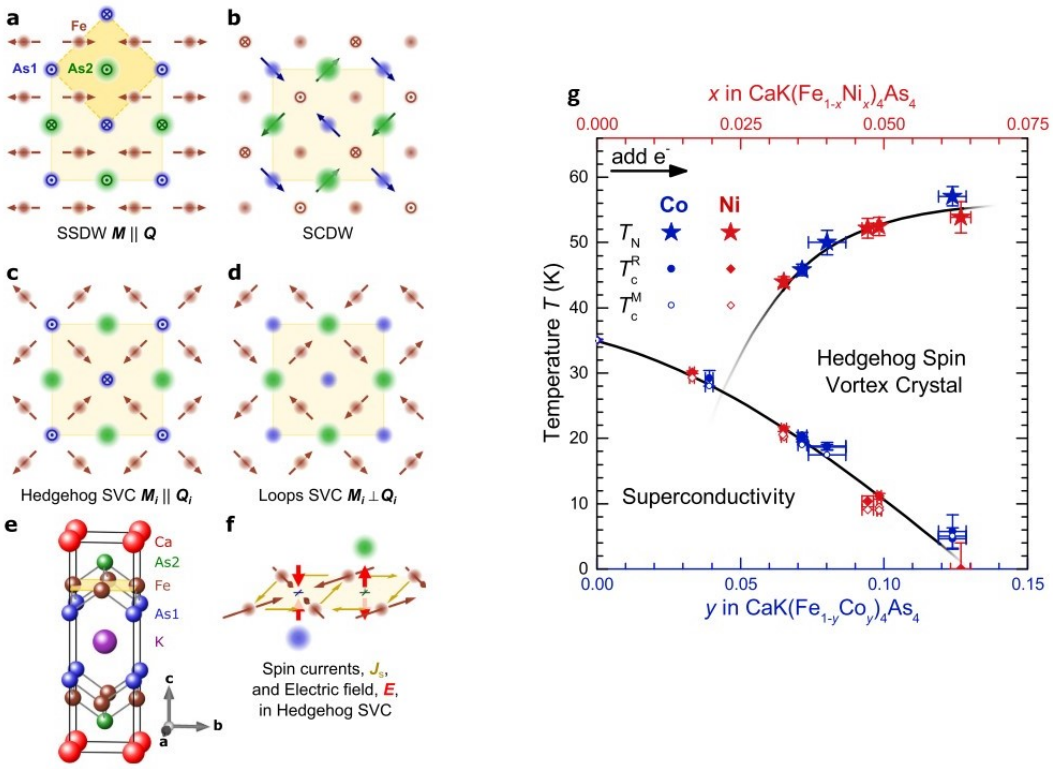

Figure 4.3 Schematics of possible magnetic order types in $CaKFe_4As_4$. (a)-(d) Sketches of four magnetic moment patterns on an FeAs layer in the $CaKFe_4As_4$ structure associated with $\mathbf{Q_i} = (\pi, 0)$ and $\mathbf{Q_2} = (0, \pi)$ magnetic propagation vectors. The upper yellow square in (a), (e) represents the projection of the $CaKFe_4As_4$ unit cell. The magnetic unit cells are represented by the central yellow squares in (a)-(d). The brown arrows represent the magnetic moments at the Fe sites and the blue and green arrows the hyperfine field ($H_{\rm hf}$) at the inequivalent As1 and As2 sites. (a) Orthorhombic stripe spin density wave (SSDW), (b) spin charge density wave (SCDW), (c) hedgehog spin vortex lattice (SVC) and (d) loops spin vortex lattice. (e) The chemical structure of $CaKFe_4As_4$, with the inequivalent As1 and As2 adjacent to K and Ca planes, respectively. (f) Section of the FeAs sheet with a hedgehog SVC moment arrangement. Spin up currents between the iron atoms, J_s (yellow arrows), generate an electric field, $\mathbf{E}$ (red arrows), which couples to asymmetric shifts of the two arsenic sites. Unlike in $CaFe_2As_2$ structure, an asymmetric arrangement of As atoms is imposed by the crystallographic symmetry in $CaKFe_4As_4$ providing a symmetry-breaking field that favors the SVC-type phases. (g) Common phase diagram of Co-doped and Ni-doped $CaKFe_4As_4$. Doping $CaKFe_4As_4$ with either Co or Ni suppresses the superconducting transition temperature, and stabilizes a hedgehog SVC below T_N. T_c^R and T_c^M were determined by resistance and magnetization measurements, respectively. The Ni-concentration on the upper axis, x is scaled by a factor of two with respect to the Co-concentration, y, which maps the transition temperature of the two series onto each other, consistent with their electron contributions. From Ref. [18].

methods in understanding this new superconductor series. The uniqueness of our approach is to combine thermodynamic (London penetration depth), transport (resistivity) and surface sensitive (STM) probes on samples within the same batch. Since these techniques complement each other, we could get a coherent and consistent picture as a result.

4.3.1 London penetration depth measurement

The full temperature range of London penetration depth and resistivity measurements in $CaKFe_4As_4$ are shown in Fig. 4.4(c) and (d). Both show that the single crystals we measured have no secondary phases and feature a sharp superconducting transition. From London penetration depth measurement we can directly compare the low temperature variation ($T/T_c \leq 0.3$) in CaK1144 to other 122 compounds, which are shown in Fig. 4.4(a). The materials in the figure were selected due to their comparable T_c values since the compositions are near or at optimal doping of their respective series. At a glance $CaKFe_4As_4$ looks more similar to $Ba_{0.46}K_{0.54}Fe_2As_2$ than to the other candidates. P-Ba122 series are nodal and therefore they show linear T-dependence at low temperature which is very different to CaK1144. On the other hand, $Ba_{0.65}K_{0.35}Fe_2As_2$ is nodeless so at very low temperatures ($T/T_c \leq 0.05$) it shows similar saturation behavior to CaK1144. However, K-Ba122 with $x = 0.54$ has the most similar (normalized) T-dependence in the range shown here. This is to be expected since they have a similar electron count as explained earlier in the introduction of this chapter.

To make our analysis of the low temperature behavior more quantitative, we can use the usual power-law fitting $\Delta\lambda \propto T^n$ with varying upper limits T_{max}/T_c, as shown in Fig. 4.4(b). As explained in Ch. 1, a nodal gap structure will show linear T behavior with exponent $n \approx 1$ which is the case for P-Ba122 [19] (not shown). For a clean nodeless gap, the fitting will show large exponent ($n \gtrsim 3$) such as shown for $x = 0.35$ K-Ba122. In the case of nodeless $s_\pm$ gap, a small degree of anisotropy and impurity scattering can bring down the exponent closer to two which we know from Ch. 3 is the case for $x = 0.54$. Therefore, the behavior of $CaKFe_4As_4$ is consistent with $s_\pm$ pairing with nodeless gaps.

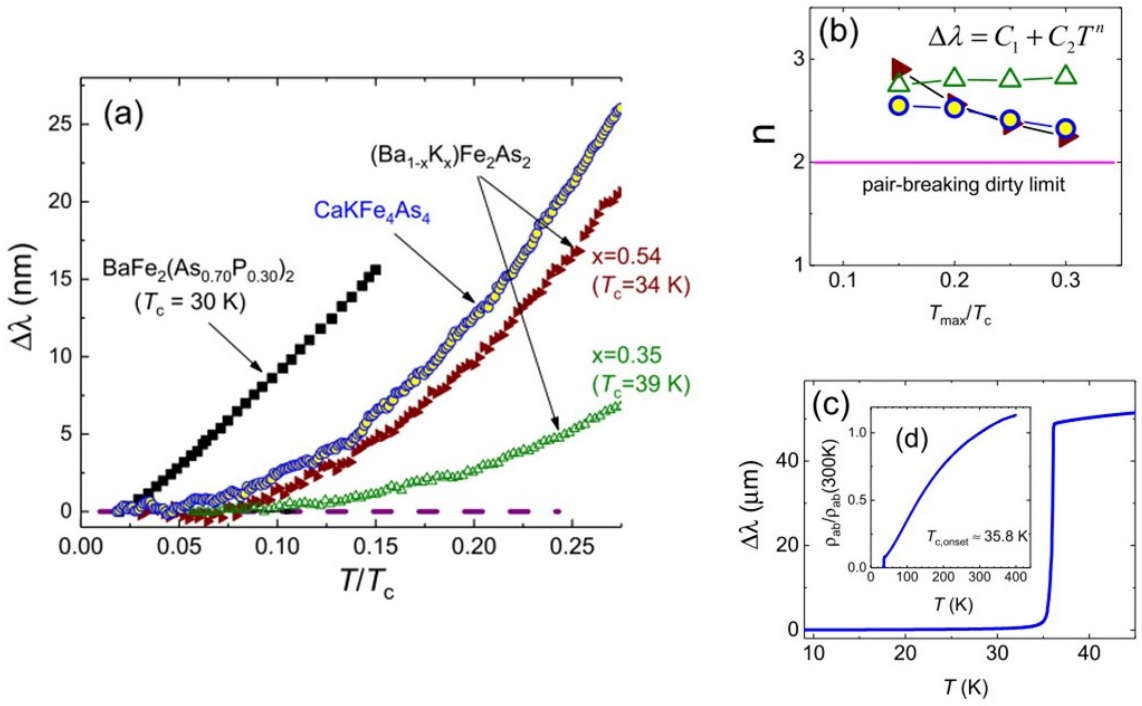

Figure 4.4 (a) The variation of the London penetration depth $\Delta\lambda(T)$ in CaK1144 (solid circles) compared with other iron-based superconductors, $BaFe_2(As_{0.70}P_{0.30})_2$ (nodal gap, $T_c \approx 30$ K, solid squares) [19]), $Ba_{0.65}K_{0.35}Fe_2As_2$ (no nodes, optimally doped, $T_c \approx 39$ K, open triangles) and $Ba_{0.46}K_{0.54}Fe_2As_2$ (no nodes, overdoped, $T_c \approx 34$ K, solid triangles) [20]. (b) Exponent n obtained from the power-law fit $\Delta\lambda = C_1 + C_2T^n$ as a function of the upper fit limit T_{max}/T_c. Pink horizontal line marks $n = 2$, the dirty limit exponent for the sign-changing order parameters such as $d-$wave or $s_{\pm}$. Symbols are the same as in (a). (c) Variation of the in-plane London penetration depth $\Delta\lambda(T)$ showing the full transition. (d) Normalized in-plane resistivity $\rho_{ab}(T)/\rho_{ab}$ (300 K) in full temperature range. From Ref. [4].

4.3.2 Scanning tunneling microscopy measurement

For the STM experiment we collaborated with Antón Fente *et al.* from Hermann Suderow group in Universidad Autónoma de Madrid (Autonomous University of Madrid). In their STM setup a $CaKFe_4As_4$ single crystal from the same batch as the one used for the penetration depth study was mounted onto a sample holder and a piece of brass was glued on top of it. Then the sample holder was moved toward a copper beam, lifting off the glued brass piece and leaving a freshly cleaved surface for the tunneling measurements [21, 22]. The STM data was taken at 0.8 K which corresponds to an energy resolution of about 70 μeV, determining roughly the interval between points in the tunneling conductance curves [21, 23]. The measurements were conducted using a normal metal (gold) tip. The tunneling conductance was obtained by differentiating the $I-V$ curves as described in their previous works [24, 25], which is shown in Fig. 4.5(a). Flat surfaces for tunneling were found using a similar protocol to other STM studies for example, in K-Ba122 [26]. Fente *et al.* measured hundreds of topographical images and millions of spectra and a detailed analysis on vortex study is published separately [6]. Here, they find that in $CaKFe_4As_4$ there is no surface reconstruction which is usually discussed in STM work on other iron-based superconductors [26, 27, 28]. Instead, they observe atomically flat surfaces showing atomic size features that are separated by steps due to terminations of different crystallographic planes.

Fig. 4.5(a) shows a few representative tunneling conductance curves obtained within an area whose topography is shown in the insets. The corresponding $I-V$ curves are shown in Fig. 4.5(b). Close to the Fermi level, there is often a negligible tunneling conductance which indicates no states (i.e. gap). Well-developed quasiparticle peaks are observed at a bias voltage that changes depending on the surface plane. At some surfaces (blue and violet in Fig. 4.5(a)), there is a quasiparticle peak slightly above 10 mV and a kink at about 5 mV. At other surfaces, the quasiparticle peaks happen at about 5 mV and shoulders somewhat below 10 mV (green and red curves). This is a common observation in effective two-gap iron-based superconductors including in a study of K-Ba122 [26]. The response variation is due to different surface terminations (Fig. 4.5(a) insets) that lead to different matrix elements for the tunneling between the tip and the sample [29, 30]. This leads to

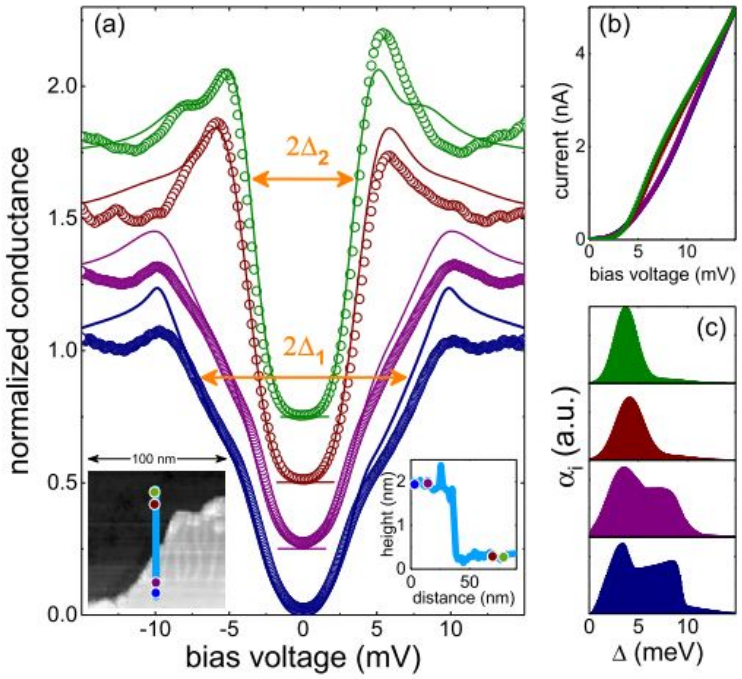

Figure 4.5 (a) Tunneling conductance vs bias voltage curves measured at 800 mK (symbols) and the corresponding fits to BCS theory (solid lines). The curves are shifted vertically, and the zero conductance value is indicated by a horizontal line under each curve. The left inset shows the topography of the surface (image size is 100 x 100 nm^2) and the right inset shows a profile taken along the line shown in the left inset. Points along the line in the left inset provide the places where we took the curves of the main panel. The step shown in the profile of the order of the unit cell c-axis parameter. Orange arrows mark the position of the two maxima in the distributions of Δ_i. (b) Tunneling current vs bias voltage curves corresponding to the tunneling conductance curves shown in (a). Colors of symbols in (a) are used to refer to the corresponding curves in (b) and (c) and points in the inset of (a). From Ref. [4].

spatially varying contributions to the density of states from different parts of the Fermi surface. When the gap is not uniquely defined (as opposed to simple s-wave BCS superconductor with a well-defined gap), the gap sizes involved in the tunneling process differ from the positions of the quasiparticle peaks in the bias voltage. To obtain the tunneling conductance and find the superconducting gap values, Fente *et al.* convoluted a density of states in the form α_i Re$(\frac{E}{\sqrt{E^2-\Delta^2}})$ with the derivative of the Fermi function to obtain the tunneling conductance [23, 29, 31, 32]. The solid lines in Fig. 4.5(a) show the tunneling conductance calculated using the set of α_i and Δ_i shown in Fig. 4.5(c). The values of the superconducting gap are spread between ~ 1 and 10 meV. The α_i provides the relative weight in the tunneling conductance from the different gap values (see, e.g. [31] for similar results obtained in MgB_2). At all locations there are two peaks in the α_i. The height of each peak varies as a function of the tunneling plane. One peak is at ≈ 3 meV and another one at ≈ 8 meV. This corresponds, respectively, to $\Delta_1(0)/T_c = 0.54$ and $\Delta_2(0)/T_c = 1.45$ (orange arrows in Fig. 4.5(a)). These values can be compared to $\Delta(0)/T_c = 1.76$ for the isotropic single gap weak-coupling (BCS) value. These values are quite typical for iron-based superconductors [20].

4.4 Measurements on CaK$(Fe_{1-x}Ni_x)_4As_4$ ($x = 0$, 0.05) in Pristine and Irradiated States

Since magnetism and superconductivity are known to have a complex interplay in the coexistence region (e.g. in $y < 0.25$ $Ba_{1-y}K_yFe_2As_2$ [33, 34, 35]) it would be interesting to study the same interplay in the CaK1144 counterpart which has the spin-vortex crystal magnetic structure rather than the stripe type spin-density wave. In this section we investigate the gap structure of CaK$(Fe_{1-x}Ni_x)_4As_4$ ($x = 0, 0.05$) with the $x = 0.05$ composition featuring an SVC magnetic structure [18] using London penetration depth, resistivity and electron irradiation. The details of the experimental methods is described in Ch. 1, 2.

4.4.1 London penetration depth measurements

Fig. 4.6(a) shows the total variation of London penetration depth of $CaK(Fe_{1-x}Ni_x)_4As_4$ over the whole superconducting range from the base temperature (0.4 K) to above superconducting T_c for both stoichiometric ($x = 0$) and Ni-doped ($x = 0.05$) samples. The measurement for $x = 0$ sample was done in a sequence of irradiation and annealing runs whose effects can be seen from the T_c response. From the pristine $T_c^{onset} = 36.1$ K, the first irradiation of dose 2.08 C/cm^2 suppresses T_c by 3.2 K which partially recovers by 1.3 K after 400 K annealing in PPMS. The second and third irradiations of 5.46 C/cm^2 + 4.38 C/cm^2 further suppress the T_c by 9.7 K, to the final value of 24.5 K. The irradiation also increases the skin-depth response in the normal state which turns the $x = 0$ sample from skin-depth limited regime (pristine, red curve in Fig. 4.6(a)) to size-limited (other colors until blue). This is consistent with the increase of residual resistivity measured directly from our resistivity experiment (Fig. 4.7(a)).

The low temperature part of $\Delta\lambda$ for the $x = 0$ sample is shown in (b). The arrow denotes the same sequence of irradiation and annealing treatments as described earlier. From the low temperature data we can extract key parameters of the gap structure in the material. Unlike the response in T_c which reverses upon annealing, the low temperature variation of $\Delta\lambda$ monotonically increases for all treatments. At $T/T_c \leq 0.3$, $\Delta\lambda$ is proportional to the amount of thermally excited quasiparticles [19, 37] which in turn indicates the amount of accessible states. The monotonic increase in $\Delta\lambda(T)$ indicates that a partial fraction of the irradiation-induced defects (mostly Frenkel pairs) remains after the annealing process which contribute to the low energy pair-breaking states. The rest of the defects are annealed away when the Frenkel pairs recombine which causes the partial T_c recovery. Therefore, we find that a real material contains different types of defects and only some of which can be annealed away. This insight can only be seen from a gap structure probe such as London penetration depth measurement as T_c by itself is an imperfect indicator for the impurity scattering in the gap structure. The second parameter is the exponent n extracted from power-law fitting $\Delta\lambda(T) \propto T^n$ with upper limit $T_{max}/T_c = 0.2$ (shown as solid line in the pristine curve as an example). n also shows monotonic decrease from pristine value of $n \approx 2.5$ to $n \approx 2.0$

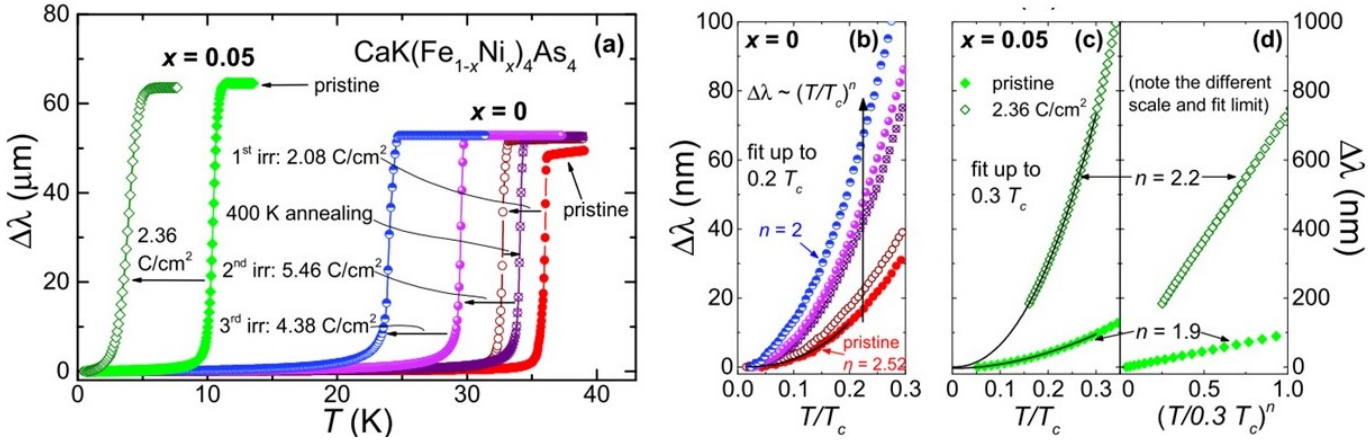

Figure 4.6 (a) Variation of London penetration depth $\Delta\lambda(T)$ showing full superconducting transitions. For the stoichiometric ($x = 0$) sample, the data were taken in a sequence of irradiation/annealing treatments as indicated in the legend. (b) Low-temperature part of $\Delta\lambda$ for $T/T_c \leq 0.3$ in the $x = 0$ sample. The choice of symbols and colors are the same as (a). The exponent n monotonically decreases with irradiation and annealing treatments of the same sequence as (a), which is also indicated by the arrow. The two right most panels show $\Delta\lambda$ in the Ni-doped sample ($x = 0.05$) plotted as a function of T/T_c (c), and of $(T/T_c)^n$ (d). From Ref. [36].

which indicates increasing in-gap impurity scattering but they remain nodeless even after heavy dose of irradiation. This observation is consistent with the effective two-band nodeless $s_{\pm}$ model proposed in Section 4.3.

Fig. 4.6(c) shows a much higher penetration of magnetic field in the pristine Ni-doped CaK1144 compared to the $x = 0$ sample, which could be due to higher level of inherent disorder in a substituted compound. Electron irradiation of moderate dose 2.36 C/cm^2 significantly increases $\Delta\lambda(T)$ even higher indicating that disorder is a more efficient pair breaker in the Ni-doped sample. A similar behavior is observed in K-Ba122 where the underdoped region is also more sensitive to disorder compared to the optimal doping composition [20]. Application of power-law fit (solid lines) yields exponents $n = 1.9$ (pristine) and $n = 2.2$ (2.36 C/cm^2 dose). By plotting $\Delta\lambda(T)$ vs $A\ T^n$ we verify the quality of the fit. The prefactor A (which gives the slope) is notably increased after irradiation reflecting increased quasiparticle density [19]. The slight increase from $n = 1.9$ to 2.2 suggests that in the pristine state, the $x = 0.05$ sample is not yet in the regime where impurity scattering dominates (dirty limit) in which case the exponent saturates without crossing $n = 2$ with further increasing disorder. Rather, in light of previous study in underdoped K-Ba122 in which long-range magnetism gives rise to gap anisotropy [34, 38], the increase of n is consistent with the averaging of an originally anisotropic gap causing the gap to become more isotropic and the gap minima to be elevated. An alternative explanation could invoke the c-axis point node [37] suggested for electron-doped Co-Ba122 from anisotropic thermal conductivity [39, 40] and c-axis penetration depth [41] measurements.

4.4.2 Resistivity measurements

Fig. 4.7 shows the in-plane resistivity of the parent $CaKFe_4As_4$ (a) and 5% Ni-doped CaK1144 (b) compounds. Solid (dashed) line denotes the data taken in the pristine (irradiated) states. The irradiation doses are 2.08 C/cm^2 ($x = 0$) and 2.36 C/cm^2 ($x = 0.05$). The in-plane resistivity of the $x = 0$ sample in pristine state shows a crossover feature at about 200 K which is typical for all hole-doped 122 compositions. Approaching T_c on cooling, $\rho(T)$ shows a small upward curvature

similar to slightly overdoped K-Ba122 where it can be fitted with $\sim T^{3/2}$ dependence in a limited temperature range from 40 K to 60 K [42]. A similar power law fits the data well in $CaKFe_4As_4$ as shown in Fig. 4.7(a) as cyan line. The resistivity just above the onset of resistive transition is about 12 times lower than $\rho(300K)$. The actual residual resistivity is impossible to extrapolate convincingly since $T^{3/2}$ fit gives a small negative value of $\rho(0)$ and T_c is large. The resistive transition to the superconducting state at $T_c(\text{onset}) = 35.2$ K is very sharp (see inset) with a width of $\Delta T_c < 0.5$ K, reflecting good sample quality. Electron irradiation of 2.08 C/cm^2 leads to a vertical shift of the $\rho(T)$ curve with the red line in Fig. 4.7(a) showing the difference between $\rho(T)$ curves before and after irradiation. The shift is not constant throughout suggesting a violation of the Matthiessen rule, which dictates a T-independent offset due to added impurities. In this case, the shift near T_c is about two times higher than at room temperature. Note as well that the superconducting transition remains sharp after the irradiation supporting homogeneous defect distribution.

The electrical resistivity $\rho(T)$ of the Ni-doped sample ($x = 0.05$) in the pristine condition is shown by a solid curve in Fig. 4.7(b). It has a similar broad crossover feature at 200 K, although it is much less pronounced due to a significant increase of residual resistivity compared to the pure $x = 0$ compound (≈ 90 $\mu\Omega$cm, lower inset). An additional feature in the $\rho(T)$ curves of the Ni-doped sample can be distinguished in the temperature-dependent resistivity derivative at ~ 50 K (top inset) which is associated with the magnetic transition (spin-vortex crystal phase [18]). Electron irradiation with a total dose of 2.38 C/cm^2 (dashed curve in Fig. 4.7(b)) leads to an upward shift of the $\rho(T)$. Similar to the pure sample, the shift is temperature dependent and is significantly bigger for $T < T_N \sim 47$ K suggesting partial loss of the carrier density due to magnetism. The magnetic transition temperature is suppressed from 50.6 K to 47.5 K while the (onset of) superconducting transition temperature is suppressed from 10.5 K to 4 K.

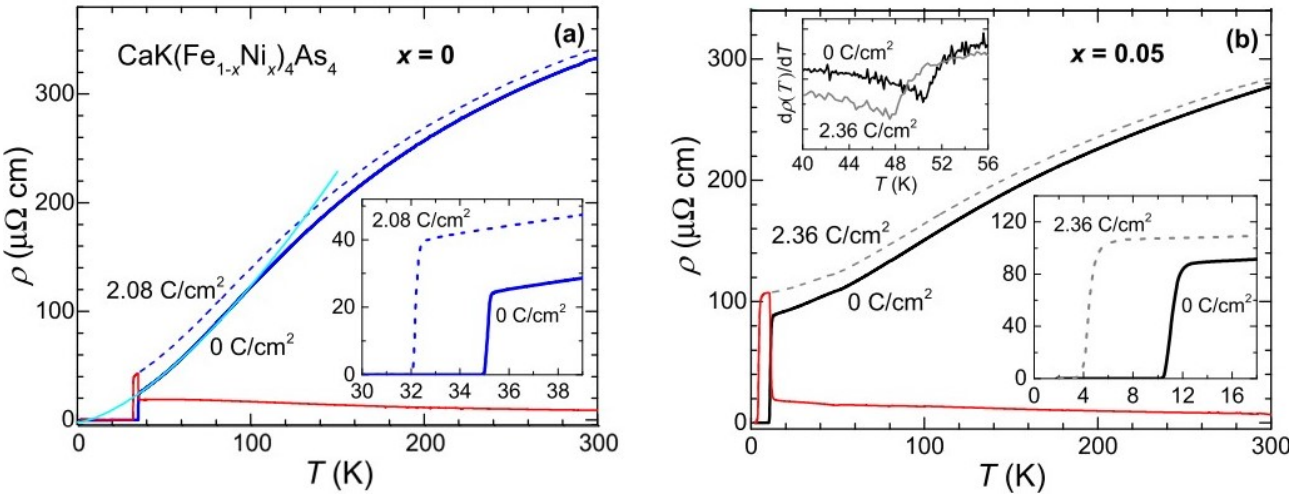

Figure 4.7 In-plane resistivity of (a) the stoichiometric sample ($x = 0$) and (b) Ni-doped sample ($x = 0.05$). Solid and dashed lines show resistivity of the samples before and after irradiation, with doses 2.08 C/cm^2 for $x = 0$, and 2.36 C/cm^2 for $x = 0.05$. Red lines show the difference of resistivity between irradiated and pristine states. The cyan line in (a) is the fit of the curve in the pristine $x = 0$ sample to $\rho(0) + \rho_T T^{3/2}$. The right inset of each panel zooms on the superconducting transition range. The left inset in (b) shows the temperature-dependent resistivity derivative zooming on the features at T_N, suppressed upon irradiation from 50.6 K to 47.5 K. From Ref. [36].

4.5 Discussion and Analysis

To get a sense of the gap size in $CaKFe_4As_4$ the low-temperature BCS asymptotic behavior can be used to fit the temperature variation of London penetration depth data, $\Delta\lambda = B_1 + B_2\sqrt{\pi\delta/2t}\,\exp(-\delta/t)$ where $t \equiv T/T_c$ and B_1, B_2 and $\delta \equiv \Delta(0)/T_c$. The experimental base temperature is taken as the lower limit and the upper limit T_{max}/T_c is varied between $\approx 0.11-0.18$. The reduced χ value $\chi^2 = \Sigma(f_{\rm data} - f_{\rm fit})^2/{\rm DOF}$ indicates the quality of the fitting procedure (lower inset of Fig. 4.8(a)) which shows reasonable quality and saturates for upper limits $T_{max}/T_c \leq 0.14$. DOF is the number of degrees of freedom defined as the number of data points minus the number of free parameters. The upper inset shows that the gap parameter δ also converges to the value of $\delta \approx 0.32$ (≈ 1 meV) using the same upper limits $T_{max}/T_c \leq 0.14$. The main panel of Fig. 4.8(a) shows an example of actual fitting of the BCS curve with $T_{max}/T_c = 0.14$. Overall, the BCS fitting correctly captures the saturation behavior at low temperature which indicates a gap in the density of states. However, this approach has two caveats: (i) the value of extracted gap generally differs from the magnitude of the order parameter due to scattering [43] and (ii) it fails to take into account the multiband nature of the material.

To get a better estimate of the gap magnitudes in a multiband context we use the two-band γ-model to fit the normalized superfluid density $\rho_s \equiv (\lambda(0))/\lambda(T))^2$ [44]. But first we need to obtain $\lambda(0)$ to calculate the superfluid density from another method since in general, the TDR technique is suitable for precision measurements of the changes in the penetration depth but not the absolute value [45]. Here, we use two approaches to estimate $\lambda(0)$. First, we use the thermodynamic Rutgers relation [46] to estimate the Ginzburg-Landau parameter $\kappa_{\rm GL} = \lambda_{\rm GL}/\xi_{\rm GL}$ [2]

$$\kappa_{\rm GL} = \sqrt{\frac{T_c}{8\pi\Delta C}}\,\frac{\partial H_{c2,c}}{\partial T}\bigg|_{T_c} \tag{4.1}$$

where ΔC is the jump of the specific heat in erg/cm^3/K (using a molar volume of 115.4 cm^3/mol). The slope of the upper critical field ($H \parallel$ the crystallographic c-axis direction) at T_c, $dH_{c2,c}/dT = -4.4$ x 10^4 Oe/K [2]. With these experimentally determined values reported in [2] Eq. 4.1 gives $\kappa_{\rm GL} \approx 60$. Since CaK1144 falls in the clean limit with a short coherence length ($\xi(0) = 2.15$ nm [2])

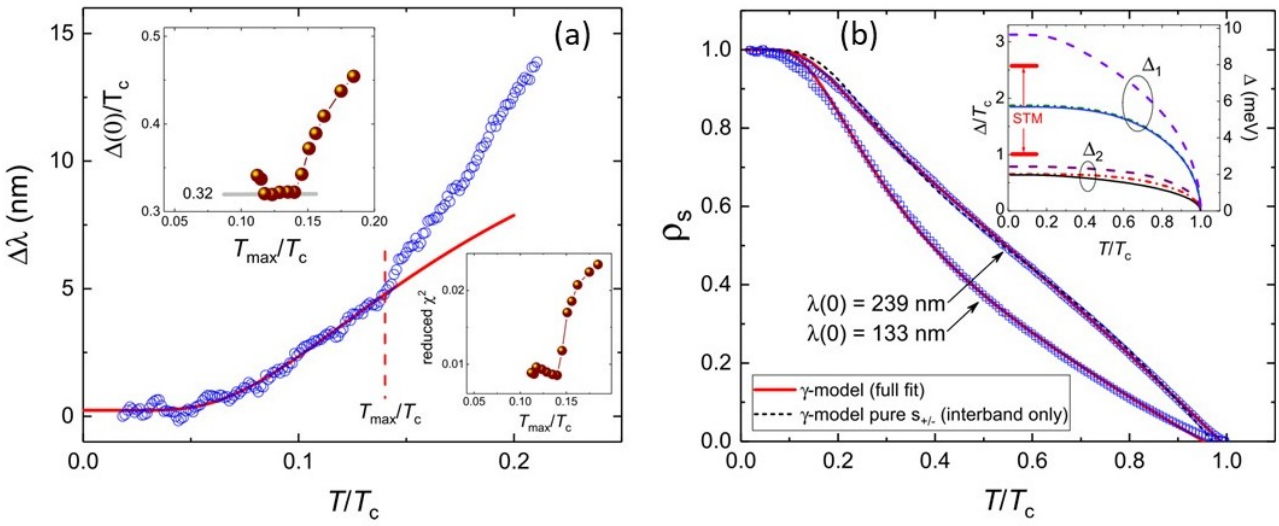

Figure 4.8 (a) A representative BCS fitting with Δ/T_c as a free fit parameter and fixed $T_{\max}/T_c = 0.14$. Upper inset: Δ/T_c obtained from BCS fittings with different $T_{\max}/T_c$. Lower inset: reduced χ^2 vs $T_{\max}/T_c$ corresponding the fitting results shown in the upper inset. (b) Normalized superfluid density ρ_s calculated with $\lambda^{\rm avg}_{\rm thermo}(0) = 133$ nm (open squares) and $\lambda^{\rm B}_{\rm NV}(0) = 239$ nm (open circles) [in-group communication]. Self-consistent γ-model fits with all coupling parameters shown as solid lines and the interband-only coupling fit is shown by the dashed line (for the $\lambda^{\rm B}_{\rm NV}(0) = 239$ nm case). The inset shows the temperature dependence of the two order parameters obtained from the fits in the main figure. Solid and dashed-dotted lines are for the all-parameter fits for two values of $\lambda(0)$, respectively. The dashed lines are for the interband-only fit. The thick red lines mark the spread of the order parameter values determined from the STM measurements. From Ref. [4].

we can use the clean limit relation $\kappa(0) = 1.206\ \kappa_{GL} = 68.7$ from which we determine $\lambda^1_{thermo}(0) = \xi(0)\kappa(0) \approx 148$ nm. As an alternative (but still using thermodynamic relations) we can use $\xi_{GL} \approx 1.5$ nm [2] so $\lambda_{GL} = \xi_{GL}\kappa_{GL} \approx 83$ nm. Therefore, $\lambda^2_{thermo}(0) = \sqrt{2}\ \lambda_{GL} \approx 118$ nm. These are quite close values resulting in a small variation of ρ_s at intermediate temperatures. For the fitting analysis of the superfluid density we use the average of the two values, $\lambda^{avg}_{thermo}(0) = 133$ nm.

The second determination involves a direct measurement of the field of the first vortex penetration on the sample edge using a recently developed sensitive and non-invasive optical magnetometry which is based on the nitrogen-vacancy (NV) centers in a diamond film [16]. Using numerical approximations it is possible to convert the measured penetration field (H_p) to the lower critical field (H_{c1}) which in turn is related to the penetration depth according to $H_{c1} = \phi_0\ (\ln \lambda/\xi + 0.5)/(4\pi\lambda^2)$ [47]. $\phi_0 = 2.07$ x 10^{-15} Wb is the flux quantum. One of the numerical approximations was developed by Brandt in 2001 [48] where $H_p \approx H_{c1}\ \tanh\sqrt{\alpha c/a}$ with c, a as the thickness and the lateral dimensions and α is a geometric factor (= 0.36 for a semi-infinite strip and = 0.67 for a disk). Using Brandt's approach we get $\lambda^B_{NV}(0) \approx 239$ nm (labeled B for Brandt). However, this approximation is not very applicable for samples with the shape of a rectangular slab which were used in the NV experiments. An alternative approach for the rectangular slab geometry is to use $H_p = H_{c1}\ (1 + N\chi)$, where N is the effective demagnetization factor and χ is the magnetic susceptibility given by $\chi = \lambda/w\ \tanh(w/\lambda) - 1$ [45]. The challenge now is to define a practical formula for N in a rectangular slab geometry. After our work was published in 2017 [4], more recently Prozorov and Kogan developed another numerical approach using the COMSOL software which solves Maxwell's equations in 3D finite-element analysis [49]. Their work yields a formula for effective demagnetization factor for rectangular slabs with dimensions $2a$ x $2b$ x $2c$ with the magnetic field pointing in the c-direction given by $N^{-1} = 1 + 3c\ (1 + a/b)/4a$. With this approach, we get an estimate of $\lambda^{PK}_{NV}(0) \approx 141$ nm (PK for Prozorov and Kogan) [16] which is consistent and close in value to the estimate derived from the thermodynamic relations.

Fig. 4.8(b) shows the superfluid density (SFD) curves constructed from $\lambda^{\rm avg}_{\rm thermo}(0) = 133$ nm and $\lambda^{\rm B}_{\rm NV}(0) = 239$ nm. Since $\lambda^{\rm PK}_{\rm NV}(0) = 141$ nm is approximately the same as $\lambda^{\rm avg}_{\rm thermo}$, all of the analysis and discussion on the SFD derived from $\lambda^{\rm avg}_{\rm thermo}$ are also applicable to the SFD derived from $\lambda^{\rm PK}_{\rm NV}$.

The superfluid densities (Fig. 4.8(b)) are fitted with two-band γ-model (red lines) to extract the gap magnitudes [44]. The two values of the order parameter are calculated self-consistently at each temperature. The relative contribution γ from one band (and $1-\gamma$ from the other) is another fit parameter to obtain the total superfluid density. We obtain a very good agreement in the entire temperature range with the order parameters shown in in the inset. In the fit with $\lambda^{\rm B}_{\rm NV}(0) = 239$ nm we obtain $\Delta_1(0)/T_c = 1.86$, $\Delta_2(0)/T_c = 0.64$ so that $\Delta_1(0)/\Delta_2(0) = 2.9$, which is almost a factor of two larger than the ratio found for slightly overdoped K-Ba122 [20]. In energy units they are $\Delta_1(0) = 5.70$ meV and $\Delta_2(0) = 1.97$ meV. With $\lambda^{\rm avg}_{\rm thermo}(0) = 133$ nm ($\approx \lambda^{\rm PK}_{\rm NV}(0)$) despite the quite different magnitude, we obtain similar values of $\Delta_1/T_c = 1.88$ and $\Delta_2 = 0.66$ or in energy units $\Delta_1(0) = 5.77$ meV and $\Delta_2(0) = 2.0$ meV. To explore all possibilities we also used the interband only $s_\pm$ model which was used to analyze the H_{c2} data in [2]. The fit is denoted as dashed line in Fig. 4.8(b) for ρ_s obtained from $\lambda^{\rm B}_{\rm NV}(0) = 239$ nm. The result of pure interband $s_\pm$ fitting is quite reasonable although not as good as the full fit. Here, the gap amplitudes are 9.6 meV and 2.4 meV. Finally, these values need to be compared with the ones obtained from the STM experiment. Indeed, as shown in the inset these values are in a good agreement with 8 meV and 3 meV gaps from STM. Since London penetration depth and scanning tunneling microscopy are quite different in nature (μm scale penetration vs nm scale surface), the agreement in the analysis between the two experimental data is quite remarkable. Our findings make a quite convincing case that superconductivity in $CaKFe_4As_4$ can be described with effective two nodeless gaps with ranges of 1-4 meV and 6-10 meV.

We were unable to reproduce the same analysis for the Ni-doped compound, because the $\lambda(0)$ value is not available in the literature. Our group wanted to apply the NV magnetometry method

however, a single crystal of Ni-CaK1144 with a sufficiently high quality (flat and clean) surface and a sharp edge has so far been elusive in the growth batches available to us.

4.6 Summary and Conclusions

During the discussion and analysis presented so far, Ni-CaK1144 ($x = 0, 0.05$) are found to be very similar in many respects to their closest siblings, the K-Ba122. Consistent with other reports [2, 5, 6, 7, 15, 18] pure (Ni-doped) CaK1144 resembles the slightly overdoped (underdoped) K-Ba122. Using our data, we are now in a better position to go beyond a general doping region such as under- or slightly overdoped regions. We will identify the exact compositions of K-Ba122 which have the closest match to the Ni-CaK1144 samples in our study ($x = 0, 0.05$). This will serve as the summary and conclusion of this chapter.

Fig. 4.9(a) shows the T_c suppression vs the increase of residual resistivity upon irradiation for $CaK(Fe_{1-x}Ni_x)_4As_4$ and selected $Ba_{1-y}K_yFe_2As_2$ compounds for comparison. For the $x = 0$ sample the T_c suppression rate (= -0.19 K/$\mu\Omega$ cm) lies very close to the rate of K-Ba122 with $y = 0.54$ [20]. On the other hand, the $x = 0.05$ compound has twice the rate (= -0.38 K($\mu\Omega$ cm) compared to $x = 0$. This is consistent with the previously discussed low temperature behavior which also shows that irradiation is a more efficient pair-breaker in this composition, possibly due to the coexistence with magnetism [33]. It is slightly steeper but comparable to $y = 0.26$ K-Ba122 which lies in the coexistence region [20]. Therefore, we are getting closer in identifying which of the compositions in K-Ba122 that best match the Ni-CaK1144 samples.

Indeed, the projection of $CaK(Fe_{1-x}Ni_x)_4As_4$ into the $Ba_{1-y}K_yFe_2As_2$ system is best shown in Fig 4.9 where the comparison is presented for both compounds by plotting T_c (in (b)) and its sensitivity to disorder (in (c)), as a function of K-doping. In (b), Ni-CaK1144 blends nicely into the K-Ba122 "dome," where the $x = 0$ ($x = 0.05$) is placed at $y = 0.48$ ($y = 0.18$). In (c), the suppression of T_c normalized by irradiation dose and (pristine) T_{c0} serves as an experimental determination of the material's sensitivity to scattering, which allows a comparison between different compounds in the two iron-based superconductor series. In this case, the $x = 0.05$ CaK1144 seems

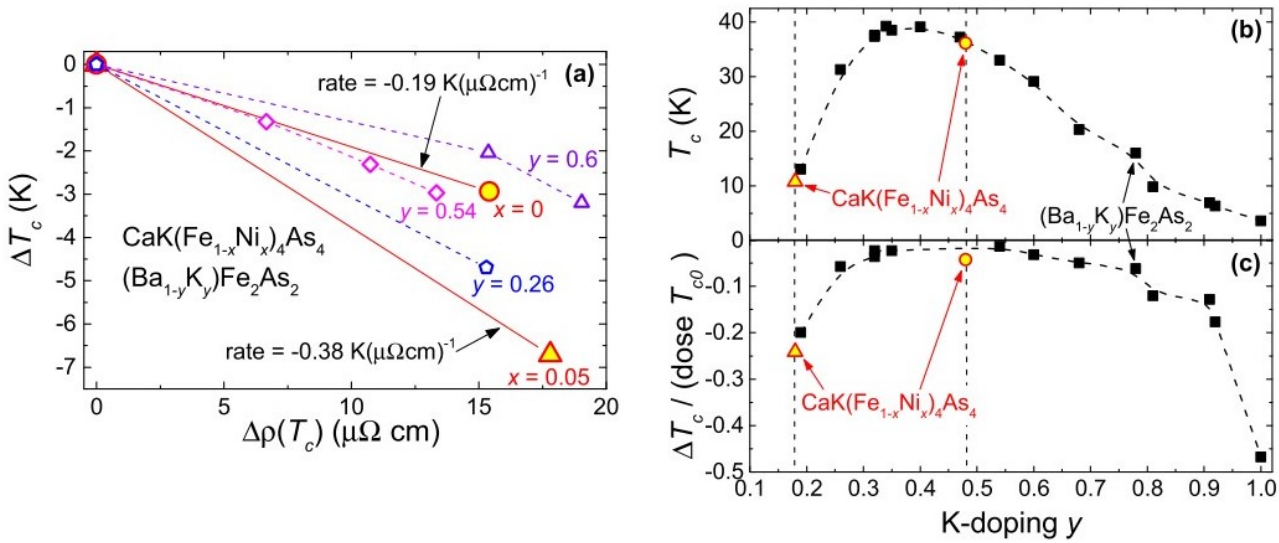

Figure 4.9 (a) The suppression of T_c upon increased disorder which is parametrized via the change in resistivity, $\Delta\rho(T_c)$. The rate of T_c suppression in stoichiometric $CaKFe_4As_4$ ($x = 0$) is similar to near optimally doped $Ba_{1-y}K_yFe_2As_2$ with $y = 0.54$ and 0.6 [20]. The Ni-doped ($x = 0.05$) sample is close to the underdoped $Ba_{1-y}K_yFe_2As_2$ with $y = 0.2$. (b) and (c) Summary figures of T_c suppression normalized by the irradiation dose and T_{c0} as a function of potassium doping y, where $CaKFe_4As_4$ compounds are placed in $y = 0.18$ and 0.48 following the T_c "dome" of $Ba_{1-y}K_yFe_2As_2$. T_c values are taken from Ref. [20, 33]. From Ref. [36].

to follow the K-Ba122 trend while the $x = 0$ lies somewhat below which indicates that it has a higher sensitivity to disorder compared to the K-Ba122 series. These observations are naturally explained by the fact that pristine $x = 0$ CaK1144 starts out cleaner than K-Ba122 ($y \approx 0.5$) so the effect of artificially added disorder is more pronounced. However, in the doped compound the inherent (substitution) disorder is similar between the two series so their suppression rates are in line with each other. It is remarkable that such good mapping is possible between these two systems, which by themselves are complex materials with several significant differences (such as the magnetic and structural phases).

In conclusion, electron irradiation with 2.5 MeV electrons results in a rapid suppression of the superconducting transition temperature in both stoichiometric $CaKFe_4As_4$ and SVC antiferromagnetic $CaK(Fe_{0.95}Ni_{0.05})_4As_4$, suggesting a sign-changing superconducting energy gap. In both cases the low-temperature variation of London penetration depth data are consistent with nodeless superconducting state. The two observations provide the strongest support for $s_\pm$ pairing in the CaK1144 series. Physics of two effective gaps is evident in the $x = 0$ sample and the γ-model yields a range of 1-4 meV for the magnitude of the smaller gap and between 6-10 meV for the larger gap, which is also confirmed by the STM data. In the end, we show remarkable similarity between $CaK(Fe_{1-x}Ni_x)_4As_4$ ($x = 0, 0.05$) and $Ba_{1-y}K_yFe_2As_2$ ($y = 0.5, 0.2$) despite the differences in structural and magnetic arrangements.

4.7 References

[1] Akira Iyo, Kenji Kawashima, Tatsuya Kinjo, Taichiro Nishio, Shigeyuki Ishida, Hiroshi Fujihisa, Yoshito Gotoh, Kunihiro Kihou, Hiroshi Eisaki, and Yoshiyuki Yoshida. New-structure-type fe-based superconductors: Caafe4as4 (a = k, rb, cs) and srafe4as4 (a = rb, cs). *Journal of the American Chemical Society*, 138(10):3410–3415, 2016. PMID: 26943024.

[2] W R Meier, T Kong, U S Kaluarachchi, V Taufour, N H Jo, G Drachuck, A E Böhmer, S M Saunders, A Sapkota, A Kreyssig, M A Tanatar, R Prozorov, A I Goldman, Fedor F Balakirev, Alex Gurevich, S L Bud'ko, and P C Canfield. Anisotropic thermodynamic and transport properties of single-crystalline CaKFe 4 As 4.

[3] W R Meier, T Kong, S L Bud 'ko, and P C Canfield. Optimization of the crystal growth of the superconductor CaKFe 4 As 4 from solution in the FeAs-CaFe 2 As 2 -KFe 2 As 2 system. *PHYSICAL REVIEW MATERIALS*, 1, 2017.

[4] K. Cho, A. Fente, S. Teknowijoyo, M.A. Tanatar, K.R. Joshi, N.M. Nusran, T. Kong, W.R. Meier, U. Kaluarachchi, I. Guillamón, H. Suderow, S.L. Bud'Ko, P.C. Canfield, and R. Prozorov. Nodeless multiband superconductivity in stoichiometric single-crystalline CaKFe4As4. *Physical Review B*, 95(10), 2017.

[5] Daixiang Mou, Tai Kong, William R. Meier, Felix Lochner, Lin-Lin Wang, Qisheng Lin, Yun Wu, S. L. Bud'ko, Ilya Eremin, D. D. Johnson, P. C. Canfield, and Adam Kaminski. Enhancement of the superconducting gap by nesting in cakfe$_4$as$_4$: A new high temperature superconductor. *Phys. Rev. Lett.*, 117:277001, Dec 2016.

[6] Antón Fente, William R. Meier, Tai Kong, Vladimir G. Kogan, Sergey L. Bud'ko, Paul C. Canfield, Isabel Guillamón, and Hermann Suderow. Influence of multiband sign-changing superconductivity on vortex cores and vortex pinning in stoichiometric high-$T_c$cakfe$_4$as$_4$. *Phys. Rev. B*, 97:134501, Apr 2018.

[7] J. Cui, Q.-P. Ding, W. R. Meier, A. E. Böhmer, T. Kong, V. Borisov, Y. Lee, S. L. Bud'ko, R. Valentí, P. C. Canfield, and Y. Furukawa. Magnetic fluctuations and superconducting properties of cakfe$_4$as$_4$ studied by ^{75}As nmr. *Phys. Rev. B*, 96:104512, Sep 2017.

[8] Sergey L. Budko, Tai Kong, William R. Meier, Xiaoming Ma, and Paul C. Canfield. 57fe mssbauer study of stoichiometric iron-based superconductor cakfe4as4: a comparison to kfe2as2 and cafe2as2. *Philosophical Magazine*, 97(29):2689–2703, 2017.

[9] Udhara S. Kaluarachchi, Valentin Taufour, Aashish Sapkota, Vladislav Borisov, Tai Kong, William R. Meier, Karunakar Kothapalli, Benjamin G. Ueland, Andreas Kreyssig, Roser Valentí, Robert J. McQueeney, Alan I. Goldman, Sergey L. Bud'ko, and Paul C. Canfield. Pressure-induced half-collapsed-tetragonal phase in cakfe$_4$as$_4$. *Phys. Rev. B*, 96:140501, Oct 2017.

[10] Vladislav Borisov, Paul C. Canfield, and Roser Valentí. Trends in pressure-induced layer-selective half-collapsed tetragonal phases in the iron-based superconductor family *aea*fe$_4$as$_4$. *Phys. Rev. B*, 98:064104, Aug 2018.

[11] G A Ummarino. Phenomenology of CaKFe 4 As 4 explained in the framework of four bands Eliashberg theory. 529:50–53, 2016.

[12] Felix Lochner, Felix Ahn, Tilmann Hickel, and Ilya Eremin. Electronic properties, low-energy hamiltonian, and superconducting instabilities in cakfe$_4$as$_4$. *Phys. Rev. B*, 96:094521, Sep 2017.

[13] P. K. Biswas, A. Iyo, Y. Yoshida, H. Eisaki, K. Kawashima, and A. D. Hillier. Signature of multigap nodeless superconductivity in cakfe$_4$as$_4$. *Phys. Rev. B*, 95:140505, Apr 2017.

[14] Kazuki Iida, Motoyuki Ishikado, Yuki Nagai, Hiroyuki Yoshida, Andrew D Christianson, Naoki Murai, Kenji Kawashima, Yoshiyuki Yoshida, Hiroshi Eisaki, and Akira Iyo. Spin Resonance in the New-Structure-Type Iron-Based Superconductor CaKFe 4 As 4 Letters. 2017.

[15] Rustem Khasanov, William R. Meier, Yun Wu, Daixiang Mou, Sergey L. Bud'ko, Ilya Eremin, Hubertus Luetkens, Adam Kaminski, Paul C. Canfield, and Alex Amato. In-plane magnetic penetration depth of superconducting cakfe$_4$as$_4$. *Phys. Rev. B*, 97:140503, Apr 2018.

[16] K. R. Joshi, N. M. Nusran, K. Cho, M. A. Tanatar, W. R. Meier, S. L. Bud'ko, P. C. Canfield, and R. Prozorov. Measurements of the lower critical field of superconductors using nv centers in diamond optical magnetometry, 2018.

[17] Shiv J. Singh, Matthew Bristow, William R. Meier, Patrick Taylor, Stephen J. Blundell, Paul C. Canfield, and Amalia I. Coldea. Ultrahigh critical current densities, the vortex phase diagram, and the effect of granularity of the stoichiometric high-T_c superconductor cakfe$_4$as$_4$. *Phys. Rev. Materials*, 2:074802, Jul 2018.

[18] William R Meier, Qing-Ping Ding, Andreas Kreyssig, Sergey L Bud'ko, Aashish Sapkota, Karunakar Kothapalli, Vladislav Borisov, Cristian D Batista, Peter P Orth, Rafael M Fernandes, Alan I Goldman, Yuji Furukawa, Anna E Böhmer, and Paul C Canfield. Hedgehog spin-vortex crystal stabilized in a hole-doped iron-based superconductor. 3:5, 2018.

[19] K. Hashimoto, K. Cho, T. Shibauchi, S. Kasahara, Y. Mizukami, R. Katsumata, Y. Tsuruhara, T. Terashima, H. Ikeda, M. A. Tanatar, H. Kitano, N. Salovich, R. W. Giannetta, P. Walmsley, A. Carrington, R. Prozorov, and Y. Matsuda. A sharp peak of the zero-temperature penetration depth at optimal composition in bafe2(as1–xpx)2. *Science*, 336(6088):1554–1557, 2012.

[20] K. Cho, M. Konczykowski, S. Teknowijoyo, M. A. Tanatar, Y. Liu, T. A. Lograsso, W. E. Straszheim, V. Mishra, S. Maiti, P. J. Hirschfeld, and R. Prozorov. Energy gap evolution across the superconductivity dome in single crystals of (Ba1-xKx)Fe2As2. *Science Advances*, 2(9):e1600807–e1600807, 2016.

[21] H. Suderow, I. Guillamon, and S. Vieira. Compact very low temperature scanning tunneling microscope with mechanically driven horizontal linear positioning stage. *Review of Scientific Instruments*, 82(3):033711, 2011.

[22] A Fente, I Guillamn, S Ran, S Vieira, H Suderow, S L Bud'ko, and P C Canfield. Observation of unreconstructed square atomic square lattice in ca(fe 0.965 co 0.035) 2 as 2 cleaved at very low temperatures. *Journal of Physics: Conference Series*, 568(2):022046, 2014.

[23] I. Guillamon, H. Suderow, S. Vieira, and P. Rodiere. Scanning tunneling spectroscopy with superconducting tips of al. *Physica C: Superconductivity and its Applications*, 468(7):537 – 542, 2008. Proceedings of the Fifth International Conference on Vortex Matter in Nanostructured Superconductors.

[24] G. Rubio-Bollinger, H. Suderow, and S. Vieira. Tunneling spectroscopy in small grains of superconducting mgb_2. *Phys. Rev. Lett.*, 86:5582–5584, Jun 2001.

[25] I. Guillamón, H. Suderow, S. Vieira, L. Cario, P. Diener, and P. Rodière. Superconducting density of states and vortex cores of 2h-nbs_2. *Phys. Rev. Lett.*, 101:166407, Oct 2008.

[26] Lei Shan, Yong Lei Wang, Bing Shen, Bin Zeng, Yan Huang, Ang Li, Da Wang, Huan Yang, Cong Ren, Qiang Hua Wang, Shuheng H. Pan, and Hai Hu Wen. Observation of ordered vortices with Andreev bound states in Ba0.6K0.4Fe2As2. *Nature Physics*, 7(4):325–331, apr 2011.

[27] Jennifer E Hoffman. Spectroscopic scanning tunneling microscopy insights into fe-based superconductors. *Reports on Progress in Physics*, 74(12):124513, 2011.

[28] F. Massee, Y. Huang, R. Huisman, S. de Jong, J. B. Goedkoop, and M. S. Golden. Nanoscale superconducting-gap variations and lack of phase separation in optimally doped $bafe_{1.86}co_{0.14}as_2$. *Phys. Rev. B*, 79:220517, Jun 2009.

[29] H Suderow, I Guillamn, J G Rodrigo, and S Vieira. Imaging superconducting vortex cores andlattices with a scanning tunneling microscope. *Superconductor Science and Technology*, 27(6):063001, 2014.

[30] Øystein Fischer, Martin Kugler, Ivan Maggio-Aprile, Christophe Berthod, and Christoph Renner. Scanning tunneling spectroscopy of high-temperature superconductors. *Rev. Mod. Phys.*, 79:353–419, Mar 2007.

[31] P. Martinez-Samper, J.G. Rodrigo, G. Rubio-Bollinger, H. Suderow, S. Vieira, S. Lee, and S. Tajima. Scanning tunneling spectroscopy in mgb2. *Physica C: Superconductivity*, 385(1):233 – 243, 2003.

[32] J.G. Rodrigo and S. Vieira. Stm study of multiband superconductivity in nbse2 using a superconducting tip. *Physica C: Superconductivity*, 404(1):306 – 310, 2004. Proceedings of the Third European Conference on Vortex Matter in Superconductors at Extreme Scales and Conditions.

[33] K. Cho, M. Kończykowski, J. Murphy, H. Kim, M. A. Tanatar, W. E. Straszheim, B. Shen, H. H. Wen, and R. Prozorov. Effects of electron irradiation on resistivity and london penetration depth of $ba_{1-x}k_xfe_2as_2 (x \leq 0.34)$ iron-pnictide superconductor. *Phys. Rev. B*, 90:104514, Sep 2014.

[34] H. Kim, M. A. Tanatar, W. E. Straszheim, K. Cho, J. Murphy, N. Spyrison, J.-Ph. Reid, Bing Shen, Hai-Hu Wen, R. M. Fernandes, and R. Prozorov. Competition between superconductivity and magnetic/nematic order as a source of anisotropic superconducting gap in underdoped $ba_{1-x}k_xfe_2as_2$. *Phys. Rev. B*, 90:014517, Jul 2014.

[35] J.-Ph. Reid, M. A. Tanatar, X. G. Luo, H. Shakeripour, S. René de Cotret, A. Juneau-Fecteau, J. Chang, B. Shen, H.-H. Wen, H. Kim, R. Prozorov, N. Doiron-Leyraud, and Louis Taillefer. Doping evolution of the superconducting gap structure in the underdoped iron arsenide $ba_{1-x}k_xfe_2as_2$ revealed by thermal conductivity. *Phys. Rev. B*, 93:214519, Jun 2016.

[36] S. Teknowijoyo, K. Cho, M. Kończykowski, E. I. Timmons, M. A. Tanatar, W. R. Meier, M. Xu, S. L. Bud'ko, P. C. Canfield, and R. Prozorov. Robust $s_\pm$ pairing in $CaK(Fe_{1-x}Ni_x)_4as_4$ ($x = 0$ and 0.05) from the response to electron irradiation. *Phys. Rev. B*, 97:140508, Apr 2018.

[37] R Prozorov and V G Kogan. London penetration depth in iron-based superconductors. *Reports on Progress in Physics*, 74(12):124505, 2011.

[38] S. Maiti, R. M. Fernandes, and A. V. Chubukov. Gap nodes induced by coexistence with antiferromagnetism in iron-based superconductors. *Phys. Rev. B*, 85:144527, Apr 2012.

[39] M. A. Tanatar, J. Ph Reid, H. Shakeripour, X. G. Luo, N. Doiron-Leyraud, N. Ni, S. L. Bud'Ko, P. C. Canfield, R. Prozorov, and Louis Taillefer. Doping dependence of heat transport in the iron-arsenide superconductor Ba(Fe1-xCox)2As2: From isotropic to a strongly K-dependent gap structure. *Physical Review Letters*, 104(6):067002, feb 2010.

[40] J.-Ph. Reid, M. A. Tanatar, X. G. Luo, H. Shakeripour, N. Doiron-Leyraud, N. Ni, S. L. Bud'ko, P. C. Canfield, R. Prozorov, and Louis Taillefer. Nodes in the gap structure of the iron arsenide superconductor $Ba(Fe_{1-x}Co_x)_2as_2$ from c-axis heat transport measurements. *Phys. Rev. B*, 82:064501, Aug 2010.

[41] C. Martin, H. Kim, R. T. Gordon, N. Ni, V. G. Kogan, S. L. Bud'ko, P. C. Canfield, M. A. Tanatar, and R. Prozorov. Evidence from anisotropic penetration depth for a three-dimensional nodal superconducting gap in single-crystalline $Ba(Fe_{1-x}Ni_x)_2as_2$. *Phys. Rev. B*, 81:060505, Feb 2010.

[42] Y. Liu, M. A. Tanatar, W. E. Straszheim, B. Jensen, K. W. Dennis, R. W. McCallum, V. G. Kogan, R. Prozorov, and T. A. Lograsso. Comprehensive scenario for single-crystal growth and doping dependence of resistivity and anisotropic upper critical fields in $(ba_{1-x}k_x)fe_2as_2$ ($0.22 \leq x \leq 1$). *Phys. Rev. B*, 89:134504, Apr 2014.

[43] V. G. Kogan and R. Prozorov. Interband coupling and nonmagnetic interband scattering in $\pm s$ superconductors. *Phys. Rev. B*, 93:224515, Jun 2016.

[44] V. G. Kogan, C. Martin, and R. Prozorov. Superfluid density and specific heat within a self-consistent scheme for a two-band superconductor. *Phys. Rev. B*, 80:014507, Jul 2009.

[45] R. Prozorov, R. W. Giannetta, A. Carrington, and F. M. Araujo-Moreira. Meissner-london state in superconductors of rectangular cross section in a perpendicular magnetic field. *Phys. Rev. B*, 62:115–118, Jul 2000.

[46] H. Kim, V. G. Kogan, K. Cho, M. A. Tanatar, and R. Prozorov. Rutgers relation for the analysis of superfluid density in superconductors. *Phys. Rev. B*, 87:214518, Jun 2013.

[47] Chia-Ren Hu. Numerical constants for isolated vortices in superconductors. *Phys. Rev. B*, 6:1756–1760, Sep 1972.

[48] E. H. Brandt. Geometric edge barrier in the shubnikov phase of type-ii superconductors. *Low Temperature Physics*, 27(9):723–731, 2001.

[49] R. Prozorov and V. G. Kogan. Effective demagnetizing factors of diamagnetic samples of various shapes. *Phys. Rev. Applied*, 10:014030, Jul 2018.

CHAPTER 5. LONDON PENETRATION DEPTH AND ELECTRON IRRADIATION IN FeSe

Modified from a manuscript published in

Physical Review B 94, 064521 (2016)

S. Teknowijoyo,[1] K. Cho,[1] M. A. Tanatar,[1] J. Gonzales,[1] A. E. Böhmer,[1] O. Cavani,[2] V. Mishra,[3] P. J. Hirschfeld,[4] S. L. Bud'ko,[1] P. C. Canfield,[1] R. Prozorov[1]

[1] Ames Laboratory and Department of Physics and Astronomy, Iowa State University, Ames, IA 50011 USA

[2] Laboratoire des Solides Irradiés, École Polytechnique, CNRS, CEA, Université Paris-Saclay, 91128 Palaiseau Cedex, France

[3] Joint Institute for Computational Sciences, University of Tennessee, Knoxville, TN 37996, USA

[4] Department of Physics, University of Florida, Gainesville, FL 32611, USA

5.1 Abstract

A highly anisotropic superconducting gap is found in single crystals of FeSe by studying the London penetration depth, $\Delta\lambda$, measured down to 50 mK in samples before and after 2.5 MeV electron irradiation. The gap minimum increases with introduced point - like disorder, indicating the absence of symmetry - imposed nodes. Surprisingly, the superconducting transition temperature, T_c, increases by 0.4 K from $T_{c0} \approx 8.8$ K while the structural transition temperature, T_s, decreases by 0.9 K from $T_{s0} \approx 91.2$ K after electron irradiation. We discuss several explanations for the T_c enhancement, and propose that local strengthening of the pair interaction by irradiation-induced Frenkel defects most likely explains the phenomenon.

5.2 Introduction

After investigating a representative member from each of the 122 and 1144 families in previous discussion, in this chapter we will turn to FeSe, a member of the 11 family. The crystallographic structure of this family can be considered as the simplest among all iron-based superconductors because it only consists of iron-containing layer without any intermediate/spacing layers (Fig 5.1(a)). In terms of the chemical composition Se may be replaced partially (doped) or fully (stoichiometric) by other elements such as S [1, 2], Te [3] or more recently reported, Be [4]. Some of such binary phase diagrams are shown below in Fig. 5.1(c), (d) and Fig. 1.2(a). In single crystal FeSe bulk superconductivity occurs at $T_c \sim 9$ K [5]. However, the superconductivity in FeSe is highly sensitive to its growth conditions and the experimental environment. Studies of chemical doping [1, 2, 3, 4, 6] and the application of pressure [2, 7, 8] reported moderate increase (up to 40 K) while monolayer growth [9, 10] revealed astounding increase ($\approx$ 100 K) of T_c. Such T_c increase of an order of magnitude is highly unusual and is thought to be strongly related to the $SrTiO_3$ substrate through electron-phonon interactions [9, 11]. An in-depth review for the possible origins of the T_c increase in a monolayer of FeSe is described elsewhere [12].

When cooled down in ambient pressure, bulk FeSe undergoes tetragonal to orthorhombic structural transition at $\sim$ 90 K without the usual accompaniment of long-range magnetic ordering [5, 14]. This provides an opportunity to study superconductivity without the complications of the interplay with magnetism, as well as the significant scattering found in other doped iron-based superconductors. In a sense, FeSe may be thought as the opposite of Ni-doped $CaKFe_4As_4$, where the SVC magnetic order is stabilized without a structural transition. In other words, both FeSe and Ni-doped CaK1144 provide an opportunity to probe the coexistence of superconductivity with the structural or the magnetic phase independently.

Despite the absence of long range magnetism, a strong electronic nematic response is reported in FeSe whose origin is discussed in terms of both spin and orbital fluctuations [14, 15, 16, 17, 18, 19]. Strictly speaking, nematicity is the spontaneous tetragonal symmetry breaking in the electronic structure which may be related to, but not to be confused with the lowering of the

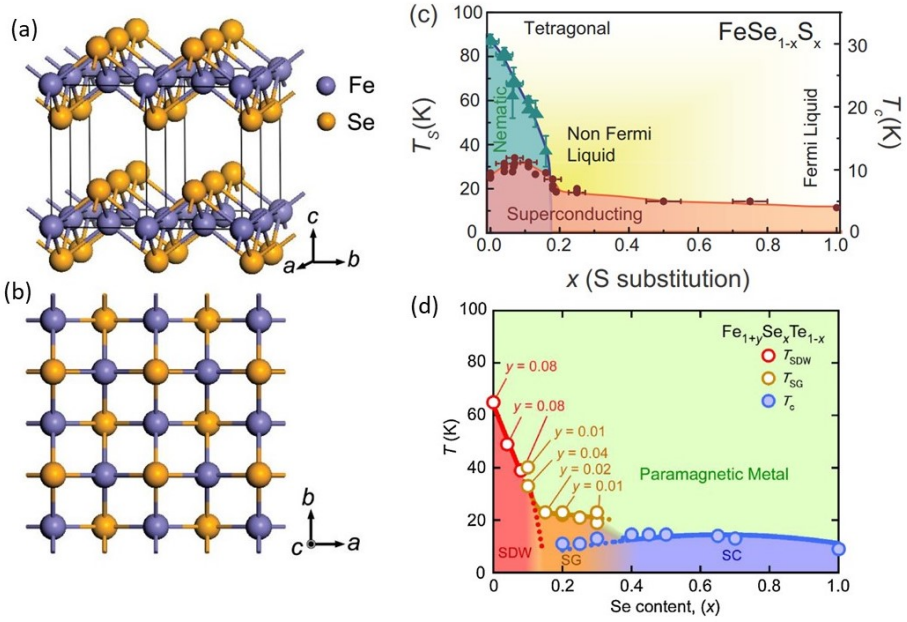

Figure 5.1 (a) And (b) a schematic crystal structure of FeSe. Four unit cells are shown to reveal the layered structure. (c) $T - x$ phase diagram of $FeSe_{1-x}S_x$. The T_c peaks inside the nematic phase which suggests an intricate interplay between superconductivity and nematicity upon S doping. (d) $T - x$ phase diagram of $Fe_{1+y}Se_xTe_{1-x}$ constructed from single crystal bulk susceptibility data. The nominal Fe content, y, is $y = 0$ unless it is specified. T_c (blue circles) represents the superconducting onset temperature. SDW, SG and SC refer to spin-density wave, spin glass and superconducting phases, respectively. (a) And (b) from Ref. [13], (c) from Ref. [6], (d) from Ref. [3].

crystal symmetry (orthorhombicity). A long-range magnetic order was later discovered upon the application of external pressure of $\sim$ 1 GPa [7, 20], which also revealed a highly non-trivial pressure dependence of T_c which has a local maxima at $\sim$ 0.8 GPa and a local minima at $\sim$ 1.3 GPa [7, 8]. A pressure-NMR [21] and an inelastic neutron scattering [22] experiments investigating the magnetism in FeSe revealed results consistent with the stripe-type antiferromagnetism which is the same motif found in the 122 family. These observations suggest that FeSe might be closer to the "mainstream" iron-based superconductors (such as the 122 family) than previously thought.

5.2.1 FeSe gap structure

Although FeSe has the simplest crystallographic structure, it turns out that its electronic band and superconducting gap structures did not get as easily and conclusively proven. Early investigations were not able to come into a converging consensus which was evident in both theoretical and experimental sides. For example, anisotropic line nodes or deep minima were found theoretically in FeSe [23, 24, 25], which was also claimed experimentally from the STM [26], London penetration depth and thermal conductivity [27] measurements. However, measurements of the lower critical field [28], low-temperature specific heat [29, 30, 31], other STM [30], and other thermal conductivity studies [32, 33] are consistent with the nodeless superconducting gap. A crossover from nodal in the bulk to nodeless at the twin boundary is found from STM [34]. Li *et al.* independently arrived at the same conclusions even with a matching estimate of the gap minimum [35]. They also discussed long quasiparticle relaxation times and an extended self-consistent γ-model to include anisotropic gaps. In all these studies however, a highly anisotropic gap and/or effective two-band physics are present. On the other hand, a single large nodeless gap has been reported in monolayer FeSe [11, 36]. Just like the variation in T_c, all these reports show how susceptible FeSe is to modification of its chemical-physical state and the results can vary from sample-to-sample basis.

One possible scenario to reconcile these apparently contradictory results is to consider marginal, accidental nodes in the clean limit which are lifted by the natural disorder already present in the sample [20, 33]. This makes the study of artificial disorder using electron irradiation in FeSe even

more fitting, in order to probe the plausibility of this scenario. Specifically, we probe the gap structure in FeSe before and after irradiation using the measurement of low-temperature London penetration depth.

5.3 Experimental Details

5.3.1 Sample preparation

We used single crystals grown using a modified chemical vapor transport method provided by Anna Böhmer [8, 37]. The samples for the study have typical dimensions of $\sim$ 0.5 x 0.5 x 0.03 mm^3. Other crystals from the same batch or a similar ones were extensively characterized by measurements of magnetization, electrical transport, Mössbauer spectroscopy and high energy x-ray scattering, including under pressure, as described in other reports [7, 8, 14]. In our samples the typical ratio of resistivities, RRR(300/10) $\equiv \rho(300\text{ K})/\rho(10\text{ K}) \approx 20$ and a linear extrapolation to $T = 0$ gives RRR(300/0) ≈ 125. In comparison, a previous study on vapor transport grown FeSe samples that found nodal superconductivity gives a very similar response for RRR(300/10), but has a negative value after linear extrapolation, indicating a lower residual resistivity $\rho(0)$ and a slightly less disordered sample [27].

In-plane London penetration depth $\Delta\lambda_{ab}(T)$ was measured down to 50 mK in two samples (labeled A and B) before and after 1.8 C/cm^2 electron irradiation. A third sample (C) was measured in $\Delta\lambda_{ab}(T)$ and $\Delta\lambda_c(T)$ configurations following the protocol described in Ref.[38, 39].

***Erratum* for the original paper.** At the time of writing, the now published work [5] contains London penetration depth data that has a miscalibration by a factor of ≈ 2. The error was found soon after the time of publication and most of the figures in this chapter have been revised with the correct calibration. None of the qualitative picture drawn in the original paper is affected. However, we did not redo the γ-model fitting of the superfluid density so one may question the accuracy of the details of the gap parameters which were obtained from the original analysis. Nevertheless, I will present the revised superfluid density side by side with the original work. I will argue that the revised curve is fully compatible with all the conclusions drawn in the original paper [5].

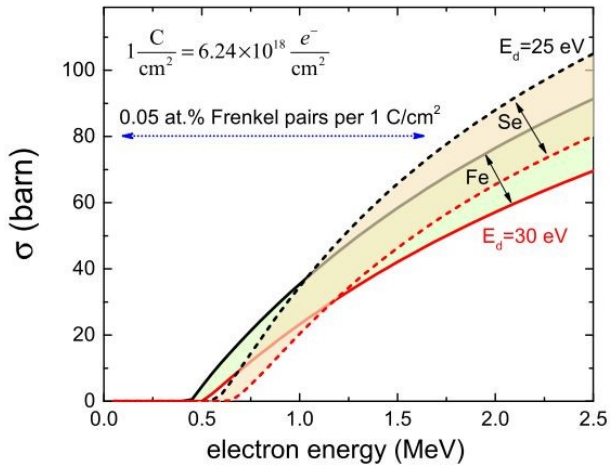

Figure 5.2 An ion-specific cross-sections calculated by using SECTE program [42]. The upper curves correspond to the ion knock-out threshold of $E_d = 25$ eV, the lower curves to $E_d = 30$ eV. Se is shown by dashed curves, Fe by solid curves. At the mid-range value of 80 barn, we expect 0.05% probability of creating a Frenkel pair per ion type. From Ref.[5] Supplemental Material.

5.3.2 Electron irradiation

To investigate the effect of deliberately introduced point-like disorder $\Delta\lambda(T)$ was measured before and after 2.5 MeV electron irradiation which was performed at the SIRIUS Pelletron Facility (Ch. 2). The accumulated dose on the two samples used in this study is 1.8 C/cm^2 = 1.12 x 10^{19} e$^-$/cm^2. It is known that for certain materials and thick samples, electron irradiation may result in a non-uniform distribution of the created defects in the longitudinal direction [40]. However, due to the small thickness of our samples we expected a very uniform defect creation. To confirm our prediction we used NIST's ESTAR software to calculate the energy loss due to brehmsstrahlung radiation by 2.5 MeV electrons in FeSe [41]. We found that the average energy loss by 2.5 MeV electrons passing through a 0.03 mm thick FeSe sample is only 26 keV ($\sim$ 1% of the initial energy). Furthermore, the average stopping depth traveled by an electron inside FeSe until it slows down to a full rest was estimated at $\sim$ 1.2 mm, which is far greater than the thickness of our samples. Both calculations indicate a highly uniform distribution of the created defects.

Next we estimate the number of the defects created by 2.5 MeV electron irradiation. Fig. 5.2 shows ion-specific cross-sections calculated by using the SECTE simulation package, which was redeveloped by the researchers in the Ecole Polytechnique facility [42]. In the figure, two pairs of curves for Fe (solid lines) and Se (dashed lines) are plotted for two values of the displacement energy. The energy range between E_d = 25 eV (upper curves) and E_d = 30 eV (lower curves) gives the displacement energies commonly found in studies of various materials [43, 44]. At the energy of the electrons used in this study (2.5 MeV), the average cross sections of all four curves is ∼80 barn. From here we estimate that 1 C/cm^2 of irradiation dose has a 0.05% probability to generate a Frenkel pair for each Fe or Se ions. A unit cell of FeSe has Z=2 which corresponds to the 0.2% probability of generating a defect per C/cm^2 of irradiation. To apply the probability to our samples which accumulated a dose of 1.8 C/cm^2, we estimate about 2 x 1.8 x 1 x 10^{-3} = 0.0036 Frenkel pairs (of either Fe or Se) per unit volume. Since FeSe has a unit cell with V = 78.4 Å^3 [37], a volume that will contain at least one Frenkel pair is 78.4/0.0036 = 2.2 x 10^4 Å^3. Assuming a simple geometry, the average distance between these defects is just $l \approx (2.1 \text{ x } 10^4)^{1/3}$ = 30 Å. Taking into account the annealing of up to ∼30% of the defects upon warming up, the distance can be estimated to increase by a factor of $\frac{10}{7}^{1/3}$ which is just about 10% enhancement. Now we can compare this average distance to the coherence length of the material. Since the $H_{c2,c} \approx 17$ T along the c-axis and $H_{c2,ab} \approx 30$ T in the planar directions [45], we can use the relation $H_{c2} = \phi_0 \, (2\pi\xi^2)^{-1}$ to get the coherence lengths ξ_c = 110 Å and ξ_{ab} = 83 Å, respectively. These values are consistent with a superconductor with a mild degree of anisotropy. Terashima *et al.* estimate the coherence lengths from the slope of dH_{c2}/dT at 130 Å and 57 Å which are close to our estimate. Although these values are estimated from the measurements of pristine FeSe, we only expect irradiation to push them slightly toward the higher end. In either case, these coherence lengths are larger than the distance between the defects of ∼33 Å. Combined with the fact that these defects are non-magnetic, for an anisotropic superconductor in this regime ($l < \xi$) T_c suppression is expected to saturate as function of scattering [46].

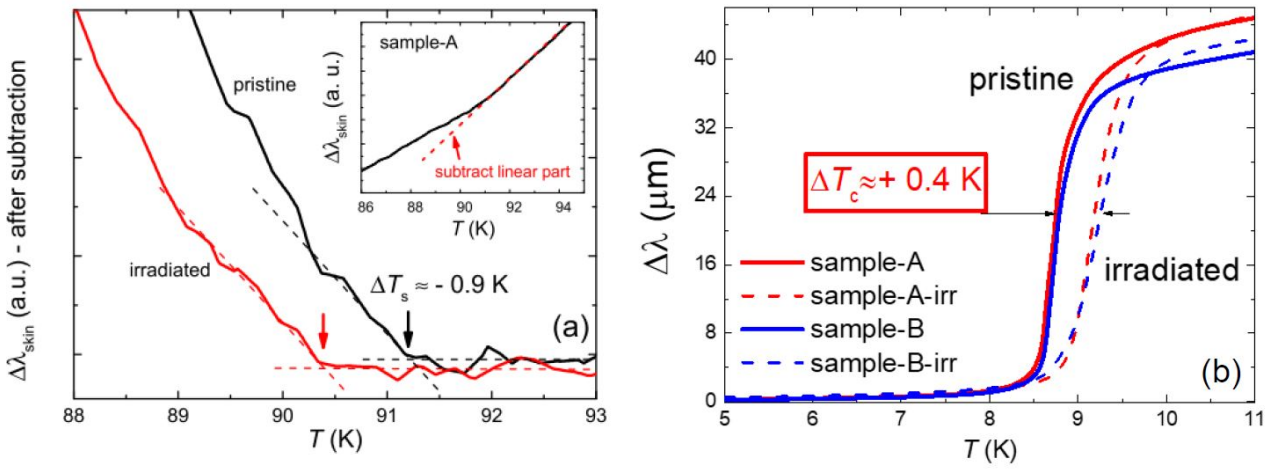

Figure 5.3 (a) The variation of the normal state skin-depth $\Delta\lambda_{skin}(T \gg T_c)$ of sample A after a linear-subtraction as shown in the inset. Arrows mark the structural transition T_s, before and after 2.5 MeV electron irradiation of 1.8 C/cm^2. (b) London penetration depth $\Delta\lambda(T)$ before and after electron irradiation in samples A and B. The pristine sample had a mid-point $T_c \approx 8.8$ K which increased after irradiation as shown by the arrows. Adapted and revised from Ref. [5].

5.4 Results

Fig. 5.3 shows the high temperature (up to ∼95 K) measurements to probe the effect of electron irradiation on T_c and T_s. In the normal state, the TDR signal is proportional to the normal skin depth $\lambda_{skin} = (\rho(T)/\pi\mu f)^2$, where f is the resonator frequency and μ is the magnetic permeability. The resistivity $\rho(T)$ has a kink at T_s [14] which is detected here via $\lambda_{skin}(T)$. To visualize the transition better, we subtract a linear part above T_s as shown in the inset of Fig. 5.3(a). The structural transition temperature T_s has shifted down by -0.9 K in sample A after irradiation. Similar behavior was also observed for Sample B (not shown). Fig. 5.3(b) shows the region of the superconducting transition. Both samples A and B show a very similar behavior with $T_c \approx$ 8.8 K (mid-point) which *increased* by 0.4 K. Such T_c increase upon electron irradiation is highly unusual and its observation imposes strict limitations on the structure of the superconducting order parameter. We note that although T_c enhancement reported here was measured in two different samples, we only had the opportunity to access one irradiation dose of 1.8 C/cm^2. Scenarios

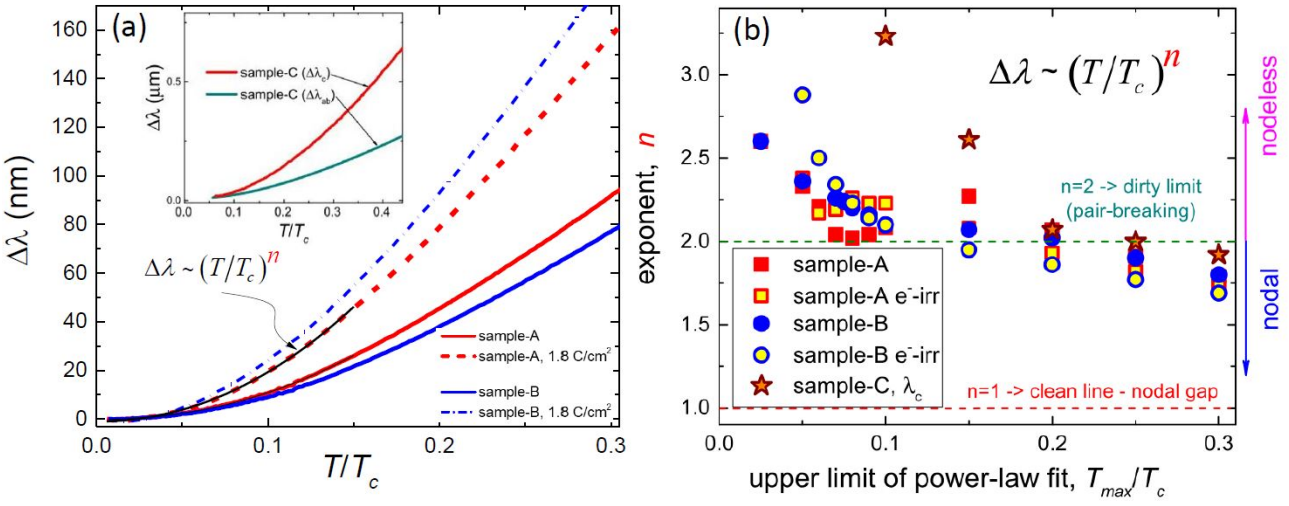

Figure 5.4 (a) The low temperature part of $\Delta\lambda(t \equiv T/T_c)$ of samples A (red) and B (blue) before (solid lines) and after (dashed lines) of 2.5 MeV electron irradiation of 1.8 C/cm^2. The arrow points to an example of the power-law fit $\Delta\lambda(t) \propto t^n$. Inset shows $\Delta\lambda_{ab}$ (teal) and $\Delta\lambda_c$ (red) of sample C. (b) The exponent n obtained from the power-law fitting for the data shown in (a). The x-axis is the upper limit of the fitting range, T_{max}/T_c. In all samples, the exponents increase to well above the dirty limit of $n = 2$ at low temperatures indicating the presence of a small but finite superconducting gap. After electron irradiation n becomes even higher, which is consistent with the reduction of the gap anisotropy. The c-axis direction is also fully gapped. Adapted and revised from Ref. [5].

discussed in this Chapter may, in fact, lead to some non-monotonic behavior and further studies of T_s and T_c as functions of irradiation dose are needed.

Fig. 5.4(a) shows $\Delta\lambda(t)$ of samples A and B before (solid lines) and after (dashed lines) 2.5 MeV electron irradiation with the dose of 1.8 C/cm^2. Here, $t \equiv T/T_c$ is the normalized temperature. At the lowest temperatures ($t < 0.05$) the penetration depth remains practically flat. Its amplitude increases faster with temperatures in irradiated samples, signaling an increase of the number of thermally excited quasiparticles compared to the pristine case. The inset shows in-plane ($\Delta\lambda_{ab}$) and out-of-plane ($\Delta\lambda_c$) penetration depths measured in sample C [38]. The ratio of $\Delta\lambda_{ab}$ and $\Delta\lambda_c$ at $t = 0.3$ is about 3, consistent with the relatively low anisotropy of other iron-based superconductors [38].

5.5 Analysis

Presented in the next subsection is the low temperature analyses on the revised figures with the corrected calibration as discussed earlier. Since the corrected calibration only practically scales the magnitude of $\Delta\lambda(T)$ by a factor of ≈ 2, it leaves the low temperature power-law behavior (linear, T^2 or exponential) unaltered. Therefore the original results presented in [5] are still valid, since the analyses only depend on the exponent of the power-law or the BCS fitting on the temperature dependence.

However, we caution the reader to discern the values of the gap magnitude and gap anisotropy drawn in the superfluid density subsection. The γ-model fitting was performed on the original curve with an inaccurate calibration and we did not redo the fitting since all the qualitative results are fully compatible with the revised superfluid density curve (which is presented in the Conclusions). Here we still present the results from the original paper [5] since it still serves as a good example of how to analyze the superfluid density data of a given material.

5.5.1 Low temperature behavior

With an apparent saturation of $\Delta\lambda(T)$ only at quite low temperatures, we analyze its behavior using two approaches. First, following our previous studies [38] we fit the London penetration depth by the power-law $\Delta\lambda(t) \propto t^n$. The solid black curve (indicated by an arrow in Fig. 5.4(a)) shows an example of such a fit. We examine the dependence of the exponent n on the upper limit of the fitting range T_{max}/T_c, which was varied from 0.05 T_c to 0.3 T_c while the lower limit was fixed at the base temperature of ~ 50 K. Fig. 5.4(b) shows how the exponent n increases with the decrease of T_{max}/T_c, reaching the values significantly greater than 2 below $0.1T_c$. This indicates that the average gap value is significantly anisotropic with the presence of a small but finite gap, because both accidental and symmetry-imposed line nodes result in $1 \leq n \leq 2$.

As discussed in the Introduction, some STM experiments on high quality samples reported evidence for gap nodes in thin films [26] and single crystals [27]. Furthermore from the theoretical stand-point, a ground state with a very shallow C_2-symmetric nodes was found within the spin

fluctuation calculations with orbital ordering [24, 25] so both findings are in apparent contrast to our small gap result. We note here that because our samples are twinned [37], the supercurrent flows through structural domains of both orientations. In principle, if one orientation is nodal we should detect it in the clean limit. However, we know that accidental nodes can be lifted by intraband disorder scattering [47]. It may, therefore, be that our samples are slightly more disordered than those that show nodes. A similar suggestion was made on thermal conductivity [33] and (ARPES + thermodynamics) [20] measurements.

It is also possible that samples of FeSe differ from one another not because of small differences in the defect concentrations, but due to different concentrations of twin boundaries due to the growth conditions or the sample mounting. Watashige *et al.* [34] have shown that even the bulk crystals exhibiting a nodal state show large scale regions of full gap behavior in the neighborhood of twin boundaries. Depending on its irregularity, the twin boundary may act as a pair breaker in which case this effect might be simply another version of the disorder node lifting phenomenon. The long range nature of the effect suggests however, that other physics maybe in play [34]. With only our data we cannot make convincing statements about the origin of our small gaps but it appears clear that the gap is sensitive to small perturbations, which can gap a nodal state. The most natural explanation then, is that disorder is lifting the nodes in slightly less pure samples or the ones with a higher twin density.

Our second approach to analyze the low temperature behavior is to use the BCS single gap fit $\Delta\lambda(t) = C_1 + C_2\sqrt{\pi\delta/2t}\,\exp(-\delta/t)$, with a variable upper temperature limit T_{max}/T_c. C_1, C_2 and $\delta \equiv \Delta(0)/T_c$ are free parameters. This procedure can be used to estimate the minimum gap in the system provided that the measurements were done down to low enough temperature, which is the case here. Fig. 5.5(a) shows examples of the exponential fitting of the sample B data before and after electron irradiation. Fig. 5.5(b) presents the ratio of $\Delta(0)/T_c$ obtained as the best fit parameter for several values of the upper limit of the fitting range. While there is only a hint of saturation in the pristine curve, the fits of the irradiated state saturated at about $\Delta_{min}(0)/T_c$ indicating a truly exponential behavior. In addition, we see that the smaller range fits

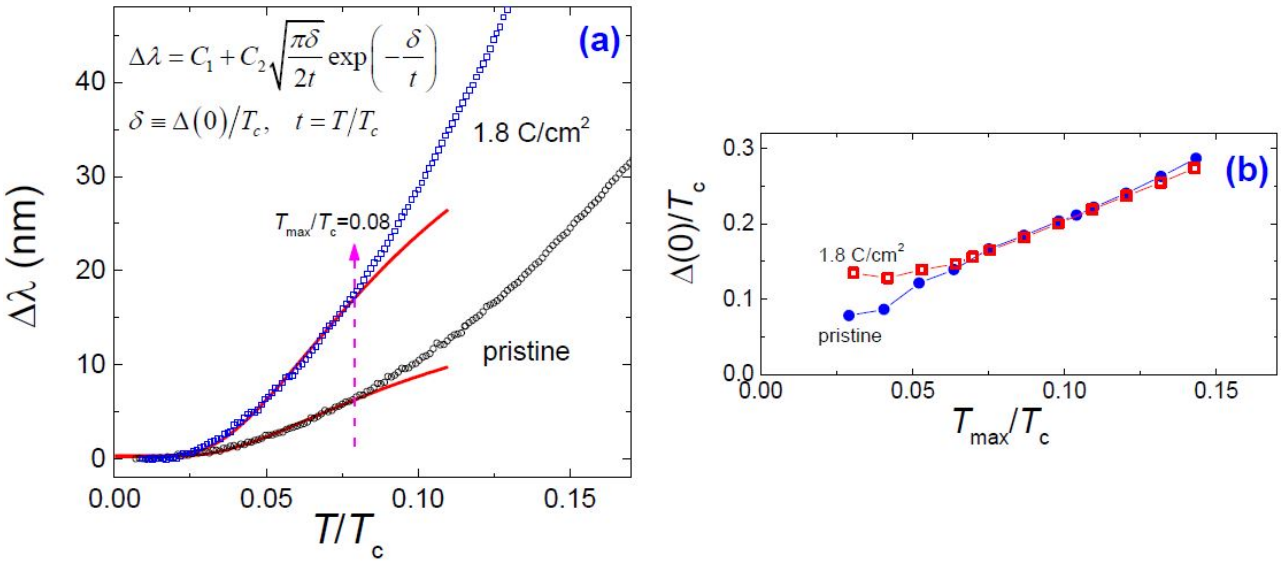

Figure 5.5 (a) The low temperature $\Delta\lambda(t)$ data of sample B with an example of BCS fitting for $T_{max}/T_c \approx 0.08$ before (lower curve) and after 1.8 C/cm^2 electron irradiation (upper curve). Also shown are the equation and definitions used. (b) $\Delta(0)/T_c$ ratio obtained as a best fit parameter with different upper limits of the fitting range, which is plotted as the x-axis. Adapted and revised from Ref. [5].

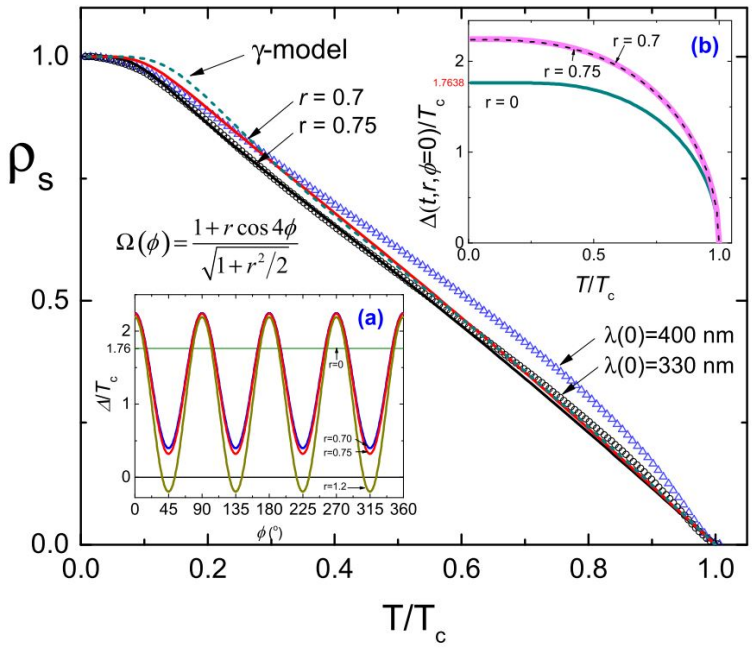

Figure 5.6 The superfluid density analyzed in terms of anisotropic gap in the form shown. The best fit is obtained for ρ_s calculated with $\lambda(0) = 330$ nm. However, with $\rho_s = 400$ nm the fit is also reasonable for the range $t \leq 0.3$. For completeness, a two-gap γ-model [48] fit is shown by the dashed line. Inset (a) shows the angular variation of the gap with $r = 0.70$ (best fit of $\lambda(0) = 400$ nm data), $r = 0.75$ (best fit of $\lambda(0) = 330$ nm data) and $r = 1.2$ of the hypothetical accidental nodes state, just for comparison. Inset (b) shows the variation of the gap with temperature obtained from the self-consistency equation 5.1. Taken from Ref. [5], which was found to be slightly miscalibrated after the paper was published however, all the qualitative results are still valid.

indicate clearly that the minimum gap has increased upon irradiation, a phenomenon analogous to node lifting which results from the averaging of the gap anisotropy by intraband disorder [47]. This is only possible if the anisotropy and possible nodes are not imposed by the pairing potential symmetry (i.e. anisotropic s-wave, or $s_{\pm}$, but not d-wave).

5.5.2 Superfluid density

To gain further insight into the gap structure, we need to analyze the temperature-dependent superfluid density ($\rho_s(T) = (1 + \Delta\lambda(T)/\lambda(0))^{-2}$) over the entire temperature range below T_c.

Since our TDR technique only measured $\Delta\lambda(T)$, we searched the literature for the value of $\lambda(0)$ in FeSe. In Fig. 5.6 the superfluid density is plotted for the $\lambda(0)$ values of 400 nm (from microwave cavity perturbation [27]) and 330 nm obtained from the best fit to the anisotropic order parameter, described in the following paragraph. The curves are not too far from each other so there is no substantial difference for the choice of $\lambda(0)$ in this spatial range. Superfluid densities for both samples A and B before and after electron irradiation are shown in Fig. 5.7. Note that both are normalized arbitrarily to 1 at $T = 0$. While it is clear that electron irradiation results in a suppressed superfluid density at all temperatures, we cannot make more rigorous conclusions, because we lack the information on how much $\lambda(0)$ increases due to electron irradiation.

To describe the data over the whole temperature range, we discuss fits using a single anisotropic order parameter as well as two isotropic gaps. Neither is really appropriate for a multiband, anisotropic superconductor but these analyses can give some sense of what properties the true gap function must display. In order to analyze the data with an anisotropic order parameter with the possibility of both gapped and nodal states, we use a convenient parametrization to separate the temperature and angular dependencies [49], $\Delta(t, \phi) = \Psi(t)\Omega(\phi)$. The temperature-dependent part, $\Psi(t)$, is obtained from the self-consistency equation [38],

$$\frac{1}{2\pi T} \ln\frac{T_c}{T} = \sum_{\omega>0}^{\infty} \left(\frac{1}{\hbar\omega} - \left\langle \frac{\Omega^2}{\sqrt{\Psi^2\Omega^2 + \hbar^2\omega^2}} \right\rangle_{FS} \right) \tag{5.1}$$

where $\hbar\omega = \pi k_B T\ (2n + 1)$ are the Matsubara frequencies and the angular part, $\Omega(\phi) = (1 + r\ \cos(4\phi))/(1 + r^2/2)^{1/2}$, is chosen as a simple representation of the gap anisotropy. In general one could choose other anisotropic harmonics (e.g., $\cos(n\phi)$) according to the symmetry of the lattice [50, 51, 52], but this would not alter the qualitative results. The angular part is normalized, $\langle\Omega^2\rangle = 1$. The fitting results of the experimental superfluid density using the set of equations above are shown in Fig. 5.6. A direct fit of the experimental $\rho_s(t)$ with $\lambda(0) = 400$ nm to this anisotropic gap can only reproduce the data roughly below $0.3T/T_c$, with $r = 0.70$. However, a small adjustment of $\lambda(0)$ to 330 nm produces a curve that can be fitted with $r = 0.75$ in the whole temperature range. The angular variation of the gap is shown in inset (a) in Fig. 5.6. A hypothetical nodal case with $r = 1.2$ is shown for comparison. For the fitting the temperature-dependent part

of the gap $\Psi(t)$ was calculated self-consistently [38] and is shown in inset (b), in comparison with the isotropic case of $r = 0$. For completeness, we also used a self-consistent two-gap γ-model [48] as shown by the dashed line in Fig. 5.6. However, due to the isotropic gaps assumption of the fit it only captures the intermediate temperatures. Nevertheless, the interaction parameters inferred from the γ-model fitting result in a positive average of the interaction matrix $\langle V \rangle > 0$, which is important for the discussion below.

5.5.3 Reconciling low temperature pair-breaking effects with T_c enhancement by irradiation

It is clearly important to reconcile the data at low temperatures (including the small gap and its enhancement due to electron irradiation) which are consistent with pair-breaking in an anisotropic s-wave state with the remarkable fact that T_c *increases* after irradiation. Note that there are several irradiations (for example by heavy ions) that produce essentially no change in T_c. These effects have been understood in terms of mesoscopic inhomogeneity, in contrast to the spatially uniform disorder produced at the nanoscale regime by electron irradiation. In pnictides (e.g. the $BaFe_2As_2$ and $CaKFe_4As_4$ series) however, T_c is suppressed fairly rapidly by 2.5 MeV electron irradiation [53, 54, 55, 56]. For example, near optimally doped K-Ba122 (Ch. 3) the same irradiation dose of 1.8 C/cm^2 suppresses T_c by $\sim$5%. On the other hand, in both the two FeSe samples presented in this work, T_c *increases* by the same amount. Hence, the effect of electron irradiation in FeSe is qualitatively different. In other words, some aspects of the defects created by electron irradiation in this system are not consistent with a purely pair-breaking interpretation. The irradiation may, for examples, effectively dope the system, exert chemical pressure, or by some other means, enhance the pairing interaction ("pair strengthening"). Another possibility is that the superconductivity in FeSe is competing with a secondary order that is suppressed more rapidly by disorder than the superconductivity itself. Theoretical studies in this area have explored scenarios of the spin-density wave [57] or the nematic [58] phases competing with superconductivity, which may result in T_c enhancement.

Before discussing each individual scenario of what might cause T_c to increase as presented above, first we need to address why the usual pair-breaking effect of disorder is rather small in FeSe. In this case there are several situations in which pair-breaking, even in a highly anisotropic superconductor, is fairly minimal. The first example is a conventional, sign-preserving s_{++} superconductor where non-magnetic disorder is pair-breaking but only to the extent that it averages the gap anisotropy [46]. However, this seems unlikely simply because the electronic interactions and the Fermi surface of FeSe are so similar to other iron pnictides, where there is considerable experimental evidence and theoretical justification for an $s_{\pm}$ identification [50, 59]. For instance, inelastic neutron scattering measurements also favor an $s_{\pm}$ gap structure in this material [22]. In this case, without any significant interband impurity scattering $s_{\pm}$ pairing is also fairly insensitive to disorder, at least as insensitive as the corresponding anisotropic s_{++}. It seems to us that this latter possibility is likely to be the case. If we compare our data to the irradiated $BaFe_2(As_{0.67}P_{0.33})_2$ [53], then the effect of pair strengthening or the competing order would have to of roughly the same order, but a bit larger, compared to the (opposite sign) effect of the disorder pair-breaking.

Now we can discuss various scenarios of the origin of the T_c enhancement. First, we find the doping scenario unlikely because we measured the Hall coefficient in other systems of superconductor and found that electron irradiation is not doping the system [56, 60]. Second, we consider the possibility that the Frenkel pairs created by electron irradiation change the lattice in away that mimics some kind of chemical pressure, thereby altering the electronic structure and the pairing interaction itself. One effect of this type is of course, the actual hydrostatic pressure where T_c is observed to increase simultaneously with the decrease of T_s, exactly as observed here [7, 8]. However, the creation of Frenkel defects should expand rather than collapse the lattice. Nevertheless, similar effects have been seen when the lattice is expanded, e.g. in the FeSe intercalate family. As pointed out by Noji *et al.* [61], expanding the lattice by intercalation in the c-direction in the range of 5-9 Å increases T_c linearly at a rate of about 14 K/Å. FeSe itself is at the bottom of this lattice constant range. This trend in the intercalates was reproduced by spin fluctuation theory with the calculated Fermi surfaces as input [62] and arises crudely due to the increase of the Fermi

level density of states as c increases. On the other hand, uniaxial thermal-expansion measurements show (via thermodynamic relations) that T_c is mostly affected by the in-plane lattice parameters a and b, and is much less sensitive to the c-axis lattice constant [37]. In either case, our estimates of the average stretch of the c-axis lattice constant with irradiation provide an effect that is an order of magnitude too small to influence T_c via chemical pressure mechanism compared to the 5% enhancement observed. With our irradiation dose, we create approximately 3.6 x 10^{-3} Frenkel pairs per unit cell and even the most optimistic estimates give a minuscule volume change in the order of the Frenkel pair density $\Delta V/V_0 \lesssim 10^{-3}$, which at best, can result in about 0.1 K change of T_c for any optimistic scenario of either expansion of the c-axis or hydrostatic pressure. So we may safely conclude that pressure due to electron irradiation is not sufficient to explain our results.

For the competing orders scenario, in FeSe there appears to be no long range magnetic order in ambient pressure but a significant nematic order is present due to the weak orthorhombic distortion below the structural transition. The assumption of a competition between the two states appears reasonable because T_s is suppressed while T_c is enhanced, both under hydrostatic pressure [7, 8] and S/Te doping [63, 64]. Mishra and Hirschfeld [58] have shown that under plausible conditions (i.e. multiband character and strong initial nematicity, among other things), disorder may suppress the nematic order and allow T_c to rise. However, several experimental pressure studies uncovered a nearby magnetic instability [7, 8, 65] which suggests that there might be a more complex interplay between the competing nematic, magnetic and superconducting orders as revealed in the phase diagram [7, 65].

The relationship between the superconducting and magnetic phases is also the key point in the discussion of the final scenario of pair strengthening. We discuss the possibility that the impurity is pair strengthening i.e., that it enhances the pair interaction locally as discussed in several microscopic models [66, 67, 68, 69]. Here, the basic idea is that the electronic structure is modulated locally so that it enhances the spin fluctuations when the system is already near a magnetic transition. Note that the impurity can, at the same time, possess an electrostatic potential component that is itself pair-breaking so the competition between these two effects decides whether

T_c is enhanced locally or not. As discussed in the Ch. 5.3 for the concentration of defects estimated in our irradiated sample, the defects are (on average) well within a coherence length of one another so there is a percolating superconducting path at the enhanced T_c, such that it can be detected in transport. The broadening of the transition by irradiation tends to support an inhomogeneous enhancement of this type. Note that since the above theoretical works considered only Hubbard-type single-band models in cuprates, considerable further work is necessary to establish the validity of this scenario in the context of the iron-based materials.

5.6 Summary and Conclusions

FeSe presents a unique opportunity to study bulk superconductivity in relation to a strong nematic phase with the absence of a long-range magnetic ordering in ambient pressure. However, experiments in pressure dependence [7, 8, 65] and inelastic neutron scattering [22] showed that a long-range magnetic phase may still be playing a relevant role or even competing with the other two phases. Using electron irradiation, we showed that superconductivity has a complex interplay with nematicity (and possibly magnetism), which is coupled to the structural tetragonal $\rightarrow$ orthorhombic transition. With 1.8 C/cm^2 dose of 2.5 MeV electron irradiation, we observed T_c enhancement by $\sim$0.4 K and T_s suppression by $\sim$0.9 K. At present, we narrow down the possible scenarios for the T_c enhancement to (i) the competition between superconductivity and nematicity where disorder suppresses the nematic order faster [58], (ii) the induced disorder enhancing the local spin fluctuations which strengthen Cooper pairing [66, 67, 68, 69], or (iii) a combination of both.

After our work in 2016, Mizukami *et al.* in 2017 reported a T_c enhancement in underdoped P-Ba122 system due to electron irradiation [70]. They explained the T_c increase as an effective shift of the T vs doping phase diagram as the critical point is suppressed to lower P composition by irradiation. The shift is due solely to scattering effects without any effective doping in the material, which is similarly observed by our group [56, 60]. It seems that this framework might essentially capture the same mechanisms and is fully compatible with the previous discussion in the Analysis section.

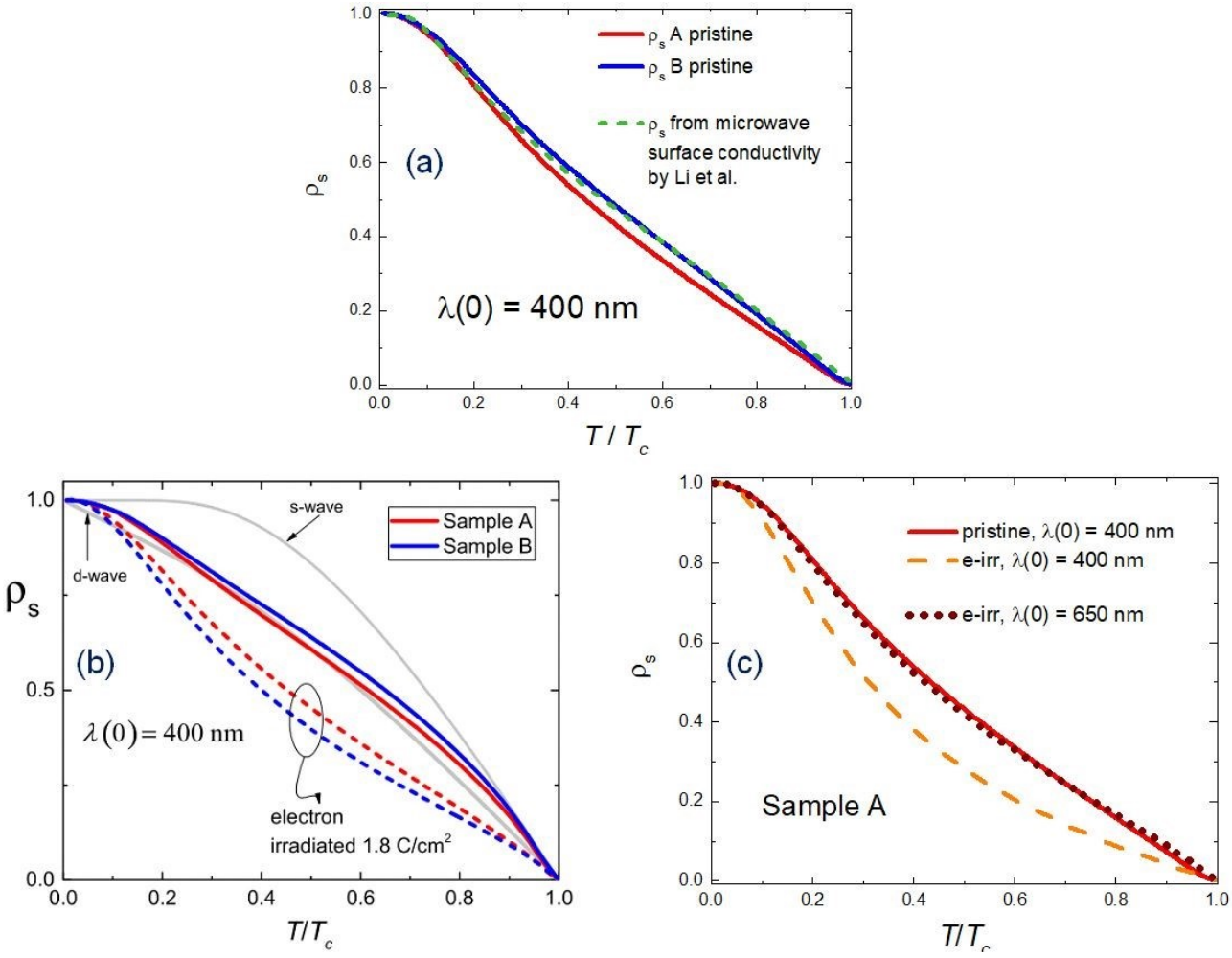

Figure 5.7 (a) The superfluid densities $\rho_s(t)$ of the pristine samples A and B (with corrected calibration, solid lines) compared to the sample in [35] (dashed line). We observe a reasonable agreement between the two experiments on the reported gap structure parameters. (b) $\rho_s(t)$ before (solid lines) and after (dashed lines) 1.8 C/cm^2 2.5 MeV electron irradiation for samples A and B. Solid grey lines show standard $s-$ and $d-$ wave curves for comparison. $\lambda(0) = 400$ nm was taken from [27]. (c) When $\lambda(0)$ is taken as 650 nm after irradiation, the overall pristine behavior of the superfluid density curve for sample A is restored, suggesting a robust gap structure against electron irradiation. (b) From Ref. [5] Supplemental Materials.

We showed that FeSe has a gap structure that is highly anisotropic in the *ab*-plane while the *c*-axis anisotropy is relatively low, as shown by the low temperature behavior of the London penetration depth data and the power-law fit (Fig. 5.4). The gap minima opens with disorder (Fig. 5.5(b)), consistent with the suggestion that cleaner samples exhibit nodal behavior [20, 33]. Therefore, we can immediately rule out *d*-wave symmetry since the nodes are not protected. Overall, the gap symmetry is consistent with an extended (anisotropic) *s*-wave model [31, 33, 35]. Li *et al.* [35] used anisotropic two-band model to fit their superfluid density curve which has a temperature dependence very close to ours, with the corrected calibration (Fig. 5.7(a)). Therefore, their estimates of the gap anisotropies ($r_1 = 0, r_2 = 0.6$) and the gap magnitudes ($\Delta_1/\Delta_2 \approx 8, \Delta_2/T_c \approx 0.25$) [35] are also fully compatible with our data. Interestingly, the (larger) gap magnitude and the (smaller) gap anisotropy values are not too far from the parameter values obtained from our single anisotropic order parameter fitting that was performed in the original paper [5] (Fig. 5.6 insets). Knowing that our original fitting still turns out to be a useful approximation, this recovers some validity back to our fitting results and procedures.

We also showed that the order parameter in FeSe is quite robust with disorder because it needs to overcome the pair-breaking effect of electron irradiation and yield T_c enhancement. We will show that the robustness against disorder is also reinforced by the shape of the superfluid density curve after irradiation. Fig. 5.7(b) shows the superfluid density curves of both samples before and after irradiation. If we assume a constant $\lambda(0) = 400$ nm, irradiation seems to significantly reduce the density of Cooper pairs in the whole temperature range. However, we expect $\lambda(0)$ to also increase due to irradiation which will minimize the difference between the pristine and irradiated states. Indeed, by plotting the irradiated state with $\lambda(0) = 650$ nm we are able to recover the overall pristine behavior of the superfluid density curve (Fig. 5.7(c)). While at present we have little justification for taking $\lambda(0) = 650$ nm, only by the fact that the behavior of $\rho_s(t)$ can be recovered in the whole temperature range simply by adjusting a single parameter is quite remarkable. It is yet another piece of evidence in favor of the insensitivity of FeSe order parameter to disorder. Lastly, our data is consistent with $s_{\pm}$-pairing (with no significant interband scattering) which is

insensitive to non-magnetic disorder and is supported by considerable experimental evidence and theoretical justification in the literature over s_{++} [21, 22, 50].

5.7 References

[1] M. D. Watson, T. K. Kim, A. A. Haghighirad, S. F. Blake, N. R. Davies, M. Hoesch, T. Wolf, and A. I. Coldea. Suppression of orbital ordering by chemical pressure in fese$_{1-x}$s$_x$. *Phys. Rev. B*, 92:121108, Sep 2015.

[2] Li Xiang, Udhara S. Kaluarachchi, Anna E. Böhmer, Valentin Taufour, Makariy A. Tanatar, Ruslan Prozorov, Sergey L. Bud'ko, and Paul C. Canfield. Dome of magnetic order inside the nematic phase of sulfur-substituted fese under pressure. *Phys. Rev. B*, 96:024511, Jul 2017.

[3] Naoyuki Katayama, Sungdae Ji, Despina Louca, Seunghun Lee, Masaki Fujita, Taku J Sato, Jinsheng Wen, Zhijun Xu, Genda Gu, Guangyong Xu, Ziwei Lin, Masanori Enoki, Sung Chang, Kazuyoshi Yamada, and John M Tranquada. Investigation of the Spin-Glass Regime between the Antiferromagnetic and Superconducting Phases in Fe 1y Se x Te 1Àx. *Journal of the Physical Society of Japan*, 79(11):113702, 2010.

[4] J. S. Kim, D. VanGennep, J. J. Hamlin, X. Wang, A. S. Sefat, and G. R. Stewart. Unusual effects of be doping in the iron based superconductor fese, 2018.

[5] S Teknowijoyo, K Cho, M A Tanatar, J Gonzales, A E Böhmer, O Cavani, V Mishra, P J Hirschfeld, S L Bud 'ko, P C Canfield, and R Prozorov. Enhancement of superconducting transition temperature by pointlike disorder and anisotropic energy gap in FeSe single crystals Enhancement of superconducting transition temperature by point-like disorder and anisotropic energy gap in FeSe single crystals. 2016.

[6] P. Reiss, M. D. Watson, T. K. Kim, A. A. Haghighirad, D. N. Woodruff, M. Bruma, S. J. Clarke, and A. I. Coldea. Suppression of electronic correlations by chemical pressure from fese to fes. *Phys. Rev. B*, 96:121103, Sep 2017.

[7] K. Kothapalli, A. E. Böhmer, W. T. Jayasekara, B. G. Ueland, P. Das, A. Sapkota, V. Taufour, Y. Xiao, E. Alp, S. L. Bud'ko, P. C. Canfield, A. Kreyssig, and A. I. Goldman. Strong cooperative coupling of pressure-induced magnetic order and nematicity in FeSe. *Nature Communications*, 7:12728, sep 2016.

[8] Udhara S. Kaluarachchi, Valentin Taufour, Anna E. Böhmer, Makariy A. Tanatar, Sergey L. Bud'ko, Vladimir G. Kogan, Ruslan Prozorov, and Paul C. Canfield. Nonmonotonic pressure evolution of the upper critical field in superconducting fese. *Phys. Rev. B*, 93:064503, Feb 2016.

[9] Jian-Feng Ge, Zhi-Long Liu, Canhua Liu, Chun-Lei Gao, Dong Qian, Qi-Kun Xue, Ying Liu, and Jin-Feng Jia. Superconductivity above 100 K in single-layer FeSe films on doped SrTiO 3. *Nature Materials*, 14(3):285–289, mar 2015.

[10] Shaolong He, Junfeng He, Wenhao Zhang, Lin Zhao, Defa Liu, Xu Liu, Daixiang Mou, Yun-Bo Ou, Qing-Yan Wang, Zhi Li, Lili Wang, Yingying Peng, Yan Liu, Chaoyu Chen, Li Yu, Guodong Liu, Xiaoli Dong, Jun Zhang, Chuangtian Chen, Zuyan Xu, Xi Chen, Xucun Ma, Qikun Xue, and X J Zhou. Phase diagram and electronic indication of high-temperature superconductivity at 65 K in single-layer FeSe films. *Nature Materials*, 12:26, 2013.

[11] Xu Liu, Lin Zhao, Shaolong He, Junfeng He, Defa Liu, Daixiang Mou, Bing Shen, Yong Hu, Jianwei Huang, and X J Zhou. Electronic structure and superconductivity of fese-related superconductors. *Journal of Physics: Condensed Matter*, 27(18):183201, 2015.

[12] Dennis Huang and Jennifer E. Hoffman. Monolayer fese on srtio3. *Annual Review of Condensed Matter Physics*, 8(1):311–336, 2017.

[13] Fong-Chi Hsu, Jiu-Yong Luo, Kuo-Wei Yeh, Ta-Kun Chen, Tzu-Wen Huang, Phillip M. Wu, Yong-Chi Lee, Yi-Lin Huang, Yan-Yi Chu, Der-Chung Yan, and Maw-Kuen Wu. Superconductivity in the pbo-type structure -fese. *Proceedings of the National Academy of Sciences*, 105(38):14262–14264, 2008.

[14] M. A. Tanatar, A. E. Böhmer, E. I. Timmons, M. Schütt, G. Drachuck, V. Taufour, K. Kothapalli, A. Kreyssig, S. L. Bud'ko, P. C. Canfield, R. M. Fernandes, and R. Prozorov. Origin of the resistivity anisotropy in the nematic phase of fese. *Phys. Rev. Lett.*, 117:127001, Sep 2016.

[15] Fa Wang, Steven A. Kivelson, and Dung-Hai Lee. Nematicity and quantum paramagnetism in FeSe. *Nature Physics*, 11(11):959–963, sep 2015.

[16] J. K. Glasbrenner, I. I. Mazin, Harald O. Jeschke, P. J. Hirschfeld, R. M. Fernandes, and Roser Valentí. Effect of magnetic frustration on nematicity and superconductivity in iron chalcogenides. *Nature Physics*, 11(11):953–958, aug 2015.

[17] Youichi Yamakawa, Seiichiro Onari, and Hiroshi Kontani. Nematicity and magnetism in fese and other families of fe-based superconductors. *Phys. Rev. X*, 6:021032, Jun 2016.

[18] Andrey V. Chubukov, M. Khodas, and Rafael M. Fernandes. Magnetism, superconductivity, and spontaneous orbital order in iron-based superconductors: Which comes first and why? *Phys. Rev. X*, 6:041045, Dec 2016.

[19] Defa Liu, Cong Li, Jianwei Huang, Bin Lei, Le Wang, Xianxin Wu, Bing Shen, Qiang Gao, Yuxiao Zhang, Xu Liu, Yong Hu, Yu Xu, Aiji Liang, Jing Liu, Ping Ai, Lin Zhao, Shaolong He, Li Yu, Guodong Liu, Yiyuan Mao, Xiaoli Dong, Xiaowen Jia, Fengfeng Zhang, Shenjin Zhang, Feng Yang, Zhimin Wang, Qinjun Peng, Youguo Shi, Jiangping Hu, Tao Xiang, Xianhui

Chen, Zuyan Xu, Chuangtian Chen, and X J Zhou. Orbital Origin of Extremely Anisotropic Superconducting Gap in Nematic Phase of FeSe Superconductor. 2018.

[20] Yue Sun, Shunichiro Kittaka, Shota Nakamura, Toshiro Sakakibara, Peng Zhang, Shik Shin, Koki Irie, Takuya Nomoto, Kazushige Machida, Jingting Chen, and Tsuyoshi Tamegai. Disorder-sensitive nodelike small gap in FeSe. *Physical Review B*, 98, 2018.

[21] P. S. Wang, S. S. Sun, Y. Cui, W. H. Song, T. R. Li, Rong Yu, Hechang Lei, and Weiqiang Yu. Pressure induced stripe-order antiferromagnetism and first-order phase transition in fese. *Phys. Rev. Lett.*, 117:237001, Nov 2016.

[22] Qisi Wang, Yao Shen, Bingying Pan, Xiaowen Zhang, K. Ikeuchi, K. Iida, A. D. Christianson, H. C. Walker, D. T. Adroja, M. Abdel-Hafiez, Xiaojia Chen, D. A. Chareev, A. N. Vasiliev, and Jun Zhao. Magnetic ground state of FeSe. *Nature Communications*, 7:12182, jul 2016.

[23] Peayush Choubey, T. Berlijn, A. Kreisel, C. Cao, and P. J. Hirschfeld. Visualization of atomic-scale phenomena in superconductors: Application to fese. *Phys. Rev. B*, 90:134520, Oct 2014.

[24] A. Kreisel, Shantanu Mukherjee, P. J. Hirschfeld, and Brian M. Andersen. Spin excitations in a model of fese with orbital ordering. *Phys. Rev. B*, 92:224515, Dec 2015.

[25] Shantanu Mukherjee, A. Kreisel, P. J. Hirschfeld, and Brian M. Andersen. Model of electronic structure and superconductivity in orbitally ordered fese. *Phys. Rev. Lett.*, 115:026402, Jul 2015.

[26] Can-Li Song, Yi-Lin Wang, Peng Cheng, Ye-Ping Jiang, Wei Li, Tong Zhang, Zhi Li, Ke He, Lili Wang, Jin-Feng Jia, Hsiang-Hsuan Hung, Congjun Wu, Xucun Ma, Xi Chen, and Qi-Kun Xue. Direct observation of nodes and twofold symmetry in fese superconductor. *Science*, 332(6036):1410–1413, 2011.

[27] Shigeru Kasahara, Tatsuya Watashige, Tetsuo Hanaguri, Yuhki Kohsaka, Takuya Yamashita, Yusuke Shimoyama, Yuta Mizukami, Ryota Endo, Hiroaki Ikeda, Kazushi Aoyama, Taichi Terashima, Shinya Uji, Thomas Wolf, Hilbert von Löhneysen, Takasada Shibauchi, and Yuji Matsuda. Field-induced superconducting phase of fese in the bcs-bec cross-over. *Proceedings of the National Academy of Sciences*, 111(46):16309–16313, 2014.

[28] M Abdel-Hafiez, Y J Pu, J Brisbois, R Peng, D L Feng, D A Chareev, A V Silhanek, C Krellner, A N Vasiliev, and X.-J Chen. Impurity scattering effects on the superconducting properties and the tetragonal-to-orthorhombic phase transition in FeSe. Technical report.

[29] J.-Y. Lin, Y. S. Hsieh, D. A. Chareev, A. N. Vasiliev, Y. Parsons, and H. D. Yang. Coexistence of isotropic and extended s-wave order parameters in fese as revealed by low-temperature specific heat. *Phys. Rev. B*, 84:220507, Dec 2011.

[30] Lin Jiao, Chien-Lung Huang, Sahana Rößler, Cevriye Koz, Ulrich K. Rößler, Ulrich Schwarz, and Steffen Wirth. Superconducting gap structure of FeSe. *Scientific Reports*, 7(1):44024, dec 2017.

[31] A.V. Muratov, A.V. Sadakov, S.Yu. Gavrilkin, A.R. Prishchepa, G.S. Epifanova, D.A. Chareev, and V.M. Pudalov. Specific heat of FeSe: Two gaps with different anisotropy in superconducting state. *Physica B: Condensed Matter*, 536:785–789, may 2018.

[32] J. K. Dong, T. Y. Guan, S. Y. Zhou, X. Qiu, L. Ding, C. Zhang, U. Patel, Z. L. Xiao, and S. Y. Li. Multigap nodeless superconductivity in fese$_x$: Evidence from quasiparticle heat transport. *Phys. Rev. B*, 80:024518, Jul 2009.

[33] P. Bourgeois-Hope, S. Chi, D. A. Bonn, R. Liang, W. N. Hardy, T. Wolf, C. Meingast, N. Doiron-Leyraud, and Louis Taillefer. Thermal Conductivity of the Iron-Based Superconductor FeSe: Nodeless Gap with a Strong Two-Band Character. *Physical Review Letters*, 117(9):1–5, 2016.

[34] T. Watashige, Y. Tsutsumi, T. Hanaguri, Y. Kohsaka, S. Kasahara, A. Furusaki, M. Sigrist, C. Meingast, T. Wolf, H. v. Löhneysen, T. Shibauchi, and Y. Matsuda. Evidence for time-reversal symmetry breaking of the superconducting state near twin-boundary interfaces in fese revealed by scanning tunneling spectroscopy. *Phys. Rev. X*, 5:031022, Aug 2015.

[35] Meng Li, N. R. Lee-Hone, Shun Chi, Ruixing Liang, W. N. Hardy, D. A. Bonn, E. Girt, and D. M. Broun. Superfluid density and microwave conductivity of FeSe superconductor: Ultra-long-lived quasiparticles and extended s-wave energy gap. *New Journal of Physics*, 18(8):1–8, 2016.

[36] Defa Liu, Wenhao Zhang, Daixiang Mou, Junfeng He, Yun-Bo Ou, Qing-Yan Wang, Zhi Li, Lili Wang, Lin Zhao, Shaolong He, Yingying Peng, Xu Liu, Chaoyu Chen, Li Yu, Guodong Liu, Xiaoli Dong, Jun Zhang, Chuangtian Chen, Zuyan Xu, Jiangping Hu, Xi Chen, Xucun Ma, Qikun Xue, and X.J. Zhou. Electronic origin of high-temperature superconductivity in single-layer FeSe superconductor. *Nature Communications*, 3(1):931, jan 2012.

[37] A. E. Böhmer, F. Hardy, F. Eilers, D. Ernst, P. Adelmann, P. Schweiss, T. Wolf, and C. Meingast. Lack of coupling between superconductivity and orthorhombic distortion in stoichiometric single-crystalline fese. *Phys. Rev. B*, 87:180505, May 2013.

[38] R Prozorov and V G Kogan. London penetration depth in iron-based superconductors. *Reports on Progress in Physics*, 74(12):124505, 2011.

[39] C. Martin, H. Kim, R. T. Gordon, N. Ni, V. G. Kogan, S. L. Bud'ko, P. C. Canfield, M. A. Tanatar, and R. Prozorov. Evidence from anisotropic penetration depth for a three-dimensional nodal superconducting gap in single-crystalline $Ba(Fe_{1-x}Ni_x)_2as_2$. *Phys. Rev. B*, 81:060505, Feb 2010.

[40] P. Rodière, J. P. Brison, A. D. Huxley, F. Rullier Albenque, and J. Flouquet. Characterization of high energy electron irradiation damage in upt3 samples. *Journal of Low Temperature Physics*, 132(1):119–134, Jul 2003.

[41] M.J. Berger, J.S. Coursey, M.A. Zucker, and J. Chang. Stopping-power and range tables for electrons, protons, and helium ions. https://www.nist.gov/pml/stopping-power-range-tables-electrons-protons-and-helium-ions.

[42] Calculations of cross - sections by electron irradiation. According to O. S. Oen (1965, 1973), C code by Daniel Lesueur, restored by Francois Beuneu. Ecole Polytechnique, Palaiseau, France, 1973.

[43] A.C. Damask and G.J. Dienes. *Point Defects in Metals*. Gordon and Breach Science, 1963.

[44] M. W. Thompson. *Defects and Radiation Damage in Metals*. September 1974.

[45] Taichi Terashima, Naoki Kikugawa, Andhika Kiswandhi, Eun-Sang Choi, James S. Brooks, Shigeru Kasahara, Tatsuya Watashige, Hiroaki Ikeda, Takasada Shibauchi, Yuji Matsuda, Thomas Wolf, Anna E. Böhmer, Frédéric Hardy, Christoph Meingast, Hilbert v. Löhneysen, Michi-To Suzuki, Ryotaro Arita, and Shinya Uji. Anomalous fermi surface in fese seen by shubnikov–de haas oscillation measurements. *Phys. Rev. B*, 90:144517, Oct 2014.

[46] David Markowitz and Leo P. Kadanoff. Effect of impurities upon critical temperature of anisotropic superconductors. *Phys. Rev.*, 131:563–575, Jul 1963.

[47] V. Mishra, G. R. Boyd, S. Graser, T. Maier, P. J. Hirschfeld, and D. J. Scalapino. Lifting of nodes by disorder in extended-s-state superconductors: Application to ferropnictides. *Phys. Rev. B*, 79:094512, Mar 2009.

[48] V. G. Kogan, C. Martin, and R. Prozorov. Superfluid density and specific heat within a self-consistent scheme for a two-band superconductor. *Phys. Rev. B*, 80:014507, Jul 2009.

[49] V. G. Kogan. Pair breaking in iron pnictides. *Phys. Rev. B*, 80:214532, Dec 2009.

[50] P. J. Hirschfeld. Erratum: Corrigendum to Using gap symmetry and structure to reveal the pairing mechanism in Fe-based superconductors (Comptes Rendus Physique (2016) 17(1-2) (197231)(S1631070515001693)(10.1016/j.crhy.2015.10.002)). *Comptes Rendus Physique*, 17(7):803, 2016.

[51] Andrey Chubukov and Peter J. Hirschfeld. Iron-based superconductors, seven years later. *Physics Today*, 68(6):46–52, jun 2015.

[52] Andrey Chubukov. Pairing Mechanism in Fe-Based Superconductors. *Annu. Rev. Condens. Matter Phys*, 3:57–92, 2012.

[53] Y. Mizukami, M. Konczykowski, Y. Kawamoto, S. Kurata, S. Kasahara, K. Hashimoto, V. Mishra, A. Kreisel, Y. Wang, P. J. Hirschfeld, Y. Matsuda, and T. Shibauchi. Disorder-induced topological change of the superconducting gap structure in iron pnictides. *Nature Communications*, 5:5657, nov 2014.

[54] S. Teknowijoyo, K. Cho, M. Kończykowski, E. I. Timmons, M. A. Tanatar, W. R. Meier, M. Xu, S. L. Bud'ko, P. C. Canfield, and R. Prozorov. Robust $s_{\pm}$ pairing in $CaK(Fe_{1-x}Ni_x)_4as_4$ ($x = 0$ and 0.05) from the response to electron irradiation. *Phys. Rev. B*, 97:140508, Apr 2018.

[55] K. Cho, M. Konczykowski, S. Teknowijoyo, M. A. Tanatar, Y. Liu, T. A. Lograsso, W. E. Straszheim, V. Mishra, S. Maiti, P. J. Hirschfeld, and R. Prozorov. Energy gap evolution across the superconductivity dome in single crystals of (Ba1-xKx)Fe2As2. *Science Advances*, 2(9):e1600807–e1600807, 2016.

[56] R Prozorov, M Kończykowski, M A Tanatar, A Thaler, S L Bud'ko, P C Canfield, V Mishra, and P J Hirschfeld. Effect of Electron Irradiation on Superconductivity in Single Crystals of BaFe 1x Ru x 2 As 2 (x 0.24).

[57] R. M. Fernandes, M. G. Vavilov, and A. V. Chubukov. Enhancement of T_c by disorder in underdoped iron pnictide superconductors. *Phys. Rev. B*, 85:140512, Apr 2012.

[58] V Mishra and P J Hirschfeld. Effect of disorder on the competition between nematic and superconducting order in fese. *New Journal of Physics*, 18(10):103001, 2016.

[59] Yunkyu Bang and G. R. Stewart. Superconducting properties of the s -wave state: Fe-based superconductors. *Journal of Physics: Condensed Matter*, 29(12):123003, 2017.

[60] Kyuil Cho, M. Kończykowski, S. Teknowijoyo, M. A. Tanatar, J. Guss, P. B. Gartin, J. M. Wilde, A. Kreyssig, R. J. McQueeney, A. I. Goldman, V. Mishra, P. J. Hirschfeld, and R. Prozorov. Using controlled disorder to probe the interplay between charge order and superconductivity in NbSe2. *Nature Communications*, 9(1):2796, dec 2018.

[61] Takashi Noji, Takehiro Hatakeda, Shohei Hosono, Takayuki Kawamata, Masatsune Kato, and Yoji Koike. Synthesis and post-annealing effects of alkaline-metal-ethylenediamine-intercalated superconductors A x (C 2 H 8 N 2) y Fe 2Àz Se 2 (A = Li, Na) with T c = 45 K. 2014.

[62] Daniel Guterding, Harald O. Jeschke, P. J. Hirschfeld, and Roser Valentí. Unified picture of the doping dependence of superconducting transition temperatures in alkali metal/ammonia intercalated fese. *Phys. Rev. B*, 91:041112, Jan 2015.

[63] Mahmoud Abdel-Hafiez, Yuan-Yuan Zhang, Zi-Yu Cao, Chun-Gang Duan, G. Karapetrov, V. M. Pudalov, V. A. Vlasenko, A. V. Sadakov, D. A. Knyazev, T. A. Romanova, D. A. Chareev, O. S. Volkova, A. N. Vasiliev, and Xiao-Jia Chen. Superconducting properties of sulfur-doped iron selenide. *Physical Review B - Condensed Matter and Materials Physics*, 91(16), 4 2015.

[64] Yoshikazu Mizuguchi and Yoshihiko Takano. Review of fe chalcogenides as the simplest fe-based superconductor. *Journal of the Physical Society of Japan*, 79(10):102001, 2010.

[65] J. P. Sun, K. Matsuura, G. Z. Ye, Y. Mizukami, M. Shimozawa, K. Matsubayashi, M. Yamashita, T. Watashige, S. Kasahara, Y. Matsuda, J. Q. Yan, B. C. Sales, Y. Uwatoko, J. G. Cheng, and T. Shibauchi. Dome-shaped magnetic order competing with high-temperature superconductivity at high pressures in FeSe. *Nature Communications*, 7:12146, jul 2016.

[66] Tamara S. Nunner, Brian M. Andersen, Ashot Melikyan, and P. J. Hirschfeld. Dopant-modulated pair interaction in cuprate superconductors. *Phys. Rev. Lett.*, 95:177003, Oct 2005.

[67] Maciej M. Maśka, Żaneta Śledź, Katarzyna Czajka, and Marcin Mierzejewski. Inhomogeneity-induced enhancement of the pairing interaction in cuprate superconductors. *Phys. Rev. Lett.*, 99:147006, Oct 2007.

[68] Kateryna Foyevtsova, Roser Valentí, and P. J. Hirschfeld. Effect of dopant atoms on local superexchange in cuprate superconductors: A perturbative treatment. *Phys. Rev. B*, 79:144424, Apr 2009.

[69] A. T. Rømer, S. Graser, T. S. Nunner, P. J. Hirschfeld, and B. M. Andersen. Local modulations of the spin-fluctuation-mediated pairing interaction by impurities in d-wave superconductors. *Phys. Rev. B*, 86:054507, Aug 2012.

[70] Yuta Mizukami, Marcin Konczykowski, Kohei Matsuura, Tatsuya Watashige, Shigeru Kasahara, Yuji Matsuda, and Takasada Shibauchi. Impact of disorder on the superconducting phase diagram in bafe2(as1xpx)2. *Journal of the Physical Society of Japan*, 86(8):083706, 2017.

CHAPTER 6. GENERAL CONCLUSION

In this final chapter, I will review and summarize the main points of the dissertation, which is about using the combination of London penetration depth and electron irradiation to study iron-based superconductors.

6.1 London Penetration Depth

The measurement of London penetration depth allows us to access the density of states in the superconducting phase. Essentially it is probing the structure and symmetry of the gapped Fermi surface of the superconductor. With our TDR method, what we get is the global average of the gap structure with the choice of in-plane or out-of-plane orientation for the perturbing magnetic field, along with the access to dilution refrigerator temperatures, and a remarkable parts-per-billion sensitivity. However, it is not trivial to measure the absolute value of the penetration depth. The aluminum coating method [1, 2] or a combination with other sensing techniques (such as the NV [3]) is required to address this problem.

The low temperature behavior ($t \equiv T/T_c \leq 0.3$) is the region of interest if one wants to extract the insight about the gap structure. As a simple approach the data of $\Delta\lambda(t)$ can be fitted with a power-law T^n with a variable upper fitting range. It is rather trivial to deduce the presence/absence of nodes if the material belongs to the ends of the spectrum, with one end having $n \approx 1$ (nodal) and the other end having $n \geq 3$ (full gap). However, for the cases in between it might not be as straightforward to infer about the gap structure from the data. Impurities, gap anisotropy and the multiband character in iron-based superconductors may affect the exponent independently. As another simple analysis, the single gap BCS fitting may give an estimate of the gap minima. Both of these simple tools can give an experimentalist a sense about the anisotropy in the material. However, in some cases it is desirable to go beyond these simple approaches, which means fitting the

$\Delta\lambda(t)$ and $\rho_s(t)$ using a more sophisticated theoretical model. Some of such theoretical approaches were already presented in the analysis of previous chapters. The assumptions and the possible obtainable information from the models are summarized below.

6.1.1 Different fitting schemes for $\Delta\lambda(t)$

For some simpler materials it may be sufficient to describe the system using a numerical approach of solving the self-consistent equation for a single anisotropic band model [1]. This was performed in the FeSe study (Ch. 5) to get an estimate of the overall gap anisotropy and magnitude. While the assumption of a single order parameter would not capture all the physics in FeSe, it turns out that the results give a reasonable agreement to the more sophisticated treatment of the anisotropic two-band approach reported elsewhere in the literature [4].

To better capture the multiband nature of iron-based superconductors, the γ-model [1, 5] can be employed. The model assumes two isotropic order parameters in the weak-coupling limit. Since many iron-based superconductors display effective two-band character that is fairly isotropic, this model becomes a reasonable option to calculate the temperature dependence of the order parameters. In Ch. 4 this method was used for the $CaKFe_4As_4$ system and the results are in good agreement with the STM data. It was also used to fit FeSe $\rho_s(t)$ data in Ch. 5. However, since FeSe has a significant anisotropy the fitting was only reasonable in the intermediate temperature range. Compared to the single anisotropic band fitting, some of the additional parameters in the γ-model include the inband/interband coupling parameters and the densities of states for each band.

Lastly, in Ch. 3 we took into account the role of three different bands (but we only calculated the pairing interaction between two anisotropic bands at all times) involving a self-consistent T-matrix calculation, in collaboration with Vivek Mishra and Peter Hirschfeld. Since in general an iron-based superconductor might have five or more bands crossing the Fermi surface, this model is arguably one of the most realistic approaches so far. However, in order to use it for studying iron-based superconductors it involves many parameters and the calculations become fairly complicated. Within this framework we were able to obtain the gap magnitudes and anisotropies in the over-

doped K-$BaFe_2As_2$, which gives a natural explanation for the development of the accidental nodes across the Lifshitz transition. Regarding the parameters, on top of the inband/interband coupling parameters and the densities of states for each band (like the γ-model) the T-matrix fitting also takes into account the anisotropy of each band, and the tunable intraband/interband (impurity) scattering strengths.

6.2 Electron Irradiation

With all the tools above in our disposal, what further information might we gain from doing electron irradiation? With such sophisticated theoretical models that employ many free parameters, pretty much all the experimental data can be fitted and described perfectly, right? Actually, having too much degrees of freedom could be seen as a disadvantage rather than an advantage when we are trying to understand the physics of the unknowns such the mechanism behind the unconventional superconductors. When the realm of possibilities is too wide, it could be difficult to construct a precise and convincing theory because of the *a priori* assumptions may not be readily justifiable. It would be more desirable if some of the free parameters can be determined experimentally (or at least somewhat constrained). And here is where electron irradiation might be useful; as an additional experimental constraint on a few of the otherwise free parameters, which makes the proposed explanation more convincing.

In particular, the point-like disorder induced by the electron irradiation would enhance the impurity scattering and the pair-breaking strengths in the gap function, which may contain a significant anisotropy and/or sign change between bands. One of the most evident effects of such effects is the suppression of T_c. In other words, the rate of T_c suppression upon increase of disorder can be experimentally obtained when plotted against irradiation dose (or $\Delta\rho_0$), which puts constraints on the inband/interband coupling and scattering strength parameters in the theoretical model.

As an example, the exponential behavior of $\Delta\lambda(t)$ at low temperature might signal either s_{++} or $s_{\pm}$ symmetry for a given superconductor. However, a rapid T_c suppression upon electron irradiation

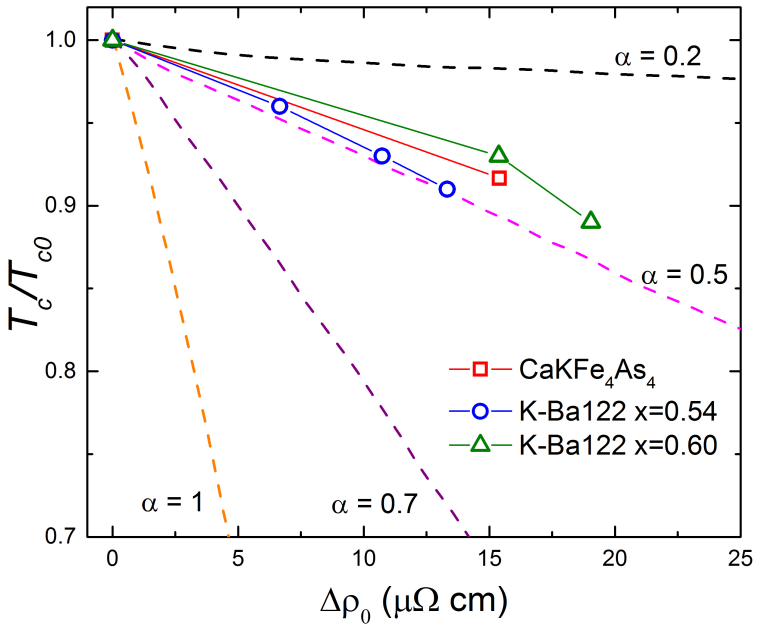

Figure 6.1 The T_c suppression upon the increase of residual resistivity, comparing the theoretical predictions with the experimental observations. The pristine superconducting critical temperature and residual resistivity,(T_c, ρ_0), for $CaKFe_4As_4$ are (35.3 K, 24.6 $\mu\Omega$ cm), $Ba_{0.46}K_{0.54}Fe_2As_2$ are (33 K, 70.7 $\mu\Omega$ cm) and $Ba_{0.4}K_{0.6}Fe_2As_2$ are (29.1 K, 52.4 $\mu\Omega$ cm). The experimental data are adapted from [6, 7] and the theoretically predicted rates are adapted from Ref. [8].

is harder to reconcile with the s_{++} scenario which requires somewhat an extreme case of anisotropy (while still keeping nodeless) and/or a huge difference in the magnitudes of the order parameters. It is more natural to explain the situation in the $s_{\pm}$ paradigm where the order parameters have different signs and thus more susceptible to non-magnetic impurity scattering.

As a step further, the precise rate of the T_c suppression can be taken from the experimental data and compared to the predicted rate from a specific theoretical model. Fig. 6.1 shows an example of such comparison where we plotted the T_c suppression in $Ba_{1-x}K_xFe_2As_2$ ($x = 0.54$, 0.60) and $CaKFe_4As_4$ side by side to the predicted T_c suppression rate calculated by Wang *et al.* [8]. The T_c suppression rates shown here were calculated for the $s_{\pm}$ pairing interactions between two (hole and electron) isotropic bands which can reasonably describe the observed gap structure of the three chosen material compositions (see Ch. 3 and 4). Within their assumptions and parameters, Wang

et al. did a T-matrix calculation on the different T_c suppression rates upon the increase of residual resistivity with different ratios of the interband to intraband scattering strengths α. Fig. 6.1 shows that the experimentally obtained suppression rates are consistent with the prediction for the ratio of $\alpha \approx 0.5$. This is quite similar to our own T-matrix fitting from Ch. 3, where the best fit was obtained with the scattering ratio of 0.6 for the compositions between $0.4 \leq x \leq 0.8$. This agreement adds more confidence and justification to our K-Ba122 picture presented in Ch. 3. While this comparison does not necessarily *prove* that $Ba_{1-x}K_xFe_2As_2$ ($x = 0.54$, 0.60) and $CaKFe_4As_4$ have $s_\pm$ pairing symmetry, it makes the $s_\pm$ scenario look very *plausible*.

Finally, beyond the systems that have been presented here can we extend the $s_\pm$ scenario to *all* other iron-based superconductor systems? The case could certainly be made considering the similarities of the crystal (e.g. the FeAs layers), electronic (e.g. Fe d-orbitals and the shape of the Fermi surface) and the energy (e.g. the BNC scaling) structures between iron-based superconductor members [9, 10]. Therefore the $s_\pm$ model is one of the favored candidates of the pairing symmetry of the iron-based superconductors. However, it might still take a couple years from now (even after over a decade since the initial discovery) to completely solve the puzzle behind the pairing mechanism of the unconventional iron-based superconductors.

6.3 References

[1] R Prozorov and V G Kogan. London penetration depth in iron-based superconductors. *Reports on Progress in Physics*, 74(12):124505, 2011.

[2] R. T. Gordon, H. Kim, N. Salovich, R. W. Giannetta, R. M. Fernandes, V. G. Kogan, T. Prozorov, S. L. Bud'ko, P. C. Canfield, M. A. Tanatar, and R. Prozorov. Doping evolution of the absolute value of the london penetration depth and superfluid density in single crystals of $Ba(Fe_{1-x}Co_x)_2as_2$. *Phys. Rev. B*, 82:054507, Aug 2010.

[3] K. R. Joshi, N. M. Nusran, K. Cho, M. A. Tanatar, W. R. Meier, S. L. Bud'ko, P. C. Canfield, and R. Prozorov. Measurements of the lower critical field of superconductors using nv centers in diamond optical magnetometry, 2018.

[4] Meng Li, N. R. Lee-Hone, Shun Chi, Ruixing Liang, W. N. Hardy, D. A. Bonn, E. Girt, and D. M. Broun. Superfluid density and microwave conductivity of FeSe superconductor: Ultra-

long-lived quasiparticles and extended s-wave energy gap. *New Journal of Physics*, 18(8):1–8, 2016.

[5] V. G. Kogan, C. Martin, and R. Prozorov. Superfluid density and specific heat within a self-consistent scheme for a two-band superconductor. *Phys. Rev. B*, 80:014507, Jul 2009.

[6] S. Teknowijoyo, K. Cho, M. Kończykowski, E. I. Timmons, M. A. Tanatar, W. R. Meier, M. Xu, S. L. Bud'ko, P. C. Canfield, and R. Prozorov. Robust $s_{\pm}$ pairing in $CaK(Fe_{1-x}Ni_x)_4as_4$ ($x = 0$ and 0.05) from the response to electron irradiation. *Phys. Rev. B*, 97:140508, Apr 2018.

[7] K. Cho, M. Konczykowski, S. Teknowijoyo, M. A. Tanatar, Y. Liu, T. A. Lograsso, W. E. Straszheim, V. Mishra, S. Maiti, P. J. Hirschfeld, and R. Prozorov. Energy gap evolution across the superconductivity dome in single crystals of (Ba1-xKx)Fe2As2. *Science Advances*, 2(9):e1600807–e1600807, 2016.

[8] Y Wang, A Kreisel, P J Hirschfeld, and V Mishra. Using controlled disorder to distinguish s and s ++ gap structure in Fe-based superconductors. *PHYSICAL REVIEW B*, 87:94504, 2013.

[9] P. J. Hirschfeld. Erratum: Corrigendum to Using gap symmetry and structure to reveal the pairing mechanism in Fe-based superconductors (Comptes Rendus Physique (2016) 17(1-2) (197231)(S1631070515001693)(10.1016/j.crhy.2015.10.002)). *Comptes Rendus Physique*, 17(7):803, 2016.

[10] Yunkyu Bang and G. R. Stewart. Superconducting properties of the s -wave state: Fe-based superconductors. *Journal of Physics: Condensed Matter*, 29(12):123003, 2017.

APPENDIX. SAMPLE HOLDER PARTS DRAWINGS

Several Autodesk Inventor drawings of the sample holder parts of the ^{3}He system (January 2017 ver.) are attached below. I have more files saved in the shared desktop PC in the graduate student office, please refer when needed. For more details about the development of this January 2017 ver. sample holder, please also refer to the ^{3}He instrument log book and Serafim's lab book.

The parts are made of oxygen-free copper to avoid magnetic impurities that are detrimental to the measurement. The parts were gold plated before the assembly.

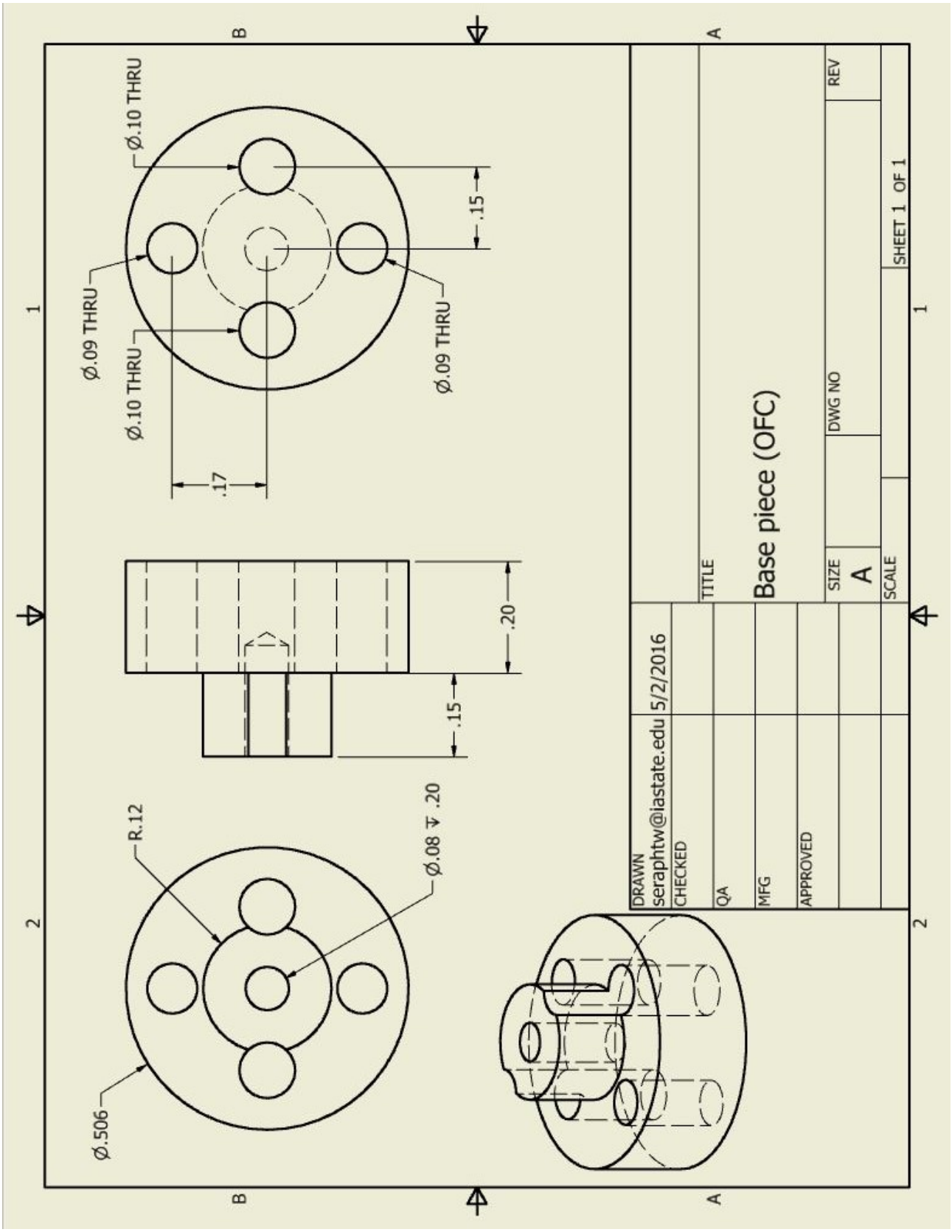
Ø.10 THRU
Ø.09 THRU
Ø.10 THRU
Ø.09 THRU
.15
.17
.20
.15
R.12
Ø.08 ↧ .20
Ø.506
DRAWN
seraphtw@iastate.edu 5/2/2016
CHECKED
QA
MFG
APPROVED
TITLE
Base piece (OFC)
SIZE
A
DWG NO
REV
SCALE
SHEET 1 OF 1

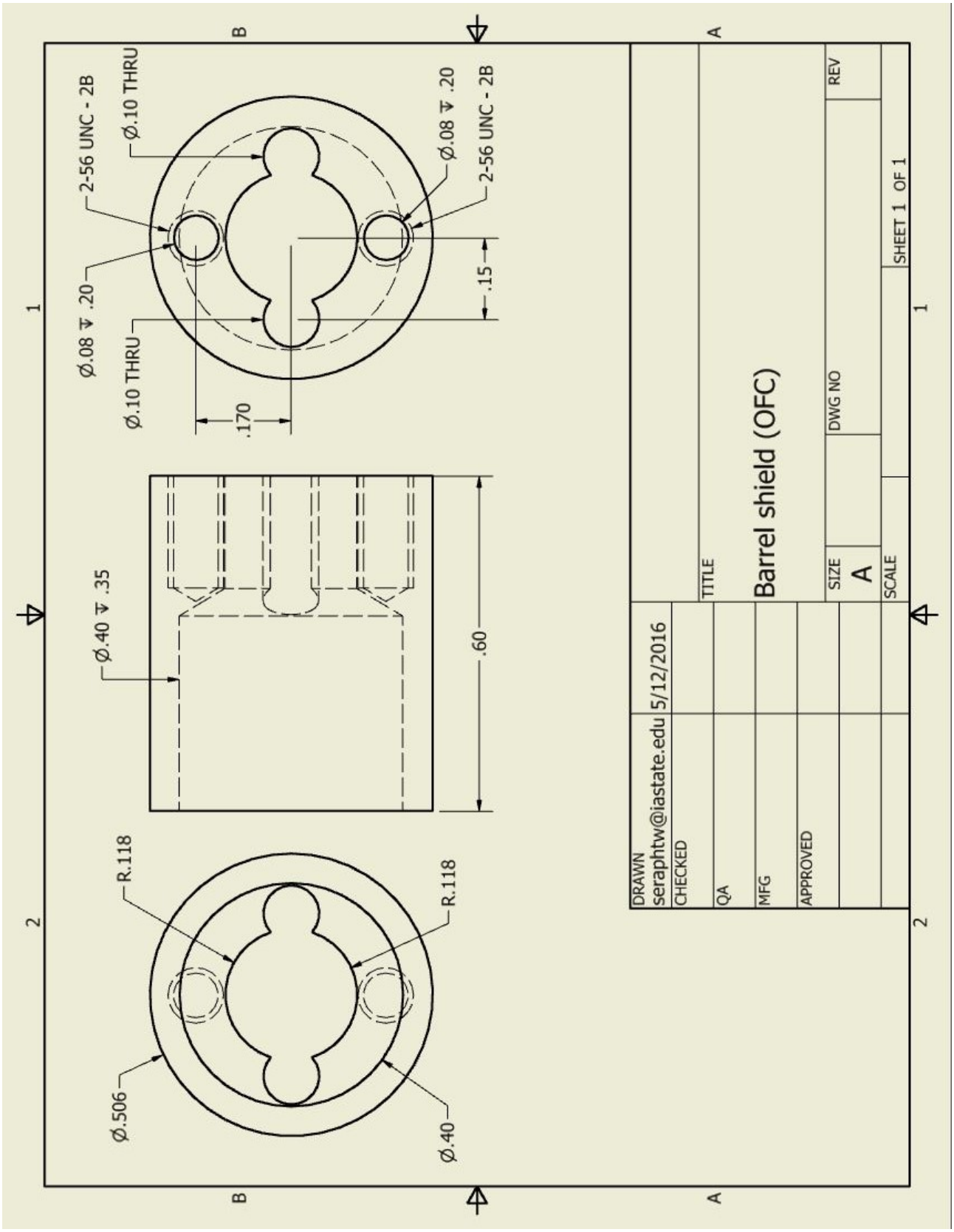
Barrel shield (OFC)
DRAWN
seraphtw@iastate.edu 5/12/2016
CHECKED
QA
MFG
APPROVED
TITLE
SIZE
A
DWG NO
REV
SCALE
SHEET 1 OF 1
Ø.10 THRU
2-56 UNC - 2B
Ø.08 ▼ .20
Ø.08 ▼ .20
2-56 UNC - 2B
Ø.10 THRU
.170
.15
Ø.40 ▼ .35
.60
R.118
R.118
Ø.506
Ø.40

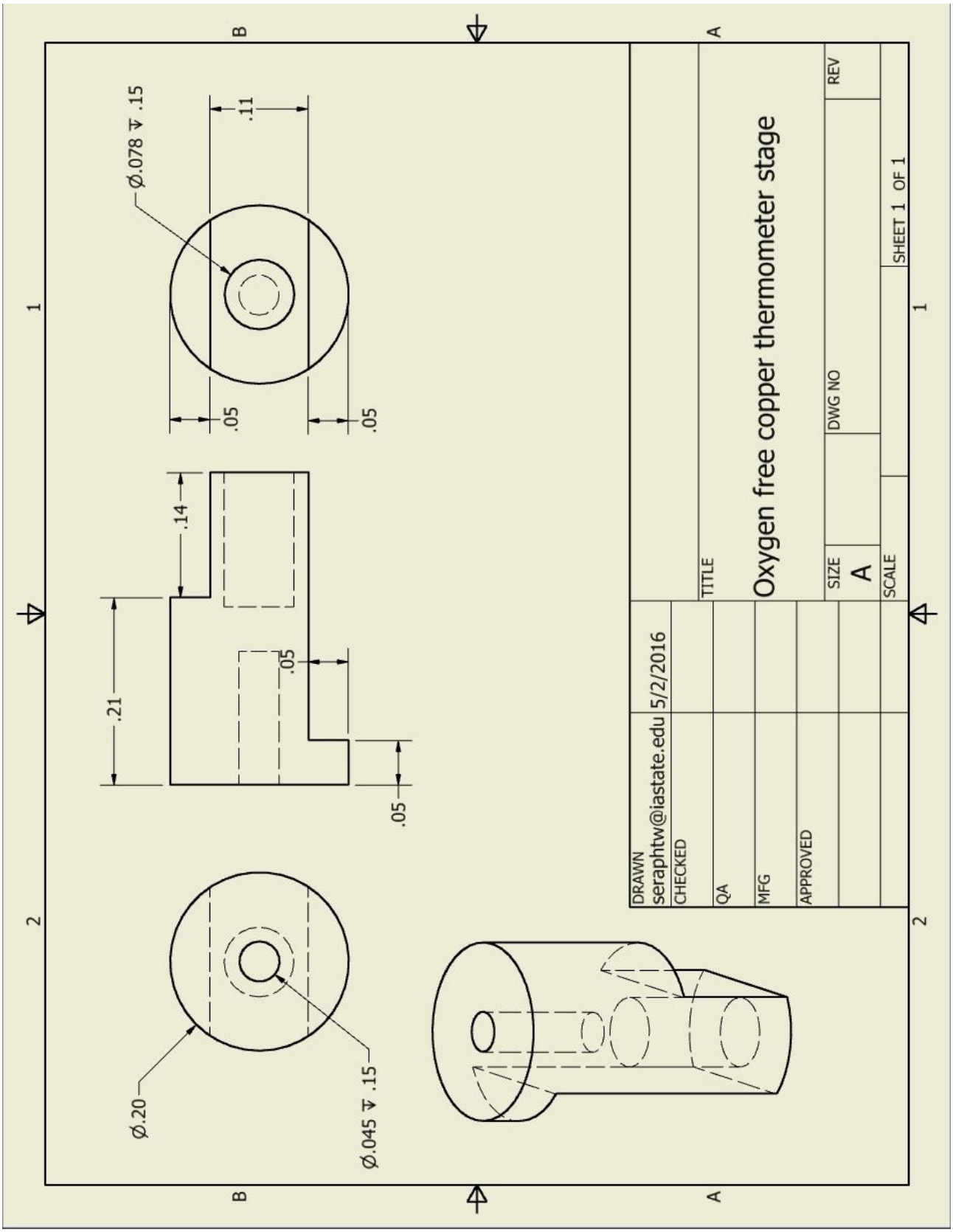
Ø.078 ∓ .15
.11
.05
.05
.14
.21
.05
.05
Ø.20
Ø.045 ∓ .15
DRAWN
seraphtw@iastate.edu 5/2/2016
CHECKED
QA
MFG
APPROVED
TITLE
Oxygen free copper thermometer stage
SIZE
A
DWG NO
REV
SCALE
SHEET 1 OF 1